AN EXPERIMENTAL AND NUMERICAL CONVECTIVE HEAT TRANSFER ANALYSIS OVER A TRANSONIC GAS TURBINE ROTOR BLADE

by

Keith Baharath Cassie

Dissertation submitted in fulfillment of the academic requirements for the degree of Master of Science in Mechanical Engineering

University of Kwa-Zulu Natal

Durban

December 2006

ABSTRACT

An experimental and numerical investigation of the flow and convective heat transfer distribution around a high turning angle gas turbine rotor blade has been carried out at the University of Kwa-Zulu, Durban campus. This study in gas turbine blade aerothermodynamics was done to meet the research and development requirements of the CSIR and ARMSCOR. The experimental results were generated using an existing continuously running supersonic cascade facility which offers realistic engine conditions at low operating costs. These results were then used to develop and validate a 2-D model created using the commercially available Computational Fluid Dynamics (CFD) software package, FLUENT.

An initial phase of the study entailed a restoration of what was an unoperational experimental facility to a state capable of producing test simulation conditions. In the analysis, a 4-blade cascade system with provisions for an interchangeable test blade was subjected to the steady state conditions set up by the facility. Firstly, the flow was characterised by evaluating the static pressures around the midspan of a pressure measurement test blade. This was done using two pressure transducers, a scanivalve, an upgraded data acquisition system and LABview software.

The method for measuring the heat transfer distributions made use of a transient measuring technique, whereby a pre-chilled Macor test blade, instrumented with thin film heat flux gauges was rapidly introduced into the hot cascade flow conditions by displacing an aluminum dummy blade while still maintaining the flow conditions. Measurement of the heat flux and generation of the isothermal heat transfer co-efficient distributions entailed re-instrumentation of the test blade section with gauges of increased temperature sensitivity along with modifications of the associated electrical circuitry to improve on the quality of experimental data.

Both the experimental flow and heat transfer data were used to validate the CFD model developed in FLUENT. An investigation into different meshing strategies and turbulence models placed emphasis on the choice of model upon correlation. The outcome of which showed the $k-\omega$ model's superiority in predicting the flow at transonic conditions.

A feasibility study regarding a new means of implementing a film cooled turbine test blade at the supersonic cascade facility was also successfully investigated. The study comprised of experimental facility modifications as well as cascade and blade redesigns, all of which were to account for the requirements of film cooling. The implementation of this project, however, demanded the resources of both time and money of which neither commodity was available.

The author would like to dedicate this dissertation in loving memory of his dearest father, the late Mr. B.P Cassie.

"You were the greatest story ever told."

PREFACE

The Author hereby states that this entire dissertation, unless specifically indicated to the contrary in the text, is his own original work, and has not been submitted in part or whole to any other University. This dissertation records the work carried out by the author in the School of Mechanical Engineering at the University of Kwa-Zulu Natal, Howard College Campus from February 2005 to December 2006. The project was supervised by Prof. S Govender and forms part of the ongoing research in the field of convective heat transfer and aerodynamics around axial flow turbine blades.

"Imagination is more important than knowledge."

- Albert Einstein

ACKNOWLEDGEMENTS

The work that I have been fortunate enough to spend the last 22 months on would not have been possible without the help of a number of people, to all of whom I am very grateful.

First and foremost, I would like to thank my supervisor Professor S. Govender for his friendship support and supervision as well as Professor J. Visser for providing me with this opportunity to perform research in the field of Gas Turbine Technology.

Mr G Snedden, R Stieger, J de Villiers for their efforts in building and developing the experimental rig and it associated techniques. A special thank you to Glen for his help and support throughout the project.

Mr Montresor Morris and Dr Danie de Kock at the University of Pretoria for their assistance with the numerical simulations.

The workshop staff at the School of Mechanical Engineering, especially Mr Michael Smith, for their help and advice with the experimental rig.

Kris Kulik and Graham Kennedy for their assistance and advice in the project.

Nululeko, Nirasha, Ismail, Keith and Mishen from the 4th year design project team for their assistance with the feasibility study.

Dr Bruce Olmstead for thankfully making my life a bit more hectic and encouraging me to complete.

Zaahir, Priyen, Vaughan, Jesse, Noel, Clinton, Jean, Stefanie, Yunus (a,k,a German Spy), Imeraan and those international guys for the outrageous in between hour partying. Shot alot!

And most importantly, my dearest mother, annoying sister Lee-Ann, wacko brother Darryl, Beon and inquisitive niece Aaryanna, for pretending they knew what I was talking about and putting up with all my weird antics.

TABLE OF CONTENTS

LIST OF FIGURES

CHAPTER 5

CHAPTER 6

CHAPTER 7

LIST OF TABLES

APPENDIX C

NOMENCLATURE

Symbols

η_{cycle}	cycle efficiency
H	enthalpy
C_p	specific heat
T	temperature
q	heat flux per unit area
$k-\varepsilon$	FLUENT turbulence model that solves the turbulent Prandtl numbers governing the turbulent diffusion of kinetic energy term (k) and kinetic energy dissipation rate (ε)
$k-\omega$	FLUENT turbulence model that solves the transport equations kinetic energy term (k) and kinetic energy dissipation rate (ω)
$\dot{q}_s(t)$	heat flux rate per unit time
d	thin film gauge thickness
k	conductivity
κ	constant of proportionality
R	thin film resistance
α_R	alphaR, temperature coefficient of resistance
ρ	density
t	time
V	voltage
I	current
c'	distributed electrical capacitance per unit length
r'	distributed electrical resistance per unit length
$\frac{A^*}{\beta}$	calibration constant for the electrical analogue
c	capacitance
D	chord length
μ	viscosity
U	velocity
y^+	non-dimensionalised distance from the wall

τ_0	shear stress
ρ	density
u_τ	friction velocity which is related to the shear stress and density by $\sqrt{\tau_0/\rho}$
y	cell height perpendicular to the wall
p_{op}	operating pressure
p	local (relative to p_{op}) gauge pressure
θ	temperature change relative to ambient $(T - T_\infty)$
θ_s	temperature change relative to surface $(T_s - T_o)$
α	thermal diffusivity
Q	electrical charge
∇	differential operator
∇^2	Laplacian
x	distance normal to surface
H	Heaviside function
ν	Poisson's Ratio
σ	stress
γ	specific heat ratio

Subscripts

0	reference or initial condition
1	thin film gauge material
2	substrate material
f	film
w	wall
s	surface
∞	ambient condition (space), or infinity (time)
in	inlet
out	outlet

op	operating
x	x-coordinate
y	y-coordinate
z	z-coordinate

Abbreviations

2-D	Two-Dimensional
3-D	Three-Dimensional
A/D	Analogue to Digital
AMG	Algebraic Multigrid Method
ASME	The American Society of Mechanical Engineers
CD	Circumferential Distance
CFD	Computational Fluid Dynamics
CSIR	Council for Scientific and Industrial Research
HP	High Pressure
HTA	High Turning Angle
I/O	Input/Output
IR	Infrared
LENS	Large Energy National Shock Tunnel
LES	Large Eddy Simulations
LP	Low Pressure
NGV	Nozzle Guide Vane
RANS	Reynolds-Averaged Navier-Stokes equations
RKE	Realizable $k-\varepsilon$ turbulence model
RNG	Renormalisation Group Theory, $k-\varepsilon$ turbulence model
RTD	Resistance Temperature Detectors
SA	Spalart-Allmaras
SKE	Standard $k-\varepsilon$ turbulence model
SKO	Standard $k-\omega$ turbulence model
SST	SST $k-\omega$ turbulence model
TFG	Thin Film Gauges
TGP	Thermographic Phosphors
TIT	Turbine Inlet Temperature

TLC	Thermochromic Liquid Crystals
UKZN	University of Kwa-Zulu Natal
VI	Virtual Instrument (from LabVIEW)
VKI	von Karman Institute

CHAPTER 1

INTRODUCTION

Since the powering of flight by the Wright Brothers in 1903 up until the end of World War II, the piston–driven internal combustion engine was the predominant form of power for both military and civilian aircrafts. Despite the technological advances in this form of power generation, the demands for an ever faster aircraft with capabilities of attaining higher altitudes revealed limitations to this form of propulsion. The progressive decrease in efficiency of the propeller at high aircraft speeds and power loss in the engine at elevated altitudes were just some of the reasons for the implementation of gas turbines to modern day aircrafts.

Gas turbines are essentially rotary engines that extract energy from a flow of combustion gas. This form of propulsion system is made up of an upstream compressor which is coupled to a downstream turbine with a combustion chamber in-between. The energy is released when pressurized air and fuel is mixed and ignited in the combustion chamber of which the resulting gases are directed over the blades of the turbine. The turbine thus spins, powering the coupled compressor while expelling the air through a nozzle which assists in the generation of thrust. Figure 1-1 shows the mechanical arrangement of a single-spool axial flow turbojet.

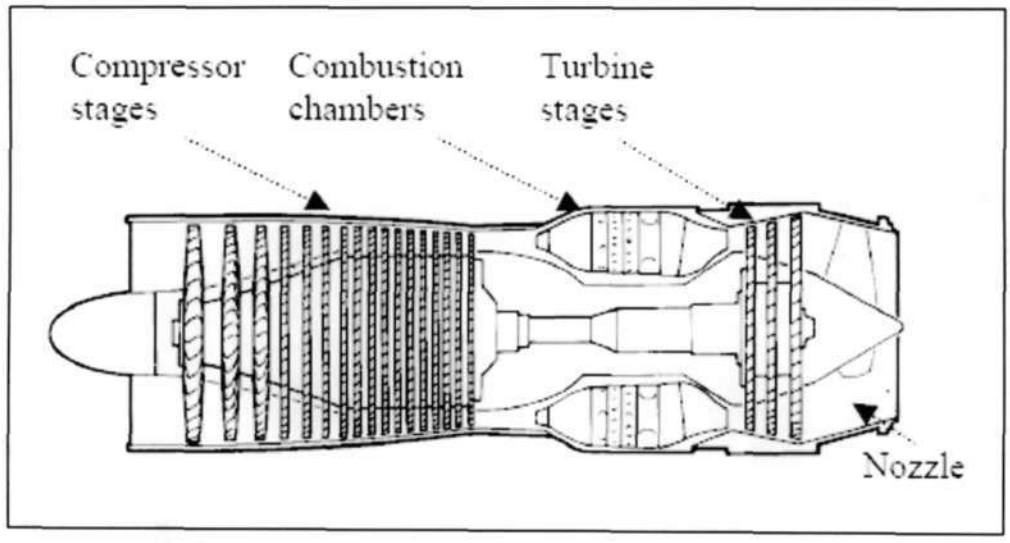

Figure 1-1 Mechanical arrangement of a single-spool axial flow turbojet (Rolls- Royce, 1986)

Thermodynamically, gas turbine engines are described by the Brayton cycle which is graphically shown in Figure 1-2. Here, an ideal gas like air is isentropically compressed, and combustion at near constant pressure then increases the temperature which is subsequently expanded isentropically back to the starting pressure. In practice however, friction and turbulence gives rise to non-isentropic compression and expansion as well as pressure losses in the air intake, combustor, turbine and exhaust, all of which decreases the efficiency of the cycle.

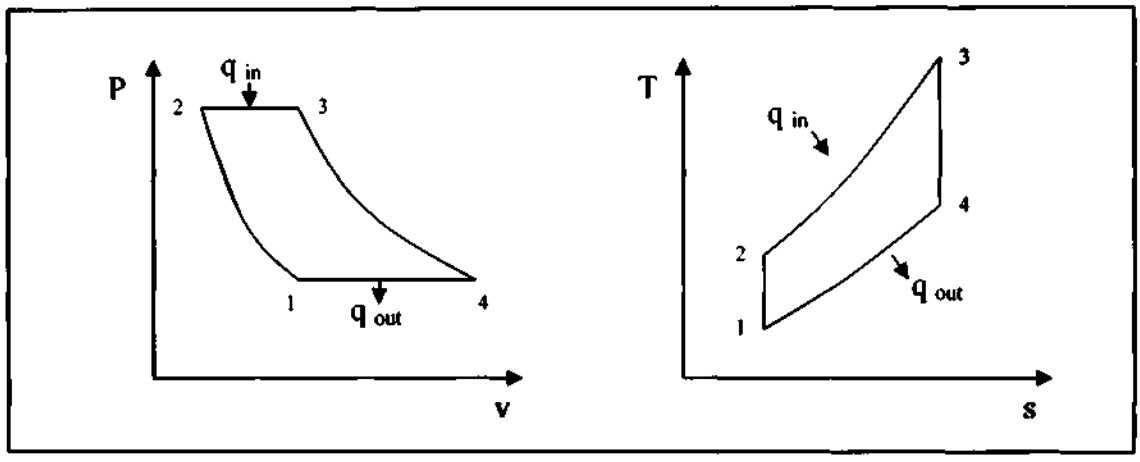

Figure 1-2 P-v and T-s diagrams respectively for an idealized Brayton cycle

As with all heat engines, a common means of raising the overall efficiency lies with increasing the combustion temperature, T_3. This is evident from a derivation of the Brayton cycle to represent the cycle efficiency, given in equation 1.1, which assumes a constant Specific heat capacity, C_p.

$$\eta_{cycle} = 1 - \frac{C_p(T_4 - T_1)}{C_p(T_3 - T_1)} \tag{1.1}$$

It is the ever increasing need for technological advancements in aerospace propulsion that has seen a significant amount of research being put forward into increasing the combustion exit temperature which would result in higher thermal efficiencies and pressure ratios. The coupled benefit of lower specific fuel consumptions (SFC), supported by Camci and Arts (1989) would result in significant financial savings, given the high fuel costs and operational times of these engines. This need for higher combustion temperatures is limited predominantly by the first set of stator blades in the turbine, which is known as nozzle guide vanes (NGV), and is located directly downstream of the combustion chamber.

The limitations imposed by increasing the turbine inlet temperature (TIT) are associated with the material from which the blades are constructed. This has seen the development and incorporation of high temperature resistant super alloys as well as thermal barrier coatings in gas turbine blade designs. However, research has seen that the usage of an effective cooling strategy will allow the TIT to be raised higher than the melting point of the blade material, of which current high performance engines are in the range of 1800 K. This point is further illustrated in Figure 1-3, which shows the increase in TIT due to the various cooling schemes implemented over recent decades.

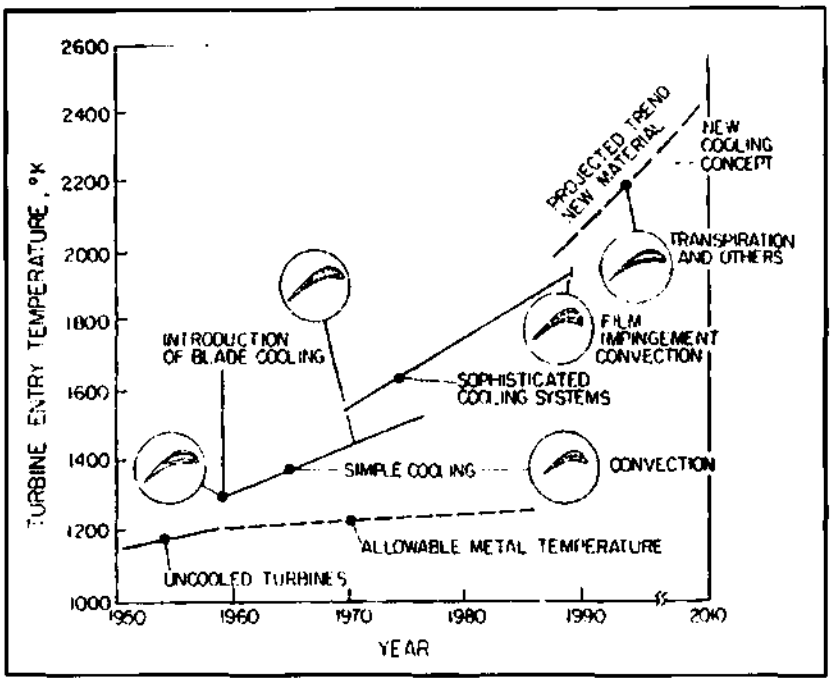

Figure 1-3 TIT variations due to various cooling strategies implemented over recent years (reproduced from Han, Dutta and Ekkad (2000))

Of all the different cooling technologies available from internal to external, one of the most popular means which has attracted justifiable attention in recent times has been discrete-hole film cooling. In this form of cooling, coolant air is forced through an array of small holes arranged over the surface of the blade exposed to high temperatures. This strategy not only cools the blade in areas of high heat transfer rates, such as the leading edge but further downstream of the profile, caused by the coolant washing away and forming a cooler air blanket. Figure 1-4 shows a blade with discrete-hole film cooling.

Since one of the main objectives in blade cooling is to minimize thermal stresses caused by the severe non-homogeneous temperature environment set up by the combustor, a principal

objective would then be to attain a uniform blade metal temperature. Film cooling prevents the blade surface from being directly exposed to the combustor exit temperature environment, thereby reducing the thermal stresses that the blade would otherwise have been exposed to.

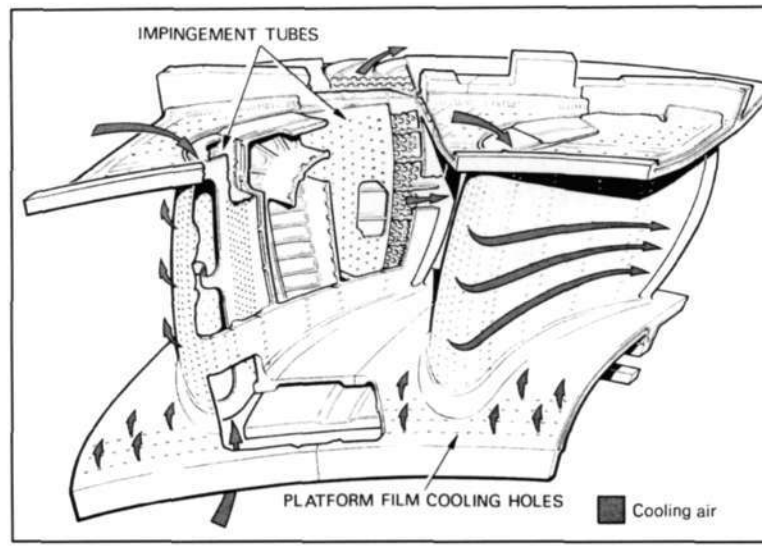

Figure 1-4 Nozzle guide vane illustrating film and impingement cooling scheme (reproduced from Son, Gillespie, Dailey and Ireland (2000))

Although this technology will offer increased blade service life, the utilisation of coolant air which is bled from the latter stages of the compressor, usually results in a reduction of the turbine efficiency and usage of any additional coolant will result in a reduction of the overall cycle efficiency. Therefore, in order to optimise on the amount of coolant used and determine the location of coolant ejection, it is imperative to accurately predict firstly the heat transfer co-efficient distribution over the blade surface.

The problems arising with predicting accurate heat transfer rates to blades are due to a number of factors. These include blade aerodynamics, free stream turbulence, boundary layer transition, vortices, separation, reattachment, main flow acceleration/deceleration and shock waves, to name a few of the related complex flow phenomena. The usage of Computational Fluid Dynamics (CFD) to analyze the flow across engine components has been seen to achieve immense advances in the aerodynamic community. With the time consuming and costly endeavor of conducting aerodynamic experimental evaluations, the benefits of using the virtual tools present in CFD makes this form of approach even more desirable and experimentation somewhat redundant. However, even though numerical codes have advanced to a point where time resolved 3-D heat transfer data for vanes and blades are routinely available by those operating full rotating rigs, the generation of experimental data is vital as it is used to validate

the reliability of these codes. The work carried out in this dissertation was therefore aimed towards validating and developing a CFD model against experimental data using a commercially available numerical code.

The experimental results were generated using an existing continuously running supersonic cascade facility. This facility offers the benefit of achieving realistic engine conditions at low operating costs. The investigation considers the flow over a high turning angle gas turbine rotor blade. In the analysis, a 4-blade cascade system is subjected to the steady state test conditions set up by the experimental rig. The flow was firstly characterized by evaluating the static pressure distribution over the midspan of the profile. This is used to validate the prediction of the corresponding heat transfer distribution, as high Mach numbers are associated with low heat transfer rates and vice versa. The heat transfer distributions were measured using an existing transient technique, where a pre-cooled Macor test blade which is instrumented with thin film heat flux gauges, is rapidly introduced into the hot cascade flow conditions by displacing an aluminium dummy blade. This measuring technique was implemented by Snedden (1995).

The numerical analysis was performed using the commercially available CFD suite, FLUENT, of which the geometry was created in its pre-processor, GAMBIT. FLUENT was used to resolve the flow field and heat transfer to the blade. The data from the experimental simulations were used as boundary conditions for the numerical model. The results generated from this model were then put under investigation by comparing it to the experimental data.

CHAPTER 2

LITERATURE SURVEY

2.1 Introduction

The extensive amount of research available for jet engine turbine blade heat transfer generally falls into two main categories, namely, experimental measurements and numerical predictions. The primary goal of predicting and validating heat transfer distributions over turbine blade profiles is seen towards designing an efficient cooling mechanism so as to raise the TIT and improve on the engine's overall efficiency. This literature review considers the experimental facilities and techniques used by the various researchers into predicting accurate heat transfer measurements. The numerical models and codes used to validate these experimental results were also reviewed so as to exhibit the development in numerical prediction techniques.

The previous work done at the University of Kwa-Zulu Natal, Durban Campus by Snedden (1995), Stieger (1998) and de Villiers (2002), have all presented comprehensive literature surveys in the field of external blade heat transfer measurement techniques as well as published results over the past few decades. This survey is therefore intended towards summarising their efforts as well as adding to the database.

2.2 Experimental Testing Facilities

One of the most delicate engineering tasks is the design and application of measurement techniques in gas turbine environments. An efficient design of the instrumentation requires a sound knowledge of the aerodynamics of the gas flow path in the machine and a good idea of the limits of the flow parameters, namely temperature and pressure. The transient measurement of heat transfer to turbine blades holds with it the fundamental requirement that a temperature gradient exists between the air stream and the blade profile. As it is important to understand all heat-transfer aspects under actual engine conditions, the measurement of these details require the simulation of the blades general operating environment. In order to acquire precise measurement of these details, the heat transfer community utilises experimental facilities that are designed to simulate realistic engine flow Reynolds numbers, Mach numbers, and gas-to-metal temperature ratios associated with turbine fluid mechanics and heat transfer. These

facilities presented below have all been used to conduct experiments using flat and curved surfaces, leading edge models, and scaled airfoil cascades at simulated engine conditions to better understand the related flow phenomena.

2.2.1 Light Piston Compression Tunnels

This experimental facility achieves operating conditions by compressing air isentropically using a light piston. Consequently, compressed air is used to drive this piston forward, thereby raising the test sections air pressure and temperature to the desired level for testing. Once test conditions have been attained, a fast acting shutter valve is actuated which then releases the high pressure, high temperature air over the cascade model under investigation. A sonic throat situated after the test section is used to create constant mass flow conditions and a downstream dump tank allows for pressure adjustments to vary the cascade outlet Mach numbers. The compression times of these facilities range in the order of 1.0 second with a run time of approximately 0.1 to 0.5 seconds. This rapid exposure of heated gas thus creates the temperature gradient used to evaluate the heat transfer distributions over the various cascade profiles. Figure 2-1 depicts a schematic of the CT-3 isentropic compression tube annular cascade, used at the von Karman Institute for Fluid Dynamics in Belgium. The principals of this type of wind tunnel is described by Jones *et al.* (1973), and its capabilities given in Richards (1980) as well as in Consigny and Richards (1982). The benefits of short duration cascade simulations include low capital and running costs when compared to continuously running facilities involving rotating turbines or two-dimensional cascades. The disadvantages however include large storage spaces as well as problems associated with the transient establishment of flow through the test section.

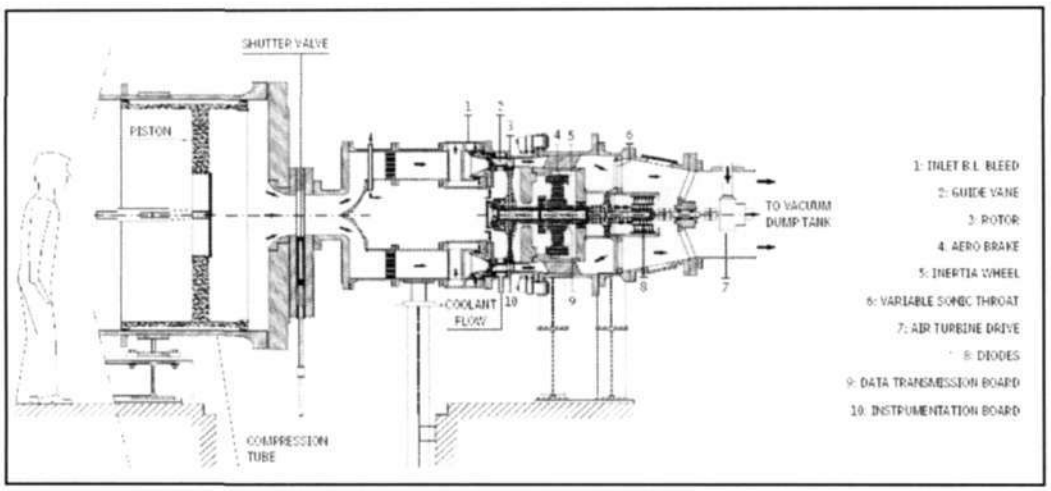

Figure 2-1 CT-3 Isentropic compression tube annular cascade (reproduced from www.vki.ac.be)

The ability of this facility to generate flow conditions at different Mach numbers, Reynolds numbers and gas-to-wall temperature ratios amongst other attractive features, has seen a significant amount of researchers investing their efforts into understanding the issue surrounding external turbine blade heat transfer at varying conditions. Researchers of note include Consigny and Richards (1982), who conducted short duration heat transfer measurements to a gas turbine rotor blade. Their efforts investigated the effect that Mach numbers, Reynolds numbers, inlet flow angles and free stream turbulence levels have on the heat transfer rate over the rotor profile. Camci and Arts (1985a, 1985b) used the same profile to perform investigations of the heat transfer distribution with the leading edge and suction side being film cooled, respectively. They further investigated the effects of film cooling on the heat transfer rate by simultaneously ejecting coolant flow through the leading edge, suction side, and the pressure side. This study investigated the effects of overall mass weight ratio, coolant to free-stream temperature ratio and free stream turbulence on the heat transfer rate distributions.

2.2.2 Shock Tube Facilities

Shock tubes are devices that use a high-pressure gas to set up a shock wave which will compress a low-pressure gas and heat it to very high temperatures indicated by Pope and Goin (1965). The shock tube is made up of two tubes separated by a diaphragm. One of the tubes is filled with a driver gas at a high pressure and the other tube is filled with the driven gas at a low pressure. The driver gas is usually helium or nitrogen and the driven gas is air. At time zero, the diaphragm bursts and the pressure step splits into a shock wave which propagates into the driven section, and an expansion wave which propagates into the driver section. The created shock wave therefore compresses and heats the driven gas. These facilities are used as a short duration wind tunnel by utilising the flow behind the shock wave. This set-up is schematically shown in Figure 2-2.

A derivation of the shock tube facility is the shock tunnel. These facilities include a shock tube and a nozzle attached to the driven section of the shock tube as well as a diaphragm between the driven tube and nozzle. When the shock tube is fired, the generated shock reaches the end of the driven tube and it is reflected back breaking the diaphragm. The heated and compressed air behind the reflected shock is then available for operation of the tunnel. Dunn et al. (1984) provides a description of this type of facility and conducted heat transfer investigations on a NGV, rotor, and shroud of a turbine blade. Additional work by Dunn et al. (1986) included heat flux and pressure measurements on a low-aspect-ratio turbine stage using a similar shock tube

wind tunnel facility. In actual fact, Dunn has been a pioneer in the use short duration experimental techniques to obtain fundamental measurements on the vanes and blades of full stage rotating turbines. An excellent source of literature regarding his work can be found in Dunn (2001).

Another variation is the gun tunnel. The longshot facility at VKI consists of a driver tube and a driven tube known as a barrel. The barrel is separated from the hypersonic convergent-divergent nozzle by valves. A piston is held in position by an aluminium disc at the junction of the driver chamber and barrel. The driver is pressurised with nitrogen at 300 -1000 bar and the barrel at 1-1.5 bar with the test section being at almost vacuum. The piston is then released from the disc, accelerating down to the barrel at a speed of up to 600m/s. The shock wave produced propagates ahead of the piston and is reflected at the end of the barrel. When the pressure starts to increase, the gas is allowed to expand through the hypersonic nozzle by rupturing a diaphragm. The reflected shock then strikes the piston face and the piston decelerates while the shock is reflected back to the barrel end. A number of shock reflections between the piston face and the barrel end then occur and when the piston velocity reaches zero, the valves at the end of the barrel close automatically, so that there is no flow back from the test section. Since a finite volume of test gas expands through the nozzle, the stagnation conditions decay with time, also limiting the duration of the test.

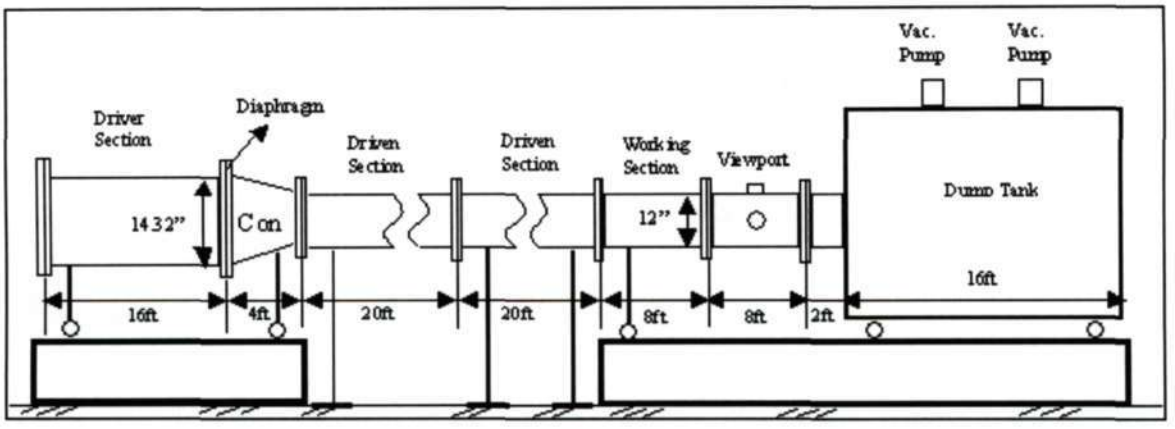

Figure 2-2 Schematic representation of a shock tube (reproduced from www-me.ccny.cuny.edu)

2.2.3 Continuously Running Facilities

The large storage space requirements of light piston and shock tube facilities are overcome by the usage of continuously running facilities. The experimental work carried out in this

dissertation was done using the continuously running supersonic cascade present at the University of Kwa-Zulu Natal's Department of Mechanical Engineering, Durban Campus. This facility operates under vacuum and consists of a centrifugal compressor which re-circulates the air within a plenum. The required Reynolds and Mach numbers are attained by adjusting the speed of the compressor and the temperature of the air is controlled by varying the amount of water supplied to a radiator housed within the plenum. This unique facility has the benefits of low storage space and low operation costs. Further details of its operation and equipment are given in Chapter 4 of this dissertation.

The facility was originally used and designed by Van der Steege (1990) for the purpose of assessing cooling performance on turbine blades. McDonald (1994) used the facility to study tip clearance effects on turbine blade endwalls and Snedden (1995) implemented the required instrumentation and data acquisition systems for the transient measurement of heat transfer distributions over turbine blade profiles. Stieger (1998) further continued the research of heat transfer distributions as well as conducted flow visualisation experiments to better understand the complex 3D flow pattern within the cascade. In an effort to develop numerical modelling techniques, the previous work done on heat transfer was complemented by de Villiers (2002) who validated the experimental results using the CFD package, FLUENT. Apart from local researchers, those abroad include Graziani et al. (1980) who used a low speed, open circuit cascade wind tunnel facility to conduct heat transfer measurements on a scaled endwall and airfoil of a turbine blade. The scale was approximately 10 times that of actual engine size and two inlet boundary layer thicknesses were investigated to determine the effects on the local heat transfer rates.

2.3 Experimental Measurement Techniques

The accuracy of heat transfer distributions is largely dependent on the type of measurement technique used. There are various measurement techniques available and the results are usually expressed as a non-dimensional parameter such as Nusselt number, heat transfer co-efficient ratio, or temperature ratios. Researchers choose experimental methods that are most suitable for the test model under investigation and the results they expect to obtain. An effective cooling design depends largely on the experimental correlations generated. These correlations have been developed by researchers who used actual components or revised simplistic models in their experimental efforts. The current experimental methods available may be split into heat transfer measurement techniques, mass transfer analogy techniques, optical techniques, and flow and thermal field measurement techniques.

2.3.1 Heat Transfer Measurement Techniques

2.3.1.1 Heat Flux Gauges

Thin-film heat flux gauges are used by researchers for the measurement of heat transfer rates on actual gas turbine blades under realistic engine conditions. These gauges are effectively resistance thermometers with very fast response times in the order of about 10^{-8} seconds. Thin-film heat flux gauges are easily attached flush to the heat transfer surface by means of painting or vapour deposition. This means of attachment overcomes the difficulty associated with the instrumentation of standard thermocouples which would usually disrupt the general flow conditions. The gauges are devices with a thin metallic element of very small heat capacity attached to a surface bearing good insulating and machining properties. Platinum is commonly chosen as the gauge and Macor or Quartz as the substrate. The gauges are supplied with a constant current and any change in temperature will result in a change in voltage. The step in voltage is then post processed to obtain the corresponding heat flux. Thin-film heat flux gauges were successfully implemented at the University of Kwa-Zulu Natal by Snedden (1995) and a detailed discussion of its construction, operation and processing technique employed can be found in Chapter 3 of this dissertation as well as in Snedden (1995).

The heat flux gauges were used by Schultz and Jones (1973), Oldfield et al. (1978), Doorly and Oldfield (1986), Snedden (1995), Stieger (1998) and de Villiers (2002) for transient turbine cascade heat transfer measurements. The details for the construction and operating principles of these gages by painting platinum layers on a piece of machinable glass ceramic are analytically discussed by Ligrani et al. (1982). However it was Schultz and Jones (1973) who initially presented the means of construction i.e. hand painting and vacuum deposition, as well as the post processing technique to obtain the heat flux measurement. The post processing techniques used to obtain the wall heat flux may be calculated numerically using the Crank-Nicholson scheme implemented by Denos (1996) and Buttsworth (1997), or by an electrical analogy that consists of a resistance-capacitance network which converts the wall temperature signal into a signal proportional to heat flux, presented by Oldfield et al. (1982). This dissertation made use of an electrical analogy implemented by Snedden (1995) together with hand painted thin film gauges on a piece of Macor substrate.

To date these gauges are extensively used at various research facilities and of particular note, the VKI institute for fluid dynamics where a considerable amount of research into blade aerothermodynamics has been carried out. Initially, Consigny (1979) used the gauges on a cold

flat plate made of quartz to determine the influence of the pressure gradient and free stream turbulence on the heat transfer to the plate using the CT2 Isentropic Light Piston facility at VKI. Entire blade surfaces were then made of ceramic and instrumented with heat flux gauges, an illustration of a stator blade with thin-film gauges is presented in Figure 2-3. Some of the researchers included Consigny and Richards (1982), who conducted their analysis on a ceramic rotor blade instrumented with thin film gauges, Arts et al. (1990) who studied the effect of free stream turbulence, Reynolds number and Mach number on the time-averaged heat transfer distribution at the midspan of a nozzle guide vane. Camci and Arts (1990) measured the time averaged heat transfer distribution at midspan of a film-cooled rotor blade.

Because Macor is not a sufficiently high strength material, using it in rotating equipment will compromise its structural integrity. Therefore in order to overcome this obstacle, gauges were deposited on a vitreous enamel-coated metal. A technique developed by Doorly and Oldfield (1986, 1987). In more recent times, measurements were successfully performed on the rotor blades of the one and a half turbine of the VKI CT3 facility by using ceramic inserts fitted into metallic blades. These researchers include Denos (1996), who studied the influence of the shock wave of the nozzle guide vanes on the Nusselt number distribution and Didier et al. (2002), who determined the time-averaged and time resolved heat transfer coefficient at 15%, 50% and 85% span of the rotor blade as well as on the rotor tip and hub platform. Dunn et al. (1984, 1986) and Guenette et al. (1989) also made extensive use of these thin film-heat flux gauges for heat transfer measurements on full stage rotating turbine rigs, investigating various parameter influences on heat transfer rates.

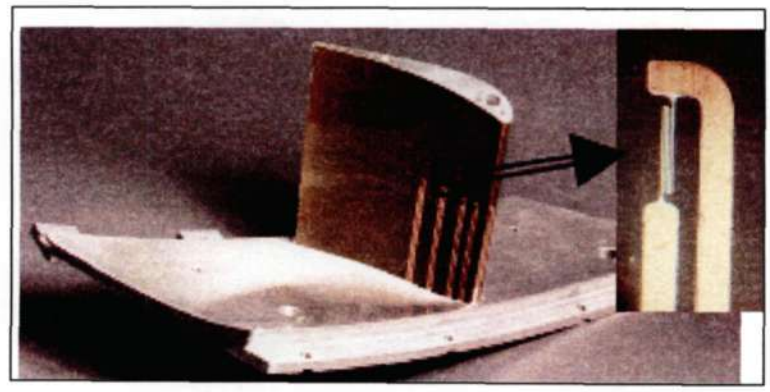

Figure 2-3 Thin-Film heat flux gauges instrumented on a stator blade (reproduced from www.vki.ac.be)

2.3.1.2 Thin-Foil Heaters with Thermocouples

The usage of foil thermocouple techniques allows for direct temperature measurements on heat transfer surfaces. Although this technique is often associated with low speed wind tunnel testing, it is possible to measure actual wall temperatures and study the various effects on the metal components under simulated engine conditions. However, the instrumentation requirements are difficult and come at high cost. The types of experimental results produced are in the form of heat transfer coefficients and film effectiveness values used for film cooling situations.

The instrumentation of these thermocouples involves a test plate which is made of a relatively low conducting medium used to reduce heat dissipation from the noncontact sides of the plate. The surface under investigation is instrumented with thin stainless steel foil strips with each foil strip being relatively small in width when compared to its span length. The strips are connected in series and supplied with an electric current that produces a constant heat flux. Thermocouples are then soldered on the underside of the foils along the span of each foil strip. The electrical power supplied to the foils provides a high resistance, low current heating device. The surfaces which are now heated, are then exposed to the desired flow conditions and upon reaching steady state, the temperature histories are downloaded and local heat transfer coefficients are calculated. The results from this form of methodology are usually of a low resolution but of sufficient accuracy. Shown below in Figure 2-4 is an instrumented NGV with thin-foil heaters and associated thermocouple leads.

Figure 2-4 Instrumented NGV with thin-foil heaters and thermocouples (reproduced from Fransson and Rubensdorffer (2004))

Some of the researchers who use this form of technique include Bellows and Mayle (1986), who investigated heat transfer downstream of a leading edge separation bubble. Their model consisted of a semicircular leading edge radius which joins smoothly into two parallel flat surfaces such that there is a step change in curvature. The step change would cause a region where the flow would intensely speed up accompanied by the adverse pressure gradient and cause the laminar leading edge boundary to separate. The subsequent reattachment of the boundary layer would then result in the formation of a separation bubble of which its effects on heat transfer were investigated.

Han (1988) used thin foil heaters and embedded thermocouples for heat transfer measurements in internal ribbed channels. Each of the test channels were made of nonconductive material which was a combination of thick wood board and thick Plexiglas plate. The 0.0025 cm thick stainless steel foils were cemented to the inner face of the wooden board and each heater was independently controlled by a variac transformer. The thermocouples were soldered to the underside of the foils at fixed locations and its connecting wires were pulled through the wooden and Plexiglas plates. The thermocouples measured the wall temperature on the assumption that the foil would indicate the same temperature on either side of the channel. This technique provided low resolution results but the measurements were robust and very cheap. The test surface instrumentation is extremely important in this technique and depending on thermocouple accuracy and test section instrumentation, uncertainty levels vary at about ±5% to ±10%.

The test surfaces may also be used to determine film effectiveness in film cooling situations. In these sort of situations the test section is instrumented downstream of the injection holes with thin foil strips and thermocouples. The heat transfer coefficients are measured with the mainstream and cooling air being at the same temperature, which is ambient, and the test section being heated. The film effectiveness is measured by using a similar setup but by heating the coolant and leaving the face unheated. Several researches such as Mick and Mayle (1988), Mehendale and Han (1992) and Ou et al (1994) have used this methodology.

2.3.2 Mass-Transfer Analogy Techniques

2.3.2.1 Naphthalene Sublimation

In order to overcome problems associated with axial heat conduction effects in usual heat transfer experimentation, the usage of mass analogy techniques have become very popular. With the ability to produce relatively high resolution heat transfer coefficient results, more and more researchers have opted to use this technique. Naphthalene sublimation is one of the most convenient techniques used to determine the local or averaged mass transfer coefficients. These coefficients are determined by measuring the mass of naphthalene sublimed by either forced or natural convection. The naphthalene test surface is usually prepared by dipping, spraying, machining or casting into the allowable complex geometry under investigation. The local mass transfer coefficient at the measurement point is then determined from the rate of mass transfer per unit surface area, the local naphthalene vapour density and the local bulk naphthalene vapour density. The local mass transfer is usually expressed by the dimensionless Sherwood number which is analogous to the Nusselt number. The ratios of the Sherwood number are then directly estimated to the Nusselt number for similar flow conditions to determine heat transfer data. The analogy between the transfer of mass and heat is directly applied on the assumption that the turbulent transport and boundary conditions are the same. The local heat transfer coefficients are determined with high accuracy and with detail by using automated measuring systems that eliminate human errors and reduce irrelevant sublimation losses. This method however, cannot generally be used in certain flow situations such as high velocity flows, because of recovery temperature effects and natural convection due to the thermal buoyancy effects of sublimation latent heat, Goldstein et al (1995).

The naphthalene sublimation technique has been demonstrated by a number of investigators to be an excellent method for obtaining heat transfer results. Goldstein and Spores (1988), and Goldstein et al (1995) used this method to study the heat and mass transfer of turbine endwalls. Haring et al (1995) coated an entire blade surface with naphthalene to study the heat and mass transfer over the airfoil profile. This technique has also been extensively used to study internal channel cooling effects by Han et al (1988), who conducted experiments using a two-pass test section to investigate the internal heat and mass transfer distributions for rotating channels.

Goldstein and Taylor (1982) used this technique to measure heat and mass transfer coefficients downstream of a flat plate instrumented with film cooling holes. Film cooling effectiveness tests are conducted in two separate experimental runs. The first test uses pure air as the mainstream

medium as well as the coolant, with the test surface coated with naphthalene. In the second test, the coolant is naphthalene saturated air such that the naphthalene density in the coolant is close to the value for the test surface wall. The mass transfer coefficient obtained from the first experiment, which is considered analogous to the heat transfer coefficient, is then compared against the second experiment containing the naphthalene saturated air. The result is the wall effectiveness which is then converted to obtain the film cooling effectiveness. More details about this technique can be found in Cho and Goldstein (1995) and Goldstein et al (1982), who used it for film cooling measurements.

2.3.3 Optical Techniques

Optical techniques are measurement techniques whereby a test surface is observed from outside the flow field path. In general, most optical techniques require some form of visualisation mode such as infrared thermography, Thermographic phosphors or liquid crystal thermography. These visualisation modes are described in more detail below.

2.3.3.1 Infrared Thermography

Infrared thermography is a non-intrusive measurement technique used for surface temperature measurements. This measurement technique has been extensively applied over the past few years in the gas turbine industry and accuracy of its instrumentation has been significantly improved. Infrared thermography is used for direct surface temperature measurements over a well characterised surface with know emissivity to temperature data. The results from this methodology are full surface temperature maps in both low and high temperature environments. Typical imagery from this technique is shown in Figure 2-5, which depicts the temperature maps of a NGV.

The test surface is constructed from a low thermally conductive insulation material that reduces conduction losses. It is instrumented with stainless steel heater foils and embedded thermocouples which measure the discrete location temperatures. Its test surface is subsequently coated in a black paint, with an emissivity value of about 0.95. An infrared camera system then provides a 2D distribution of the surface temperature. The image is then digitised into an array of pixel values with the thermocouples on the foil heaters providing the required calibration data for the infrared signal. The usage of insulation material on the test surface thus assumes conduction losses to be negligible allowing the measurement of adiabatic wall surface

temperatures. Despite the expensive nature of the material, such as quartz or zinc-salinide, the outcome from these experiments are of a high resolution with an accuracy of ±1%.

Adiabatic wall temperature measurements have been conducted by various researchers such as Gritsch et al (1998) and Kohli and Bogard (1998). Blair and Launder (1975) introduced a measurement technique for determining film effectiveness. In this technique, infrared imaging is done with a cold window and a heated/unheated surface with an emissivity value very close to 1. This technique has also been used for measuring heat transfer in rotating channels by Glezer et al (1998), as well as rotating channels that are impingement cooled by Epstein et al (1985).

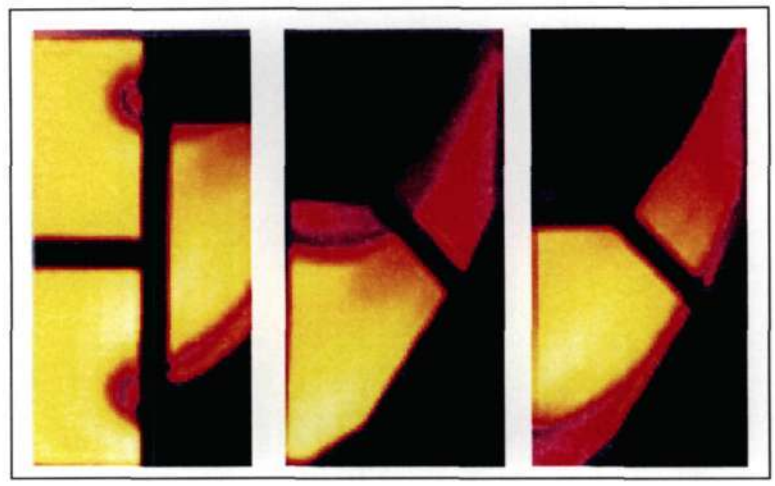

Figure 2-5 Leading edge, suction side and pressure side infrared images (reproduced from Fransson and Rubensdorffer (2004)

2.3.3.2 Thermographic Phosphors

Another non-intrusive measurement technique is done by using thermographic phosphors. Thermographic phosphors exhibit a specific luminescence which is dependent on temperature when exposed to a UV light. This remote measurement technique exploits its temperature dependence to measure the surface temperatures over complex test geometries. The most significant advantage of this technique its use at temperature as high as 1700 K, allowing its use in actual engine conditions. One of the researchers who used thermographic phosphors to measure temperatures over jet engine components includes Noel et al (1990). His experimentation model used a YAG laser to excite the thermographic phosphors over turbine vanes by way of fibre optics to probe. The return signal is detected by a photomultiplier tube and analysed in a waveform-processing oscilloscope. The data was plotted against increasing

engine rpm and their work further supported the usage of this technique as a non-intrusive method for evaluating turbine component temperatures under general operating conditions.

2.3.3.3 Liquid Crystal Thermography

This powerful and widely used visualisation tool correlates the colour response of a heat surface treated with thermochromic liquid crystals to temperature. The thermochromic liquid crystals are materials that change their reflected colour as a function of temperature when illuminated by a white light. It therefore reflects visible light at different wavelengths. The colours are calibrated to particular temperatures since the transition of colours are sharp and defined. The liquid crystals can be factory set with the appearance of the primary red, green and blue colours calibrated to specified fixed temperatures. The bandwidths for the colour transition may also be set to allow for wide or narrow band measurements depending on the measurement requirements.

Son et al (1999) used the transient liquid crystal technique to conduct heat transfer measurements on an engine representative impingement cooling system. The measurements were conducted using coatings comprised of a mixture of three narrow band thermochromic liquid crystals. The crystals had the ability to record single measurements over a wide range of temperatures allowing heat transfer coefficient data to be generated over the full test surface in a single experiment. Full local heat transfer coefficient distributions were measured with high accuracy on both the target and impingement plates.

2.4 Flow and Thermal Field Measurement Techniques

Apart from the heat transfer measurement techniques outlined above, flow field and thermal measurements augment the understanding of the heat transfer phenomena. It is imperative that the knowledge of the flow and thermal field away from the test surface which causes the heat transfer characteristics be understood. There are several measurement techniques readily available to researchers to obtain these sorts of data and these are outlined very briefly below.

Five-hole probe/thermocouples are used for mean velocity measurements and hot/cold-wire anemometry systems has been seen as an effective tool for measuring fluctuating velocity and temperature components in non-isothermal boundary conditions. A high resolution non-intrusive measurement technique with extensive capabilities is Laser Doppler Velocimetry (LDV). This technique has the capabilities of providing full field flow measurements at any

plane of the flow as well as determining all turbulence quantities and Reynolds stresses. The capabilities of this system make it highly feasible for film cooling technology experiments and researchers such as Pietryk et al (1990) and Thole et al (1998) have all opted to use such techniques in their film cooled models. A branch of this technique includes particle image velocimetry, where a laser sheet of the seeded flow is captured in an image by a camera. This technique has been used for flow measurements in internal rib turbulated channels by Schabaker et al (1998). Surface visualisation tools are also helpful measurement techniques used to further understand the flow field characteristics. This technique, seen as a very simple tool is very effective in providing a great deal of information over solid profiles. Stieger (1998) conducted flow visualisation experiments at varying turbulence intensities on the high turning angle SMR-95 rotor profile by using a mixture of poster paint pigment and multigrade motor oil. The streak patterns formed provided an excellent visual description of the boundary layer flow patterns and characteristics. An illustration of the outcome is shown below in Figure 2-6, which depicts the suction side SMR-95 profile at 15% turbulence intensity.

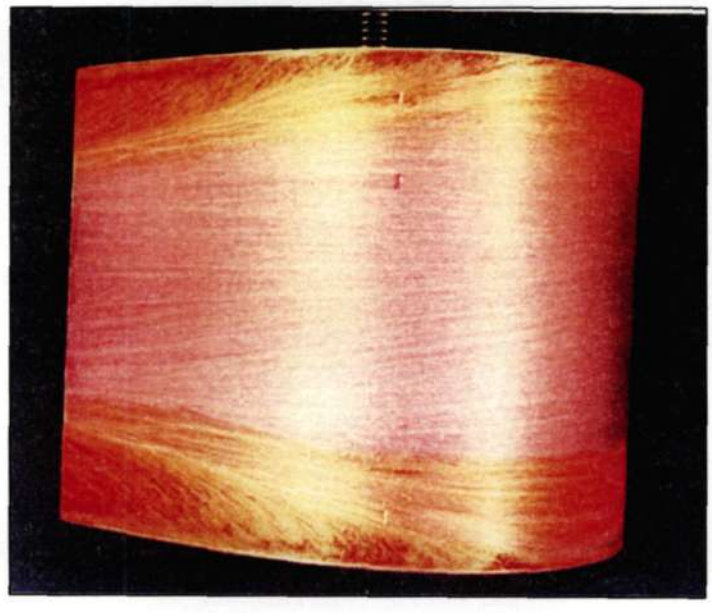

Figure 2-6 Flow visualisation measurements seen on the suction side of the SMR-95 profile at 15% turbulence intensity (reproduced from Stieger (1998))

2.5 Numerical Prediction Techniques

The usage of numerical prediction codes by the heat transfer community has been seen to provide significant benefits in all aspects of research involving flow over airfoils. This powerful processing tool has the ability to provide researchers with a much better and clearer

understanding of the complex flow field surrounding the turbine blades. The tremendous growth in computational power of the personal computer has further aided in its economical feasibility. With advantages of providing flow details that are difficult to obtain experimentally, optimisation of various design parameters can now be done with significant savings in cost and time.

Although numerical codes have developed at a powerful pace over the past 30 years, there is currently no code in existence capable of completely and accurately predicting the highly complex flow field through the gas turbine. The accuracy of these codes is judged solely by comparing experimental data to numerical predictions. The results used for CFD verification usually comes from experimental facilities that may be about a decade old. This is because of the existing time lag between experimental facilities in use and predictive codes, with experimental facilities in the lead.

The accurate prediction of heat transfer in gas turbines has long been seen as the key into improving performance and extending service time. The use of cascade and flat plate model research were instrumental towards the development of current CFD prediction codes, with many of these models still in use today. The codes and processing power have developed to the point where time resolved 3-D heat transfer data for vanes and blades are routinely available to those operating full rotating rigs. An excellent source of literature that reviews the development of these codes and experimental models used for verification is that of Dunn (2001).

Early numerical studies in the 1970's solved the bulk flow using an inviscid Navier-Stokes or Euler code. A separate boundary layer code was then used to resolve the heat transfer using the pressure and velocity fields from the bulk flow calculations as boundary conditions. The codes were in the form of flat plate correlations, or two-dimensional boundary layer codes like STAN5, developed by Crawford and Kays (1976) at Stanford University. Graziani et al (1980) performed 3-D heat transfer measurements on a large scale cascade model and compared the results of the midspan to a numerical model using the STAN 5 code. The result was that the numerical model continuously over predicted and Graziani stated that this uncertainty was due to there being no reliable means of accurately resolving the flow field.

One of the main difficulties with predictions is the usage of proper turbulence models. Daniels and Brown (1981) used five different computer programs to calculate heat transfer to gas turbine blades. Each program incorporated a different turbulence model and the results were validated against experimental measurements made by Daniels (1978). The five models used were that of Cebeci-Smith (1974), Patankar-Spalding (1970), Cebeci-Smith-Mcdonald, Wilcox

'EDDYBL' and Wilcox (W-T). All programs exhibited good agreement with the experimental data in both the laminar and turbulent regions on the suction surface, however showed poor conformity on the pressure surface as well as the transition zones. The conclusion was that the complex two-equation models exhibited no significant advantages over the simpler one equation models.

Most common models used today are based on two-equation turbulence models, namely, standard k-ε , low Reynolds number k-ε, two-layer k-ε, and the k-ω model. Other models include the one equation Spallart Allmaras model, the Baldwin-Lomax model, algebraic closure, and second moment closure models. The low Reynolds number version of the k-ε two-equation model of Jones and Launder (1973), was integrated into the STAN 5 code by Wang et al (1985) to predict the flow and heat transfer around gas turbine airfoils. The two-zone model was then used to treat the k and ε variables in the regions near the wall. The heat transfer predictions were conducted for flat plate models, the C3X profile and the Turner airfoil, with correlations done against the experimental data of Hylton et al. (1983) and Turner (1971) for the C3X and Turner profiles respectively. The overall heat transfer results for the C3X were in good correlation to the numerical predictions however Wang's solution did over predicted at the leading edge. This difference between measurement and prediction is common at the leading edge as the flow is very unsteady. The unsteadiness is predominantly caused because of moving shock patterns and wake impingement. The predictions of the Turner airfoil however did agree well at the leading edge but not at the trailing edge. This was because the inlet Reynolds number for the Turner airfoil was much lower than that of the C3X, resulting in much slower flow conditions and thicker viscous sub-layers. This further supported the effectiveness of the low Reynolds number turbulence model. The ability of the model to simulate transitional flow accurately resulted in the flat plate model predictions to be within very good agreement to the experimental data and more and more researchers therefore opted to use this model at the time.

Another means of resolving the flow and heat transfer characteristics apart form boundary layer codes, is the usage of full Navier-Stokes solvers. These solvers have the capability to solve the entire flow field with special adaptations applied to the near wall region. A numerical code based on the compressible Navier-Stokes equations was developed by Hah (1984), for 3-D turbulent flows through turbine blade rows. The code was based on a fully conservative control volume formulation with an algebraic Reynolds stress model that was modified to incorporate for the effects of streamwise curvature. The model had the ability to show various 3-D viscous flow phenomena such as 3-D flow separation and horse shoe vortices. Comparisons were made against the subsonic flow measurements of Langston et al (1977) and the results showed a good agreement on the pressure side of the blade but not the suction side.

The use of full stage and multistage experiments brought about an even better understanding of the complex three dimensional flow field. Researchers Joslyn and Dring (1992) conducted experimental measurements on a one and a half stage, first stator, rotor and second rotor test rig. The results were compared against the full 3-D Navier-Stokes predictions of both Rai (1987) and Adamczyk et al (1990). The excellent agreement between numerical and experimental data further validated the capabilities of the full Navier-Stokes solver. The solutions of the unsteady 3-D Navier-Stokes were however predominately constrained by limitations imposed by the turbulence model of choice. Dunn et al. (1992) compared unsteady pressure measurements of vanes and blades on a transonic turbine stage to the unsteady Euler and unsteady Navier-Stokes code of Rao and Delaney (1990). The numerical predictions were within reasonable agreement with the experimental results but the conclusion was that the Navier-Stokes codes required a grid that was too computationally expensive to resolve the viscous affected regions.

A summary on 3-D CFD based models of the time-averaged flow field within axial flow turbomachines can be found in Adamczyk (2000). Adamczyk provides a detailed discussion on the development of mathematical models used in CFD. It spans from the simple mean flow governing equations, through the averaged passage model and Reynolds averaged Navier-Stokes equations right up to the full Navier-Stokes equations. Adamczyk also noted that in order to obtain a truthful solution in any CFD model, the most important variables are accurate geometries, correct inlet and outlet boundary conditions, a good quality grid and the correct choice of turbulence model.

CHAPTER 3

THEORY

3.1 Introduction

A convective study of heat transfer from fluid flow to surfaces generally requires the experimental evaluation of the heat transfer coefficient distribution coupled with a numerical validation, all of which are used to develop current CFD codes and models to push the limits towards increasing the efficiency of gas turbine engine cycles.

In order to measure heat flux in transient conditions, the measurement of the wall temperature history is fundamental to the derivation of the corresponding heat flux and associated heat transfer coefficient. The current technique used at UKZN utilizes thin film platinum resistance temperature detectors or (RTDs) to measure the surface temperature of an effectively semi-infinite Macor substrate. This method is most suitable for measurement under transient conditions as the required response times are fast enough to trace variations caused by the rapidly changing flow conditions. It should be noted that it is possible to derive heat flux from the simple measurement of the surface temperature history using a numerical algorithm, a differential process that will result in the generation of noise disruptions. The existing technique of measuring heat flux directly using analogue circuitry has the advantage of reducing noise being that the numerical algorithm to determine surface temperature from heat flux is an integration process. These techniques were implemented at UKZN by Snedden (1995) which was largely based on the system employed at the Von Karmen Institute for Fluid Dynamic as described by Ligrani et al (1982).

A useful tool in the aerospace propulsion industry is that of CFD, which may be described as the science of determining a numerical solution to the governing equations of fluid flow. In using CFD codes to complement experimental work, the end result is usually a reduction in both time and money, factors essential for profitability. The commercially available FV code FLUENT 6.2 was used for the numerical validation of the experimental aerodynamic and convective heat transfer distributions. This chapter deals with the relevant theory of obtaining heat transfer measurements and the computational methodology used in FLUENT.

3.2 Theory of Heat Transfer Measurements

3.2.1 The Thin Film Gauge

Thin film gauges operate on the simple principle that the resistance of metals enhances with a corresponding increase in temperature. Since the process of determining heat transfer rates requires the measurement of the temperature rise under transient conditions, the calculation of heat flux could easily arise from the measurement of the change in resistance of the metal. It is common practise to use platinum as the metal of choice being that its resistance varies linearly with temperature as given by:

$$R = R_o(1 + \alpha_R(T - T_o)) \tag{3.2.1.1}$$

where R is the film resistance at surface temperature T, R_o is the film resistance at temperature T_o, and α_R is the film temperature co-efficient of resistance which is determined from the experimental calibration of the gauges described in section 6.3.2.

A constant current source could then be passed across the sensors which are effectively variable resistors to produce a corresponding change in the voltage, according to Ohm's Law. The voltage signal may then be expressed as:

$$V = I \times R = I \times R_o(1 + \alpha_R(T - T_o)) = V_o(1 + \alpha_R(T - T_o)) \tag{3.2.1.2}$$

which concludes that if the initial voltage and temperature, V_o and T_o respectively, are recorded before an experimental run then the change in surface temperature, $\theta_s = T_s - T_o$, which is given by the equation:

$$\theta_s = \frac{\Delta V}{\alpha_R V_o} \tag{3.2.1.3}$$

where ΔV is the change in film output voltage captured using data acquisition software, could be used to determine the heat flux at the point of interest.

3.2.2 The Electrical Analogy

The method of determining the surface heat flux is done by utilising electrical analogue circuitry. This circuitry makes use of a series of resistances and capacitors of which the voltages and currents behave in the same way that the temperature and heat fluxes do, respectively. This analogy which exists between the heat conduction into a semi-infinite solid like Macor, and the flow of current into an infinite resistive capacitive network is evident from the similarities present in the equations defining their physical processes, i.e. the transient heat conduction equation and transmission line equation shown below, respectively:

$$\frac{\partial^2 T}{\partial x^2} = \frac{\rho C}{k}\frac{\partial T}{\partial t} \tag{3.2.2.1}$$

$$\frac{\partial^2 V}{\partial x^2} = r'c'\frac{\partial V}{\partial t} \tag{3.2.2.2}$$

In examining their behaviour, a simultaneous derivation of the appropriate forms presented on the next page, taken from Schultz and Jones (1973) best describes this analogy, where the differential elements of thermal and electrical problems given in Figure 3-1 are considered.

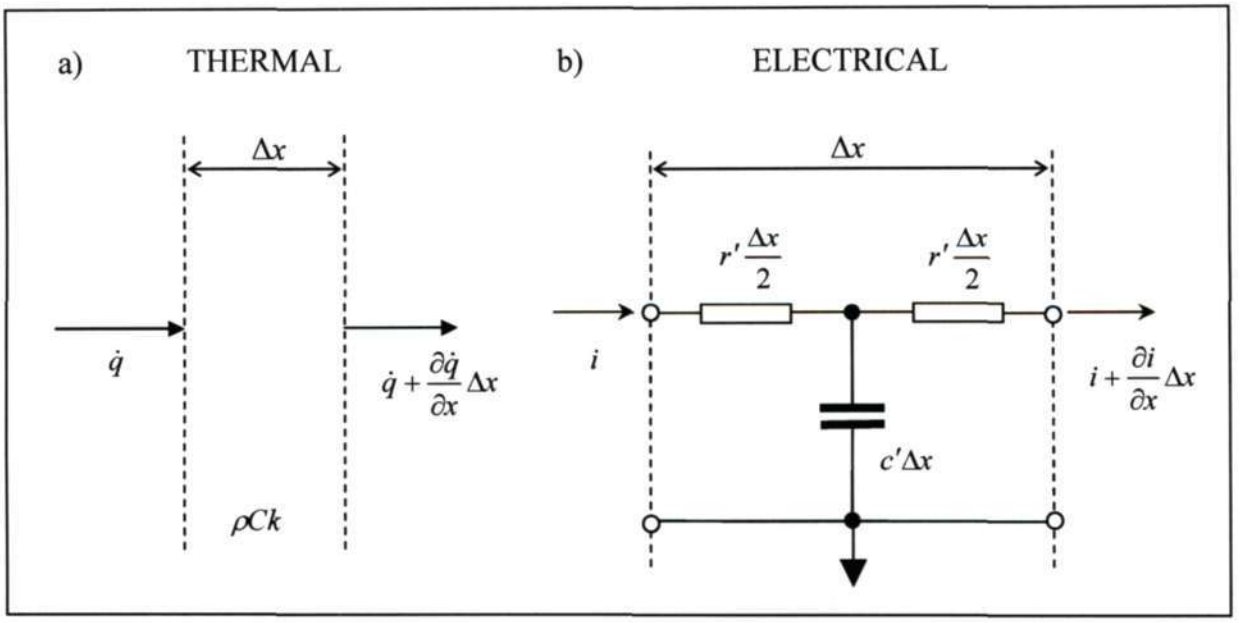

Figure 3-1 Differential elements of thermal and electrical problems

Rate of gain of energy in element Δx

$$= -\frac{\partial \dot{q}}{\partial x}\Delta x \qquad (3.2.2.3a)$$

which by conservation of energy

$$= \rho C \Delta x \frac{\partial T}{\partial t} \qquad (3.2.2.4a)$$

Thus,

$$\frac{\partial \dot{q}}{\partial x} = -\rho C \frac{\partial T}{\partial t} \qquad (3.2.2.5a)$$

The conduction equation is

$$\dot{q} = -k \frac{\partial T}{\partial x} \qquad (3.2.2.6a)$$

The diffusion equation (3.2.2.1) may then be obtained by combining the above two equations

Rate of gain of charge in element Δx

$$= -\frac{\partial \dot{i}}{\partial x}\Delta x \qquad (3.2.2.3b)$$

which by conservation of energy

$$= c' \Delta x \frac{\partial V}{\partial t} \qquad (3.2.2.4b)$$

Thus,

$$\frac{\partial \dot{i}}{\partial x} = -c' \frac{\partial V}{\partial t} \qquad (3.2.2.5b)$$

Ohm's laws is

$$i = -\frac{1}{r'\Delta x}\frac{\Delta V}{\Delta x}\Delta x = -\frac{1}{r'}\frac{\partial V}{\partial x} \qquad (3.2.2.6b)$$

The transmission line equation (3.2.2.2) may then be obtained by combining the above two equations

This gives rise to the analogy between the following parameters presented below in Table 3-1

Table 3-1: Thermal and Electrical parameter analogy

Thermal			**Electrical**		
Quantity	**Symbol**	**Units**	**Quantity**	**Symbol**	**Units**
Temperature	T	K	Voltage	v	V
Time	t	s	Time	t	s
Heat Flux Rate	$\dot{q}$	W	Current	i	A
Heat Capacity	c	J / Kg K	Capacitance	c'	F
Conductivity	k	W / m K	Conductivity	$\frac{1}{r}$	1/Ω
Length	x	m	Length	x	m

3.2.3 Heat Transfer Measurement Analysis

The time dependent problem of thin film gauges is transient heat conduction into a thin metallic film mounted on a semi-infinite extent of another material governed by equation 3.2.2.1. The situation which must be analysed is presented in Figure 3-2, which is a schematic illustration of conduction into a metal film on a ceramic substrate.

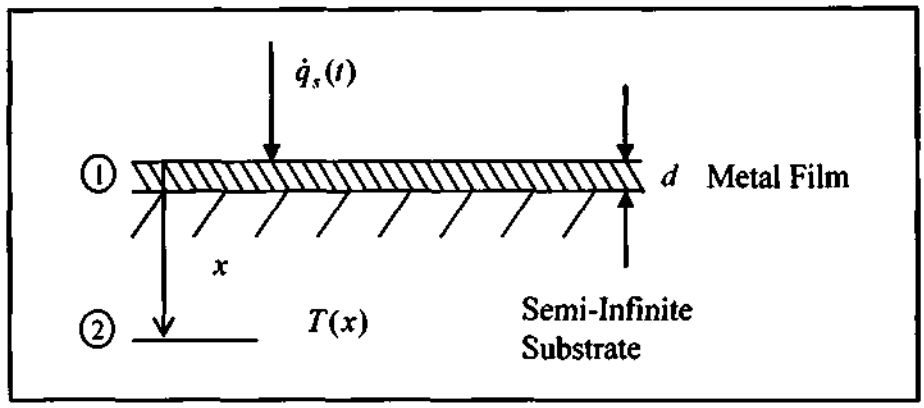

Figure 3-2 Schematic of heat conduction in thin film gauges

Theoretically the film is infinitely thin so that it does not affect the temperature history of the substrate surface. It may then be assumed that the heat flux passing into the substrate through the metallic film is one dimensional allowing the relevant theory to be applied. This analysis of heat transfer into these thin film gauges presented follows that of Schultz and Jones (1973). The differential equations that describe the heat conduction of the metal and substrate are shown below respectively:

$$\frac{\partial^2 \theta_1}{\partial x^2} = \frac{1}{\alpha_1}\frac{\partial \theta_1}{\partial t} \tag{3.2.3.1}$$

$$\frac{\partial^2 \theta_2}{\partial x^2} = \frac{1}{\alpha_2}\frac{\partial \theta_2}{\partial t} \tag{3.2.3.2}$$

where θ is the temperature change relative to ambient $(T - T_\infty)$ at distance x and time t, and α the thermal diffusivity of the material.

The boundary conditions for these equations under the assumption of one dimensional heat transfer and that the substrate is semi-infinite follow that:

i. At the interface between the fluid and film the heat flux convected into the gauge balances heat conduction at the surface thus

$$-k_1 \frac{\partial \theta_1}{\partial x} = \dot{q}_s\big|_{x=0} \tag{3.2.3.3}$$

ii. At the interface between film and substrate the heat conducted out of the gauge balances the heat conducted into the substrate where the temperature at the interface is continuous i.e. $\theta_1 = \theta_2$

$$k_1 \frac{\partial \theta_1}{\partial x}\Big|_{x=d} = k_2 \frac{\partial \theta_2}{\partial x}\Big|_{x=d} \tag{3.2.3.4}$$

iii. The substrate is semi-infinite

$$\theta_2 = 0\big|_{x=\infty} \tag{3.2.3.5}$$

Assuming that the TFG has a negligible effect on heat transfer and also that it remains at a uniform temperature due to its small size, thus it is considered as being isothermal. Letting $d \to 0$, the entire heat conduction equation for the gauge is eliminated, leaving:

$$\frac{\partial^2 \theta_2}{\partial x^2} = \frac{1}{\alpha_2} \frac{\partial \theta_2}{\partial t} \tag{3.2.3.6}$$

which is subject to the following boundary conditions

$$-k_2 \frac{\partial \theta_2}{\partial x} = \dot{q}_s\big|_{x=0} \tag{3.2.3.7}$$

and

$$\theta_2 = 0\big|_{x=\infty} \tag{3.2.3.8}$$

The initial condition for equation 3.2.3.6 is that $\theta_2 = 0$ at $t = 0$ for all values of x. So by using the Laplace transformations on both sides, this equation may be expressed as

$$\bar{\theta}_s = \frac{1}{\sqrt{\rho C k}} \frac{\bar{\dot{q}}_s}{\sqrt{s}} \tag{3.2.3.9}$$

where the overbar denotes the Laplace transforms, s is the Laplace variable, and $\sqrt{\rho C k} = \sqrt{\rho_2 C_2 k_2}$ which are parameter constants. Using the convolution theorem, the inverse transformation of $\bar{\theta}_s$ may be obtained, as shown below

$$\theta_s = \frac{1}{\sqrt{\pi}\sqrt{\rho C k}} \int_0^t \frac{q_s(\tau)}{\sqrt{t-\tau}} dt \tag{3.2.3.10}$$

The direct integration of this equation for a constant heat flux at t>0 yields

$$\theta_s = \frac{2\dot{q}_s}{\sqrt{\pi}} \sqrt{\frac{t}{\rho C k}} \tag{3.2.3.11}$$

which after rearranging and substitution of equation 3.2.1.3, where a constant current source supplies the thin film gauge, gives the heat flux $\dot{q}_s$, shown below

$$\dot{q}_s = \sqrt{\frac{\rho C k}{t}} \frac{\sqrt{\pi}}{2} \frac{\Delta V}{\alpha_R V_0} \tag{3.2.3.12}$$

3.2.4 Analogue Circuitry Calibration and Considerations

The integration process of obtaining the heat flux from equation 3.2.3.10 has the natural ability to reduce computational noise. The inverse of this process which requires the simple measurement of the surface temperature history and derivation of the corresponding heat flux has the opposite effect resulting in noise generation. In using the heat transfer analogue circuitry, the measurement of the signal proportional to the heat flux allows the usage of the noise reducing integrative nature of equation 3.2.3.10 to determine the surface temperature history and corresponding heat transfer coefficient.

The analogy described in section 3.2.2 showed that equations 3.2.2.1 and 3.2.2.2 are analogous. The solutions of these equations will thus be identical and from the methodology used in

determining equation 3.2.3.9, solving the characteristic equation 3.2.2.2 in a similar fashion will result in equation 3.2.4.1 shown below in the Laplace domain.

$$\Delta\bar{V} = \bar{i}_{in}\sqrt{\frac{r'}{c'}}\frac{1}{\sqrt{s}} \tag{3.2.4.1}$$

Noting that the circuit input voltage is the thin film output, i.e.

$$\Delta\bar{V} = \alpha_R V_0 \bar{\theta}_s \tag{3.2.4.2}$$

Substitution of equations 3.2.4.2 in 3.2.4.1 gives

$$\bar{i}_{in} = \sqrt{\frac{sc'}{r'}}\alpha_R V_0 \bar{\theta}_s \tag{3.2.4.3}$$

The heat conduction equation analogous to 3.2.4.1, which is 3.2.3.9, may be substituted for $\bar{\theta}_s$ from 3.2.4.3 to get:

$$\bar{q}_s = \sqrt{\rho Ck}\sqrt{\frac{r'}{c'}}\frac{1}{\alpha_R V_0}\bar{i}_{in} \tag{3.2.4.4}$$

The circuitry of Oldfield et al. (1985), which is the circuitry implemented by Snedden at UKZN makes use of a current to voltage converter which has an output voltage proportional to the current supplied i.e. $V_{out} = \kappa i$, where κ is a constant of proportionality allowing equation 3.2.4.4 to be rewritten as:

$$\bar{q}_s = \sqrt{\rho Ck}\sqrt{\frac{r'}{c'}}\frac{1}{\alpha_R V_0}\frac{V_{out}}{\kappa} \tag{3.2.4.5}$$

The emerging surface heat flux equations, obtained from equation 3.2.4.5, and 3.2.3.12, must be equal if $\dot{q}_s$ is constant for $t > 0$ and if $T_\infty = T_0$. Hence,

$$\bar{q}_s = \sqrt{\rho Ck}\sqrt{\frac{r'}{c'}}\frac{1}{\alpha_R V_0}\frac{V_{out}}{\kappa} = \sqrt{\frac{\rho Ck}{t}}\frac{\sqrt{\pi}}{2}\frac{\Delta V}{\alpha_R V_0} \tag{3.2.4.6}$$

By rearranging into the form

$$\frac{A^*}{\beta} = \frac{\bar{\dot{q}}_s \alpha_R V_o}{\sqrt{\rho c k} V_{out}} = \sqrt{\frac{r'}{c'}} \frac{1}{\kappa} = \frac{\Delta V}{2V_{out}} \sqrt{\frac{\pi}{t}} \tag{3.2.4.7}$$

where $\sqrt{\rho c k}$ and α_R are constants defined by the thin film gauge, V_o is the initial voltage measured across the gauge before commencement of an experimental run when t=0, then for a step change in the heat flux, $\dot{q}_s$ and V_{out} will likewise be constant. This equation defines the calibration constant of the electrical analogue circuit used to measure heat flux. The calibration of the analogue circuits is done by supplying a parabolic voltage where the ratio $\frac{\Delta V}{\sqrt{t}}$ is constant. The gauge and analogue circuitry may thus be used to accurately determine the heat flux at any time given the output voltage, parameter and calibration constants via:

$$\dot{q}_s = \frac{V_{out}}{V_o} \frac{\sqrt{\rho C_p k}}{\alpha_R} \frac{A^*}{\beta} \tag{3.2.4.8}$$

However, if V_o is measured at T_∞ and not at T_o, then an additional term may be added to compensate for this, resulting in

$$\dot{q}_s = \frac{V_{out}}{V_o} \frac{\sqrt{\rho C_p k}}{\alpha_R} \frac{A^*}{\beta} (1 + \alpha_R (T_\infty - T_o)) \tag{3.2.4.9}$$

3.2.5 Reconstruction of the Surface Wall Temperature

The final step to obtain the heat transfer coefficient requires the reconstruction of the surface temperature from the surface heat flux. The detailed solution provided by Ligrani et al. (1982) which was initially worked out by Schultz and Jones (1973), considers the analogue signal of heat flux as a series of digital data points of which at any time t, may be expressed as follows:

$$\dot{q}_s(t) = \sum_n H(t - t_n) a_n (t - t_n) \tag{3.2.5.1}$$

where H is the Heaviside function such that $H(t - t_n) = 1$ for $t \geq t_n$ or is otherwise 0, and

$$a_n = \frac{\dot{q}_{n+1} + \dot{q}_{n-1} - 2\dot{q}_n}{\Delta\tau} \tag{3.2.5.2}$$

Thus, in order to find the heat flux at time t_x where there are m data points

$$\begin{aligned}\dot{q}_s(t_x) &= \sum_{n=1}^{m} H(t_x - t_n)a_n(t_x - t_n) \\ &= H(t_x - t_1)a_1(t_x - t_1) + H(t_x - t_2) + \ldots \\ &\ldots + H(t_x - t_{x-1})a_{x-1}(t_x - t_{x-1}) + H(t_x - t_x)a_x(t_x - t_x) + \\ &H(t_x - t_{x+1})a_{x+1}(t_x - t_{x+1}) + \ldots + H(t_x - t_m)a_m(t_x - t_m)\end{aligned} \tag{3.2.5.3}$$

reduces to

$$\dot{q}_s(m) = (m-1)\dot{q}_o - m\dot{q}_1 + \dot{q}_m \tag{3.2.5.4}$$

Illustrating that the function will follow the actual signal if the first two data points, $\dot{q}_o$ and $\dot{q}_1$ are forced to zero. This allows equation 3.2.5.1 to be used as the data points. Thus, considering a single element of 3.2.5.1

$$\dot{q}_n = Ha_n(t - t_n) \tag{3.2.5.5}$$

which when represented in it's integral form shown below:

$$\dot{q}_n = \int_{t_n}^{t} Ha_n d\tau \tag{3.2.5.6}$$

is integrated using the convolution theorem with $f(t-u) = 1$ and $g(u) = H$ which have the respective Laplace transforms $F(s) = \frac{1}{s}$ and $G(s) = \frac{e^{-t_n s}}{s}$ to result in

$$\bar{\dot{q}}_n = a_n e^{-t_n s} s^{-2} \tag{3.2.5.7}$$

and by applying the principal of linearity where the sum of the Laplace transformed terms is the same as the Laplace transform of the sum, the result is

$$\bar{\dot{q}}_n = \sum_n a_n e^{-t_n s} s^{-2} \tag{3.2.5.8}$$

This is substituted into equation 3.2.3.9, giving

$$\bar{\theta}_s = \frac{1}{\sqrt{\rho C k}} \sum_n a_n e^{-t_n s} s^{\frac{-5}{2}} \tag{3.2.5.9}$$

Which is inverted once more using the convolution theorem, where the transforms of the terms under summation are found using $F(s) = s^{-\frac{3}{2}}$ and $G(s) = \frac{e^{-t_n s}}{s}$, the result of which is

$$h(t) = \int_0^t H(t - t_n) \frac{2}{\sqrt{\pi}} (\tau - t_n)^{\frac{1}{2}} d\tau \tag{3.2.5.10}$$

The integration of this is

$$h(t) = \frac{4}{3\sqrt{\pi}} H(t - t_n)(t - t_n)^{\frac{3}{2}} \tag{3.2.5.11}$$

which when substituted back into equation 3.2.5.8 produces

$$\theta_s = \frac{4}{3\sqrt{\rho c k \pi}} \sum_n a_n H(t - t_n)(t - t_n)^{\frac{3}{2}} \tag{3.2.5.12}$$

of which a_n from equation 3.2.5.2 is then substituted giving

$$\theta_s = \frac{4}{3\sqrt{\rho c k \pi}} \sum_n \left[\left(\frac{q_{n+1} + q_{n-1} - 2q_n}{\Delta \tau} \right) H(t - t_n)(t - t_n)^{\frac{3}{2}} \right] \tag{3.2.5.13}$$

$\Delta \tau$ and $H(t - t_n)$ are then removed from the summation to produce the final result used to calculate the surface temperature, expressed as

$$\theta_s(m\Delta\tau) = \frac{4\sqrt{\Delta\tau}}{3\sqrt{\rho ck\pi}} \sum_{n=1}^{m-1} \left[(q_{n+1} + q_{n-1} - 2q_n)(m-n)^{\frac{3}{2}} \right] \qquad (3.2.5.14)$$

3.2.6 Summary of Heat Transfer Measurements

The process of acquiring the isothermal heat transfer coefficient thus entails supplying the thin film gauges, which may be defined as variable temperature resistors, with a constant current source that results in a voltage signal proportional to the surface temperature being produced. This voltage signal may then be used as an input into the analogue circuitry, which produces an output voltage that is essentially the heat flux. This output of heat flux allows one to numerically reconstruct the wall temperature. By plotting a graph of heat flux versus temperature and using the method of linear regression, where a straight line fitted through the heat flux data points is extrapolated back to the point when the wall temperature difference was zero, the isothermal heat flux may be obtained. The isothermal heat transfer coefficient may then be obtained via division using the well documented relation shown below, provided that the difference between the wall and free stream temperature is known.

$$h = \frac{\dot{q}_s}{T_{wall} - T_\infty} \qquad (3.2.6.1)$$

3.3 Computational Methodology

The computational methodology of the CFD codes in FLUENT, makes use of the finite volume method. Here, the governing partial differential equations are converted into a set of discrete algebraic equations which are then solved numerically by an iterative technique. The domain in question is thus discretized into a finite set of control volumes or cells, collectively know as a grid or mesh. This grid, being structured or unstructured is solved by integrating the governing conservation equation over each cell to yield discrete equations which are linearised and finally solved using a linear equation solution algorithm. It is however the natural physics of the problem that defines the conservation equation, which by adding, removing and modifying the necessary terms results in the ability to solve the various modelling issues such as turbulent flows.

3.3.1 The Governing Equations

The governing equations that describe the fluid flow are that of the Navier-Stokes equations, which are derived from the principals of conservation of mass, momentum and energy. These are the continuity, momentum and energy equations which are presented below respectively in their general form:

$$\frac{\partial \rho}{\partial t} + \nabla(\rho \vec{V}) = S_m \tag{3.3.1.1}$$

$$\frac{\partial}{\partial t}(\rho \vec{V}) + \nabla(\rho \vec{V}\vec{V}) = -\nabla p + \nabla(\bar{\bar{\tau}}) + \rho \vec{g} + \vec{F} \tag{3.3.1.2}$$

$$\frac{\partial}{\partial t}(\rho E_E) + \nabla(\vec{V}(\rho E_E + p)) = \nabla\left[k\nabla T - \sum_j h_j \vec{J}_j + (\bar{\bar{\tau}}\vec{V}) \right] + S_h \tag{3.3.1.3}$$

where $\vec{V}$ is the velocity vector components, ρ is the fluid density, p defines the static pressure of the fluid, $\rho\vec{g}$ and $\vec{F}$ are the respective gravitational and bodily forces, S_m and S_h are the source terms for mass addition and volumetric heat generation respectively with k being the effective conductivity and T, the temperature. The summation terms of enthalpy h and flux $\vec{J}$ account for diffusion of the species j. The stress tensor, $\bar{\bar{\tau}}$ and energy, E_E are defined below in equations 3.3.1.4 and 3.3.1.5 respectively where μ is the molecular viscosity and I, the unit tensor.

$$\bar{\bar{\tau}} = \mu\left[(\nabla\vec{V} + \nabla\vec{V}^T) - \frac{2}{3}\nabla\vec{V}I \right] \tag{3.3.1.4}$$

$$E_E = h - \frac{p}{\rho} + \frac{V^2}{2} \tag{3.3.1.5}$$

3.3.2 Numerical Modelling Technique

In using the RANS equations to model flow, the solutions that are generated are via two algorithms i.e. the Segregated and Coupled. In using either of them the methodology used by FLUENT to solve the governing equations is the same, whereby

i. the domain is discretized into a finite set of control volumes

ii. the governing equations are integrated over the individual control volumes to obtain a set of algebraic equations

iii. algebraic equations are linearized and solved iteratively

3.3.2.1 Discretisation

The discretisation of the governing equations involves integration over a control volume V, shown below by equation 3.3.2.1a, in its integral form for the transport of a scalar quantity ϕ. The result is algebraic equations that are conserved on a control volume basis which when represented in its discrete form is given by equation 3.3.2.1b.

$$\oint \rho \phi \vec{V} d\vec{A} = \oint \Gamma_\phi \nabla_\phi d\vec{A} + \int_V S_\phi dV \qquad (3.3.2.1a)$$

$$\sum_f^{N_{faces}} \rho_f \vec{V}_f \phi_f A_f = \sum_f^{N_{faces}} \Gamma_\phi (\nabla \phi)_n \vec{A}_f + S_\phi V \qquad (3.3.2.1b)$$

In these equations, A represents the surface area, V is the cell volume, Γ_ϕ and S_ϕ are the diffusion coefficients and source per unit volume of ϕ respectively, for N number of faces enclosing the cell. $\rho_f \vec{V}_f \vec{A}_f$ and ϕ_f refers to the respective mass flux and value of ϕ convected through a face, having area $\vec{A}_f$.

The discrete values of ϕ are stored in the centre of the respective cells by default. The cell values ϕ_f at the cell faces are required for the convection terms in equation 3.3.2.1b and are

solved by an upwinding scheme, interpolating between the cell centre values. The upwinding scheme basically means that cell face values are derived from the quantities present in the cell upstream. The choice of upwinding schemes available is purely limited by the choice of solver and linearisation technique. The process of linearisation is where the equation sets are solved iteratively. The method in which the equation sets are solved may be either implicitly or explicitly.

In the case of implicit linearisation, the unknown value of each cell is computed using relations that include both existing and unknown values from neighbouring cells. The result is that each unknown variable will appear in more than one cell and hence equation, which is thus solved simultaneously. Explicit linearisation on the other hand computes the unknown value in each cell using a relation that includes only existing values from neighbouring cells. These quantities can then be solved systematically as only one unknown appears in one equation.

3.3.2.1 The Coupled Solver

The coupled solution algorithm solves the governing equations of continuity, momentum, energy and species transport simultaneously. In the coupled solver there is a choice of using either an implicit or explicit linearisation technique. The Coupled-Implicit solution results in a coupled system of equations in each cell which is solved simultaneously using a point Gauss-Siedel in conjunction with an algebraic multigrid, where all the variables are solved in all the cells at the same time. The choice of the explicit option in the coupled solver solves the system of equations using a multistage (Runga-Kutta) method, where all the variables in a cell are solved at a time being continuously updated. In each iteration loop of the coupled solver the following steps are undertaken:

1. Fluid properties are updated based on the initialised or current solution.

2. The governing equations are solved simultaneously.

3. Equations for the scalars such as turbulence are solved using updated variables.

4. Convergence based criteria is checked and the solution is stopped if satisfied.

3.3.2.2 The Segregated Solver

The segregated solution algorithm uses the method where the governing equations are solved sequentially. This method only allows the equations to be linearized implicitly. The point implicit, Gauss-Siedel linear equation solver in conjunction with an algebraic multigrid solves these equations. The nature of the equations being non-linear and coupled results in several iterations before a converged solution is obtained. Each iteration loop consists of the following steps:

1. Fluid properties are updated based on the initialised or current solution

2. The momentum equations for each velocity component are solved in turn using current values for pressure and face mass fluxes, in order to update the velocity field

3. If the velocity, pressure and mass fluxes do not satisfy the continuity equation, a Poisson type equation is derived from the continuity and linearized momentum equations which are solved to obtain the necessary corrections

4. Convergence based criteria is checked and the solution is stopped if satisfied

3.3.3 Turbulence Models

In the case of modelling flows that are turbulent, where the flow field is highly irregular characterised by fluctuating velocity fields, the result is that the transported quantities of momentum, energy and species concentration fluctuate as well. The nature of these fluctuations makes it computationally impractical to directly simulate. The approach of working around this is to directly solve the instantaneous Navier-Stokes equations which then by either time-averaging, ensemble-averaging or manipulation results in a set of equations that are computationally practical to simulate. These equations however, contain variables in themselves that are unknown and require further turbulence models to solve. The technique of time-averaging is known as the Reynolds Averaged Numerical Simulation (RANS) which is widely used in practical applications as the computational effort and resources used are minimal. This technique also has an extensive range of models available to solve the unknown quantities. The Reynolds averaging approach thus solves the instantaneous Navier-Stokes equations, then decomposes it into its mean (ensemble or time-averaged) and fluctuating components shown below in terms of velocity, which are used similarly for other quantities like pressure, etc.

$$V_i = \overline{V}_i + V_x' \qquad (3.3.3.1)$$

Here, V_i represents the instantaneous velocity, $\overline{V_i}$ is the mean velocity and V_x' the fluctuating velocity for changing integers of $i = 1,2,3$

FLUENT 6.2 provides the capability of choosing between several different turbulence models to solve the values of the unknown quantities brought about by RANS modelling approach. These models are listed below:

- Spalart – Allmaras model (SA)
- k – ε models
    - Standard $k - \varepsilon$ (SKE)
    - Renormalisation-group (RNG) $k - \varepsilon$ model
    - Realisable $k - \varepsilon$ model (RKE)
- $k - \omega$ models
    - Standard $k - \omega$ model (SKO)
    - Shear-Stress Transport (SST) $k - \omega$ model
- Reynolds Stress Model (RSM)
- Large Eddy Simulations

3.3.3.1 The Spalart-Allmaras Model

The Spalart – Allmaras turbulence model is a one equation low cost model that solves the RANS modelled transport equation for kinematic turbulent viscosity. This model in its original form is effectively used for flows involving low Reynolds numbers and requires that the viscous affected layer be properly solved. The model was specifically designed for use in the aerospace and turbomachinery industry where the flows are wall-bounded and boundary layers are subjected to adverse pressure gradients. The usage of this model is on areas where the flow exhibits mild separation such as supersonic and transonic flows.

3.3.3.2 The $k - \varepsilon$ Models

The three $k - \varepsilon$ models have essentially the same forms which model the turbulent productivity k, heat and mass transfer, and account for compressibility effects in the same fashion. It is in the value of the respective Prandtl numbers, calculation of the turbulent viscosity and dissipation rates ε, which differentiates the models. These two equation models solve the two separate transport equations for k and ε, allowing the turbulent velocity and length scales to be independently determined.

The Standard $k - \varepsilon$ (SKE) is the most widely used turbulence model for industrial applications as it is robust, economical and reasonably accurate for a wide range of problems. This high Reynolds number model has been known to perform poorly in flows where there is strong separation, large stream line curvature and favourable pressure gradients, due to it being a semi-empirical model. The weaknesses known in the model brought about improvements in the form of two variants, being the RNG and realisable $k - \varepsilon$ (RKE) models.

The RNG $k - \varepsilon$ model was derived from a statistical technique known as Renormalisation Group Theory. This model contains an additional term in the ε equation to improve accuracy and computes the turbulent Prandtl number analytically where as the standard version uses user-specified constant values. This model may also be used for low Reynolds number applications as the RNG theory provides an analytically derived differential formula for effective viscosity.

The recent development of the Realisable $k - \varepsilon$ model differs from its standard predecessor in two ways. It employs a new formulation for the turbulent viscosity and a new transport equation for ε. The Realisable term suggests it ensures realisability of the model and means that the model satisfies the mathematical constraints of the Reynolds stresses that are consistent with the

physics of the turbulent flow. The immediate benefit of this model is that it more accurately predicts the spreading of both planar and round jets. It is also likely to provide superior performance in flows where there is rotation, recirculation, separation and boundary layer under strong adverse pressure gradients.

The performance of the three models depends strongly on the viscous flow in the near wall region as it is this region where the solution variables have large gradients. The usage of near wall treatments allows adaptations to the main $k - \varepsilon$ model which solve the flow taking into consideration viscous effects and the no slip condition i.e. law-of-the-wall. The near wall functions available are:

- Standard Wall Functions
- Non-Equilibrium Wall Functions
- Enhanced Wall Treatment

In general, wall functions are a set of laws which serve as boundary conditions for momentum, energy, species and turbulent quantities. The standard and non-equilibrium wall function treatment does not solve the viscous sub-layer and buffer region illustrated in Figure 3-3, but uses semi-empirical formulae to bridge the viscous affected and fully turbulent regions. In the case of enhanced wall treatments, the turbulent model is modified allowing the regions from the turbulent core till the wall to be solved. This combines the use of a blended law-of-the wall and a two-layer zonal model. The respective treatments therefore require special meshing techniques in order to be accurately modelled. The standard and non-equilibrium wall function approach requires a mesh that can be relatively coarse where the first cell centroid should be within the log-law layer of $y^+ = 30 - 300$. The enhanced wall treatment requires meshes that are fine enough to resolve the viscous sub-layer with each wall adjacent cell centroid being located within the viscous sub-layer i.e. $y^+ = 1$. This is suitable for low Reynolds number flows with complex near-wall phenomena.

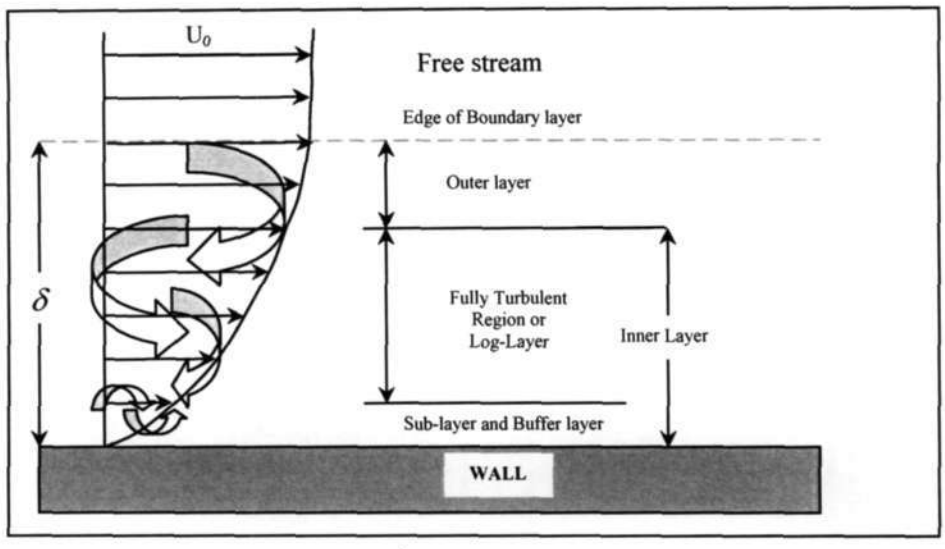

Figure 3-3 Sub-divisions at the near-wall region

3.3.3.3 The $k - \omega$ models

The Standard and SST $k - \omega$ models available in FLUENT have the same form which solves for the unknown quantities of k and specific dissipation rate ω, in the transport equations. The standard $k - \omega$ is a modified version which allows for the incorporation for low Reynolds number effects. The SST $k - \omega$ model however, incorporates a blending function that allows it to switch from the standard $k - \omega$ model in the near-wall region to a high Reynolds number version of the $k - \varepsilon$ model in the free stream. This model also incorporates a modified turbulent viscosity formulation to account for transport effects in principal turbulent shear stresses. These models have gained significant popularity in the aerospace and turbomachinery industry because it can be integrated without using any damping functions, and they produce accurate results for a wide range of applications involving boundary layer flows with pressure gradients, flow around airfoils and transonic shock waves

The details pertaining to the Reynolds Stress model (RSM) and the Large Eddy Simulation (LES) model have been omitted as the resources of computational time and effort were not available.

CHAPTER 4

EXPERIMENTAL EQUIPMENT

4.1 Introduction

The Department of Mechanical Engineering at UKZN holds in its possession a unique high speed cascade testing facility. This facility was originally designed by Van der Steege (1990) for the purpose of assessing cooling configurations and its performance on turbine blades. McDonald (1994) used the facility to study tip clearance effects under steady state conditions and it was Snedden (1995), who provided the necessary modifications to allow the measurement of heat transfer coefficients at realistic blade velocities. The facility and techniques implemented, where used by the likes of Stieger (1998), de Villiers (2002), and G.S Kennedy in 2004 who continued the research on turbine blade heat transfer while performing the necessary modifications and upgrades to improve on the quality of experimental results.

The facility uses a continuously running cascade system with thin film heat flux gauges to experimentally determine the heat transfer coefficient distribution around the blade profile. The transient measurement technique employed consists of a 4-blade cascade which is continuously subjected to heated air. A pre-cooled instrumented test blade then displaces a dummy blade into the hot cascade while maintaining the flow conditions. The usage of this technique in a continuously running facility offers the benefits of reduced storage space, time and money. The disadvantage however is the mechanical reliability of the rig. This is predominantly due to its age and downtime experienced between researchers. The mechanical failure of the rig experienced at the start of this project saw extensive work being done to restore the facility in its original condition. Descriptions of the high speed rig and its associated components together with the experimental equipment used to determine the pressure and heat transfer distributions are presented in this chapter with reference being made to the refurbishments conducted.

4.2 The High Speed Experimental Rig

The high speed rig present at UKZN consists of a large cylindrical vacuum chamber or plenum that contains an instrumented 4-blade cascade connected to an angled diffuser that feeds into the eye of a centrifugal compressor. The compressor is driven by a hydraulic motor which is

stepped up six times by a custom built gearbox. An annular cooling radiator is slotted within the plenum to regulate the temperature of the air while a secondary cooling circuit containing a series of heat exchangers and an air pump is used to pre-cool the instrumented test blade. This relatively low cost facility which offers continuous flow conditions has the distinct advantages of saving time and money over its rivals such as light piston and blow down facilities which offer short durations of flow at high operating costs. It is these advantages which were the motivation for its construction in the early 90's.

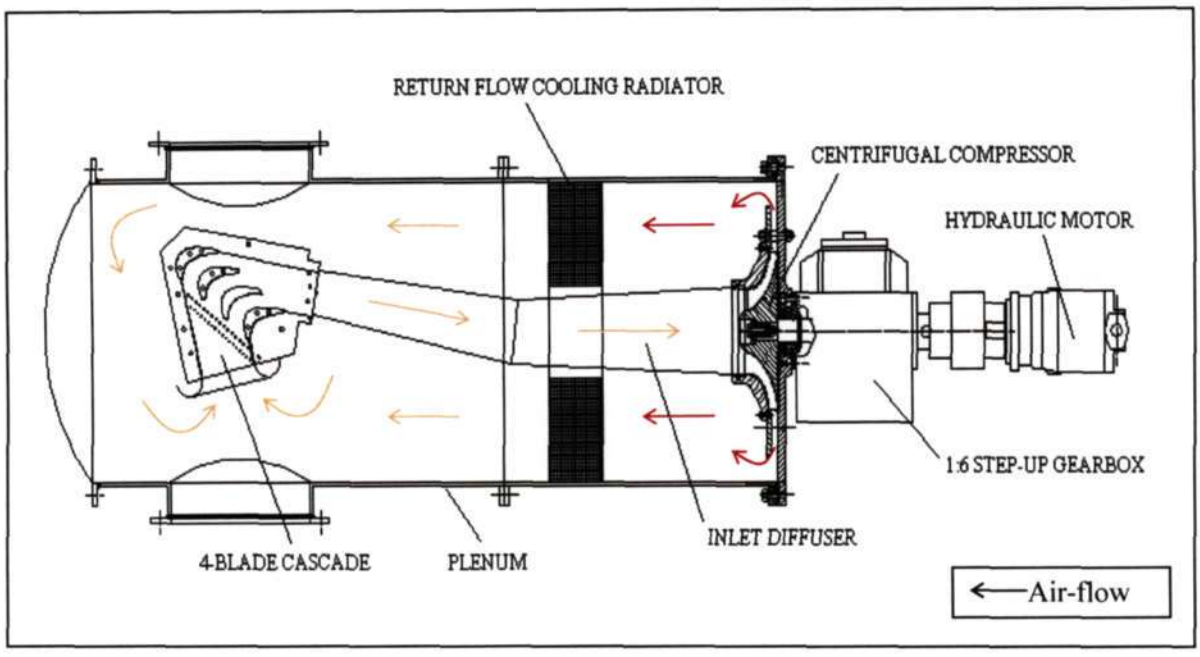

Figure 4-1 Top view of the high speed experimental facility (reproduced from de Villiers (2002))

The principal of operation depicted above in figure 4-1, shows how the air is sucked in through the bellmouth of a high turning angle 4-blade cascade, accelerated towards the eye of the compressor through the angled diffuser and expelled radially back into the plenum. The air is therefore re-circulated within the plenum creating high speed steady state continuous flow conditions which is used as the basis for experimental testing.

4.2.1 Plenum

The plenum, ideally a vacuum chamber that is only 0.6 m in diameter and 1.55 m in length, houses an instrumented 4-blade cascade, angled diffuser, annular cooling radiator and centrifugal compressor. Entrance to the cascade and diffuser is made possible through a dished end located at its front which is held together by 40 bolts and made air tight using a fibrous

gasket. To gain contact with the radiator, the plenum may be split at its mid section which is also sealed using a fibrous gasket and an extensive number of bolts. The back of the plenum is a flat section that interfaces with the gearbox and contains a mechanical carbon seal which allows the compressor shaft to enter the plenum. There are four Pyrex viewing portals of which two are located in the front test section and two at the rear compressor section which may also be used for access. An additional four access ports are used for the instrumentation of the cascade such as thermocouple cables, pressure tappings and heat flux gauge leads. All portals and windows are sealed using a combination of silicon sealer, silicon grease, rubber O-rings, neoprene seals and large clamping forces to ensure that the chamber is completely isolated.

The operation of the rig requires that the pressure of the plenum range between 0.25 and 0.4 bar absolute, the latter being the pressure at which experimental testing occurs. This is necessary due to the relatively inexpensive nature of the drive equipment used to attain the required Mach numbers. By reducing the total pressure within the plenum, the density of the air will drop thus reducing the amount of power required by the compressor to re-circulate the air. This relationship is shown below in equation 4.2.1.1, by the formula of an ideal gas. Another advantage is the ability to control the Reynolds number which is based on chord length. This is true based on equation 4.2.1.2, which shows the relationship between Reynolds number and density.

$$\rho = \frac{P}{RT} \tag{4.2.1.1}$$

$$\mathrm{Re} = \frac{\rho DU}{\mu} \tag{4.2.1.2}$$

In the equations shown above, P and T are the respective pressures and temperatures at a point, ρ is the density of the working fluid, μ is its viscosity, R is a proportionality constant, D is the chord length of the blade, U is the velocity of the fluid and Re is the Reynolds number.

The vacuum level in the plenum is thus a fundamental requirement for the operation of the rig and great difficulty was encountered in attaining these levels. The restoration of the facility saw that the mechanical carbon seal mounted on the compressor shaft had been eaten away by a corrosive build up caused by a damaged radiator. A cross sectional view of the compressor mounting and seal is given in Figure 4-2. The result is a vacuum being created within the

interfacing gearbox and gear oil being sucked in the plenum. The damaged radiator had also caused an extensive build up of corrosion along the walls of the plenum and associated equipment like the cascade and blower.

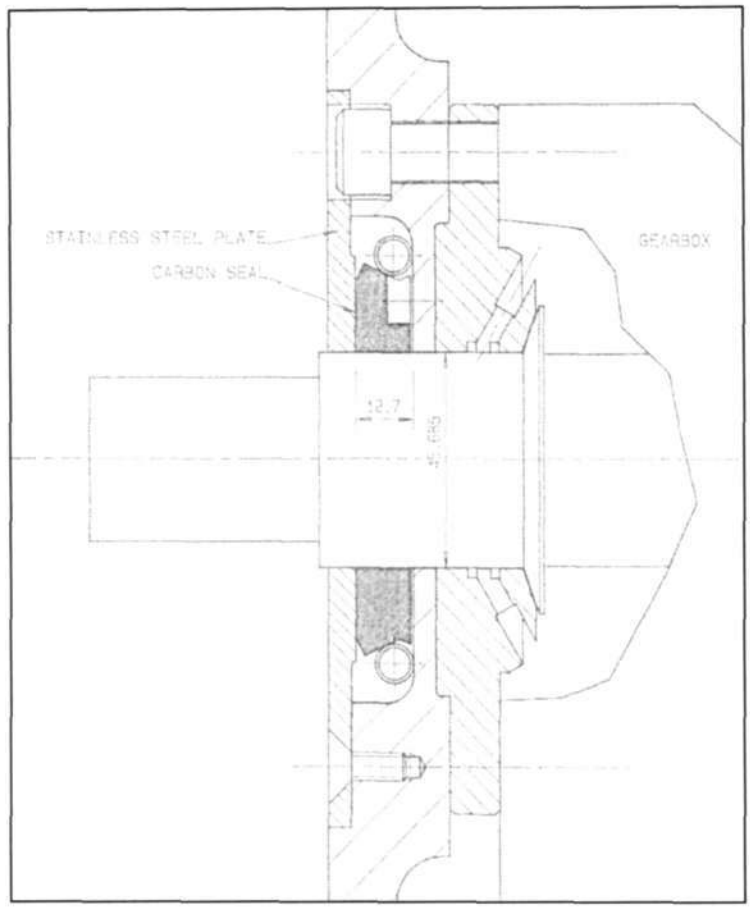

Figure 4-2 Cross sectional view of compressor mounting

The compressor shaft was reground to remove the corrosive build up and the three 120^0 carbon segments of the mechanical seal, which is held together by a torsion spring were relapped to minimise clearance and suit the newly ground shaft. The plenum was sanded down to remove the corrosion and sprayed with a heat resistant aluminium coating as the temperatures within the plenum reached levels of approximately 120 °C.

4.2.2 Vacuum Pump

The plenum is evacuated to controllable pressures using a continuously running Rietschle VCE 25 submerged oil vane vacuum pump. This pump is connected to a shell and tube heat exchanger which is in turn connected to the plenum. The reason for the heat exchanger is to

prevent over heating of vacuum pump as the air evacuated is at relatively high temperatures during test conditions. The vacuum pressure in the plenum is continuously controlled by a control system implemented by G.S Kennedy that replaced the system designed by Stieger (1998), which was based on a comparator with built in hysteresis known as a Schmidt Trigger. The current system uses a WIKA, 4-20mA pressure transducer that monitors the total pressure within the plenum by sending the corresponding voltage signal to a digital controller located within a 'yoke box'. The controller is made up of a digital display of gauge pressure that can be easily used to select the desired vacuum levels, and a temperature display which is used to display the cascade inlet total temperature. Thus, when the pressure reaches its user defined value, the control circuit sends a signal to close a solenoid valve mounted on the heat exchanger, disengaging the pump. Natural leakages into the system will therefore increase the pressure of the plenum resulting in the solenoid valve reopening and the vacuum pumps evacuation re-engaging. This system ensures stability in pressure during test conditions and does so with an accuracy of about ± 0.1 Kpa.

4.2.3 Centrifugal Compressor and Hydraulic Drive

A centrifugal compressor is mounted on the back plate of the plenum and is driven by a 65 kW hydraulic motor through a 1:6 step up gearbox. The compressor draws air axially through the angled diffuser of the cascade which is spigoted to its eye, and expels this air radially back into the plenum before being sucked back into the cascade through its bellmouth, as shown in Figure 4-1. The hydraulic motor is supplied with power from a Uchida swash-plate pump that is located in the second lab adjacent to the rig. The speed of the motor is governed by the flow rate of oil supplied by the Uchida pump and this is varied by changing the angle of the swash-plate via a mechanical lever. The lever is connected to a powerscrew which is operated by a DC motor and controlled remotely in the experimental laboratory via a switch. The switch is located on the display box and allows for fine and coarse speed control by regulating the polarity and amount of current supplied to the DC motor. The rotary motion of the DC motor is thus converted to a linear displacement by the powerscrew which mechanically varies the angle of the swash-plate and controls the speed of the compressor. This is illustrated in Figure 4-3 below, which shows the interaction of the various components used to remotely control the oil flow rate of the Uchida pump. The maximum speed of the motor is 3000 rpm, allowing the centrifugal compressor to reach speeds of up to 18000 rpm through the gearbox. These speeds result in high air velocities and realistic engine Mach numbers being set up within the cascade for experimental testing.

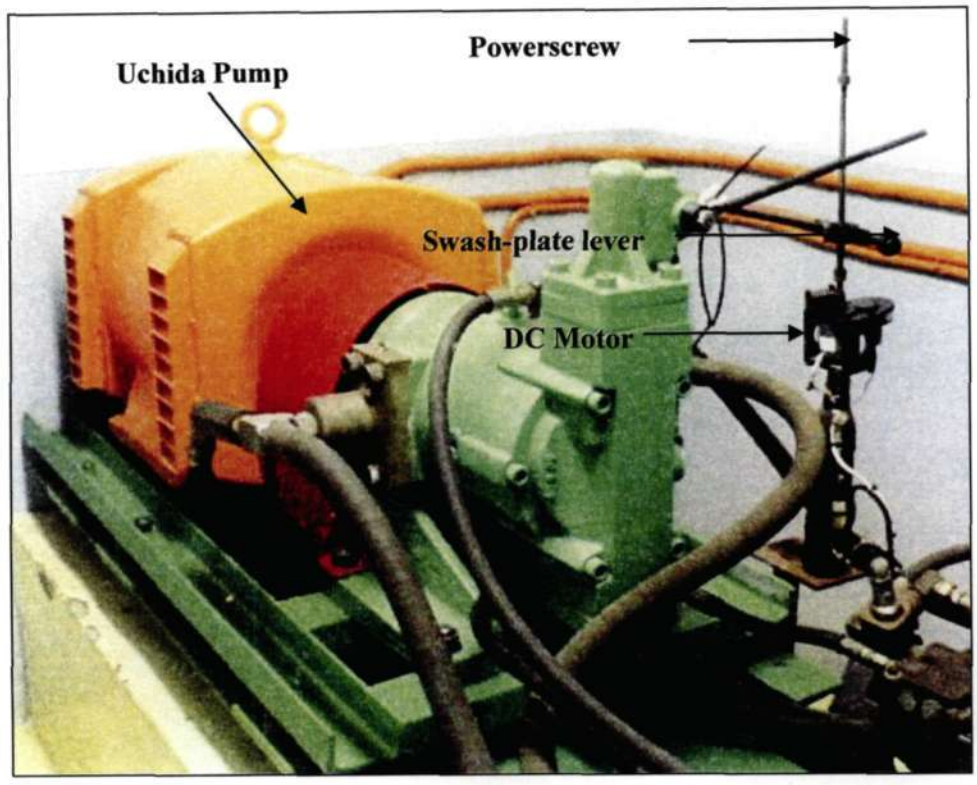

Figure 4-3 Uchida swash-plate pump

In order to start up the hydraulics of the system, various safety interlocks have to be deactivated to ensure that no damage to the components occurs. These locks monitor the plenum vacuum levels, air pressure, oil pressure, and oil flow to the gearbox to ensure adequate lubrication and ensures that the compressor is not overloaded. The safety circuitry is discussed further in section 4.2.7. If all of these safety conditions are satisfied, a fault free system is attained and it is displayed on the start up box allowing the hydraulic pump to be activated. A compromise on any of the safety measures will result in the hydraulic motor being switched off. Before starting the hydraulic pump it is necessary to check if the hydraulic oil levels are within an acceptable range, the angle of the swash-plate is in its neutral position and that cooling water is being supplied. Once this is done the prime pump may be switched on followed by the actual pump itself.

4.2.4 Gearbox

A specially constructed high speed 6:1 gearbox is used drive the centrifugal compressor. The operation of the gearbox requires that a continuous flow of lubrication is provided to it and special provisions, like large return pipes were made to ensure that no oil build up occurs in the

gearbox. An air motor driven by the workshop compressor operating at 6 bar is used to provide the necessary lubrication requirements. The advantage in using this motor lies within its source as any power failures that may occur will result in sufficient lubricating oil still being provided for a short period of time allowing the compressor to come to a safe stop. The air motor draws heavy duty industrial gear oil i.e. MOBIL 627, at approximately 15 l/min from a 60 litre sump which is fitted with an electrical immersion heater used to achieve operating oil temperatures between 50 – 70 °C. The oil return path is interrupted by a shell and tube heat exchanger that allows for the control of the lubrication temperature within the specified range. Safety interlocks were also installed on the gearbox to ensure its lubrication requirements and prevent further damage to associated components. These include that of oil pressure, air pressure and a flow rate indicator of which if any are compromised, the shut down of the main hydraulics is initiated.

4.2.5 Cooling Radiator

As the air is passed through the centrifugal compressor, the waste heat generated results in the temperature of the air rising to approximately 120 °C. In order to achieve test operating conditions and prevent damage to components such as cables and hoses, an annular cooling radiator was slotted within the plenum to control the air temperature. The radiator which is made up of a copper core and brass tubing cools the air by regulating the amount of water supplied. The water flow is manually controlled by adjusting two valves, a stopcock being the primary supply and a ball valve next to it that allows rapid switching of the cooling water.

The radiator which had been severely plagued with corrosion resulted in water re-circulating within the system. This promoted further corrosion to equipment including the cascade, plenum, blower and compressor shaft which lead to seizure of the blower and failure of the compressor seal. The damage to the radiator was to such an extent that the leaks could not be repaired. A new core together with tubing was thus fitted to prevent further damage to the equipment.

4.2.6 Secondary Cooling

The method of determining heat transfer results is done by plunging a pre-cooled instrumented test blade into a hot steady state cascade. The pre-cooling of the test blade takes place in a cooling box that is housed onto the four blade cascade. The cooling box, shown below in Figure

4-4 is made of steel and has a lid which makes provisions for two copper inlet ports that allows for cooling air to enter and a hole which allows for the free sliding motion of the pneumatic ram used to displace a dummy blade with an instrumented test blade. The box, not being completely sealed ensures that no cooling air is pumped into the cascade via the blade cut profile endwall which may lead to flow disruptions and compromise experimental data. This box is however filled with layers of polyurethane foam to minimise the heat transfer to the surrounding flow conditions which is at approximately 100 °C during test conditions.

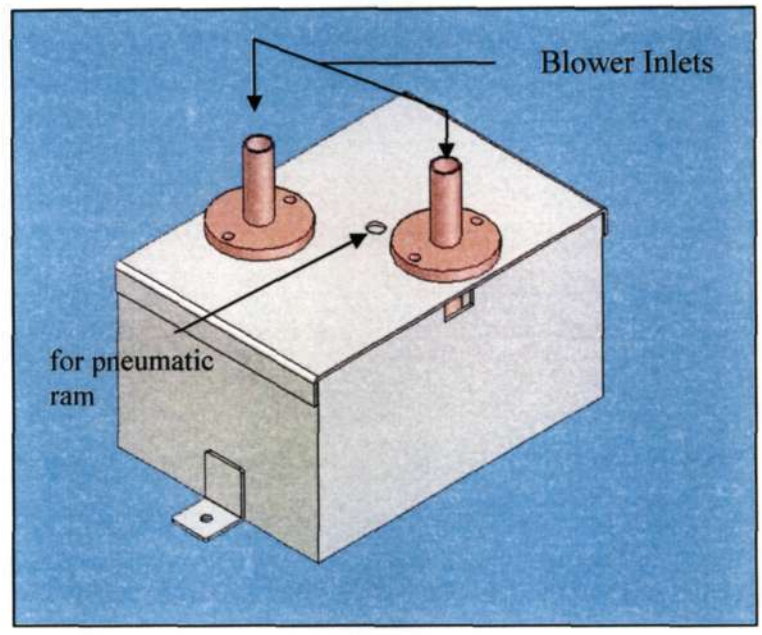

Figure 4-4 Cooling box

The cooling air used to chill the test blade is extracted from the plenum. This is done to maintain the pressure within the plenum, as the usage of an external source will pressurise the system and result in a loss of vacuum pressure initiating shut down of the rig. The secondary cooling circuit extracts air from a drain located at base of the plenum and passes it through a shell and tube heat exchanger where the air is cooled against water. The air is sucked through a DC motor driven Effepizeta lateral channel blower and passed through another shell and tube heat exchanger to achieve air temperatures of approximately 20 °C seen by the cooling box. The cooling box is maintained at temperatures between 25 – 30 °C, achieving realistic blade to free stream temperature ratios of about 0.8 under test conditions. It should be noted that operation of the blower under non test conditions with air at atmospheric conditions will result in the driving DC motor to trip. This is because the density of the air at atmospheric conditions causes an increase in the load capacity of the DC motor to such an extent that the proportional increase in current surpasses its design limits.

This system marks a significant improvement over the first cooling circuit design by McDonald (1994), which utilised a turbocharger unit running on the workshop compressor that supplied air to the cooling box after passing it through four radiators. The replacement of that system was predominantly due to the problems associated with the simultaneous running of the turbocharger unit and air motor, as well as sealing against vacuum pressure on the inlet of the turbocharger and turbocharger itself, indicated by Snedden (1995). The current system however, being improved does exhibit inefficiencies in its design. The usage of a drain located at the base of the plenum usually results in water being sucked up by the blower and passing into the cooling box. The result is a corrosive build up on the blower's casing and blading as well as water being lodged within the instrumented section of the test blade. The damaged radiator mentioned previously in section 4.2.1 and 4.2.5, had caused such an extensive build up of corrosion within the blower that the driving DC motor was subjected to increased loading conditions, as a result of the tight clearances existing between the blading and casing. This caused the motor to continuously trip under test conditions.

Both the casing and blading of the blower were then stripped and wire brushed to remove the corrosive build up. These components were then given a coat of primer to prevent the inevitable reformation of rust.

4.2.7 Control and Safety Circuitry

The safe operation of the experimental facility and its equipment is ensured by the usage of a series of safety circuits. These circuits as mentioned earlier in sections 4.2.4 and 4.2.1, monitor the air pressure, oil pressure and oil flow to the gearbox as well as the vacuum pressure within the plenum respectively. This is necessary to ensure that the gearbox is continuously lubricated and the compressor is not overloaded. A compromise on any of the safety features installed will result in the shut down of the systems main hydraulics to prevent damage to equipment. In order to initiate start up of the facility, all the safety parameter LED's located on the control box shown in Figure 4-5, must switch from red to green. This is done by achieving sufficient air pressure to the air motor which is supplied by the workshops Hydrovane compressor and a vacuum level of 0.55 bar absolute within the plenum. A Kulite ITQ-1000 (0-100 mV) absolute pressure transducer provides the signal for the pressure control circuitry and gives a digital read out on the display box located adjacent to the control box.

This display box shown in Figure 4-6, has digital readouts for oil pressure, oil temperature, inlet total and static pressures as well as the hydraulic motor speed. The display of oil temperature

and pressure is used to monitor and ascertain whether the gearbox is within a safe operating zone, being 50 – 70 °C and 80 – 100 kpa respectively. These measurements are taken at the oil inlet to the gearbox. The hydraulic motor speed is measured using a tachometer and the digital readout is given in RPM. The box also makes provisions for remote speed control of the hydraulic motor by a switch which allows for fine or coarse adjustments, plus an emergency stop button.

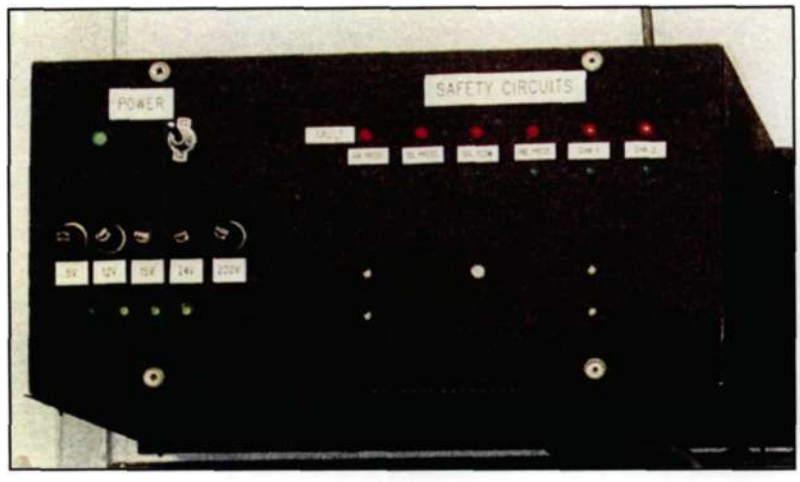

Figure 4-5 Safety control box

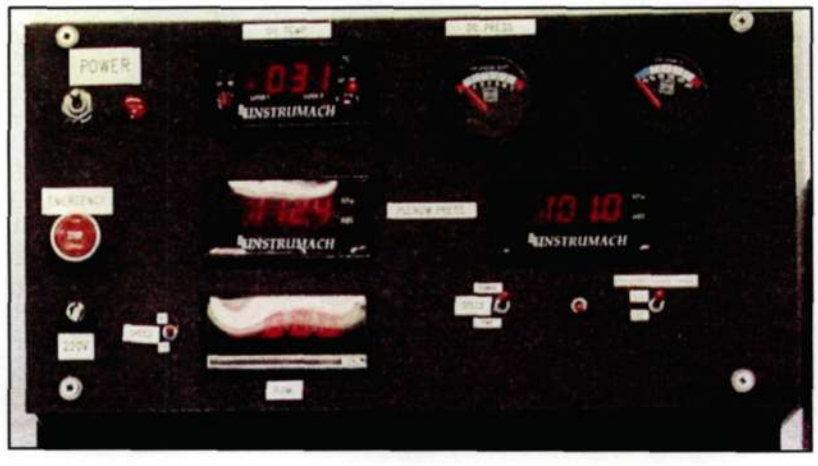

Figure 4-6 Display Box

4.3 The HTA Four-Blade Cascade

The cascade used for the experimental testing in this dissertation consists of three aluminium blades that are held in place between two 6mm wire cut end walls by two through bolts and cap

screws at each end. The end walls are machined with close tolerances to accommodate a fourth instrumented test blade which is used for determining either the static pressure or heat transfer distribution around the profile. The cascade has an inlet bellmouth with a square flange at the exit which is bolted to the inlet diffuser of the compressor. The pressure and suction side tailboards are fixed but provisions were made to accommodate an adjustable tailboard. The consequence of using an adjustable tailboard is that the cascade looses periodicity. This is given in Snedden (1998). A 3-D view of the supersonic cascade is shown below in Figure 4-7.

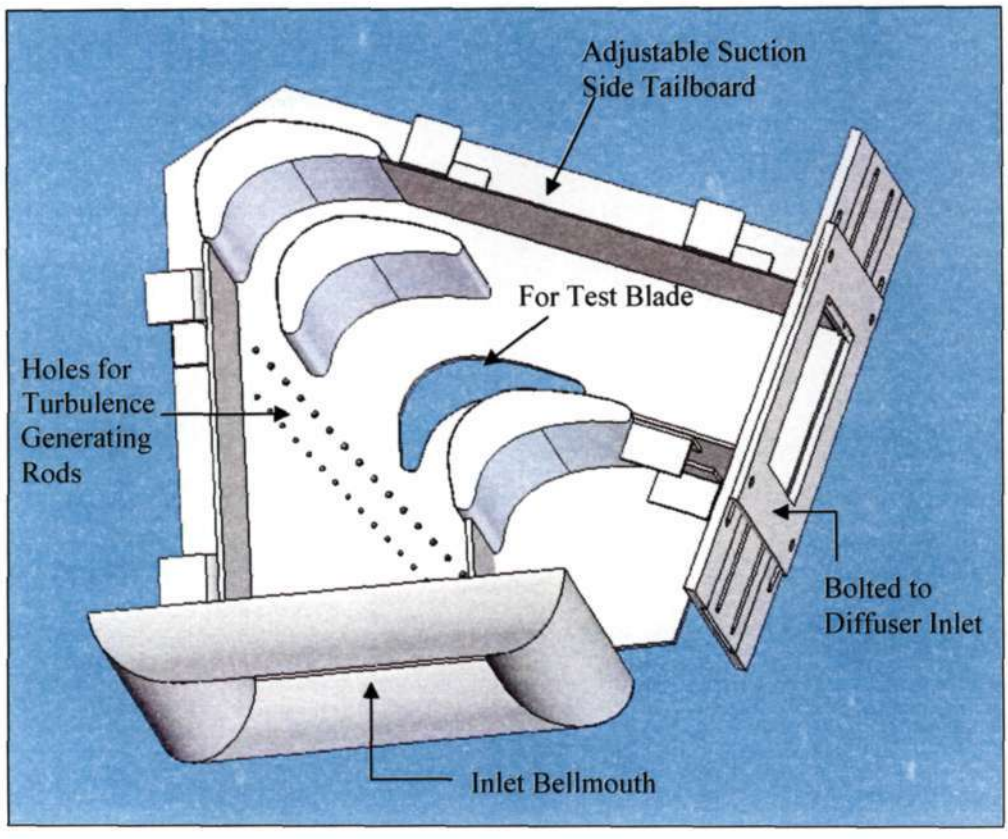

Figure 4-7 A 3-D View of the Supersonic Cascade

The profile used in the cascade is that of the high turning angle SMR-95 profile. The aerothermal details of the original blade are presented below in Table 4-1 and the scaled up details used in the cascade are given in Table 4-2. The rotor test blades were manufactured by Snedden (1995) and its co-ordinates are presented in Table A1-1. The cascade has provisions for two sets of vertical rods which may be inserted separately from each other. These rods are used to generate free stream turbulence. The measured turbulence intensities investigated by Stieger (1998) were 3% for a clean inlet, 15% for the 2.4mm diameter grid and 25.5% for the 3.2mm diameter grid.

Table 4-1: Original Blade and Aerothermal Properties (reproduced from Snedden (1995))

	Inlet	**Outlet**
Relative Gas Velocity[m/s]	410.46	613.72
Static Pressure [kPa]	796.89	603.5
Static Temperature [K]	1304.5	1216.1
Relative Mach No.	0.581	0.8997
Relative Reynolds No.	597713	756284
Relative Flow Angle [°]	38.4	28.6
Chord [mm]	33.27	N/A
Pitch [mm]	21.33	N/A
$T_{wall}/T_{freestream}$	0.86	N/A

Table 4-2: Test Blade Details (reproduced from Snedden (1995))

Blade Chord [mm]	94.8
Pitch/Chord ratio	0.675
Camber Angle [°]	113
Blade Span [mm]	80
Leading Edge Diameter	10
Scale Amplification	2.85

4.4 Pressure Measurement Equipment

In order to obtain a static pressure distribution around the SMR-95 profile various instruments are required. These include an instrumented test blade, a scanivalve, pressure transducers and a data acquisition system. These instruments are discussed in detail below.

4.4.1 Static Pressure Measurement Test Blade

The measurement of the blade static pressures are performed using an instrumented test blade with 42 pressure tappings. The pressure tappings are 0.5mm in diameter and drilled

perpendicularly to the blade surface along its midspan. The pressure surface has 20 tappings and the suction surface has 23 with the last tapping on the trailing edge being connected. The static pressures are measured using a scanivalve and three pressure transducers. Figure 4-8 shows the layout of the pressure tappings and Table 4-3 shows the circumferential positioning of the pressure tappings.

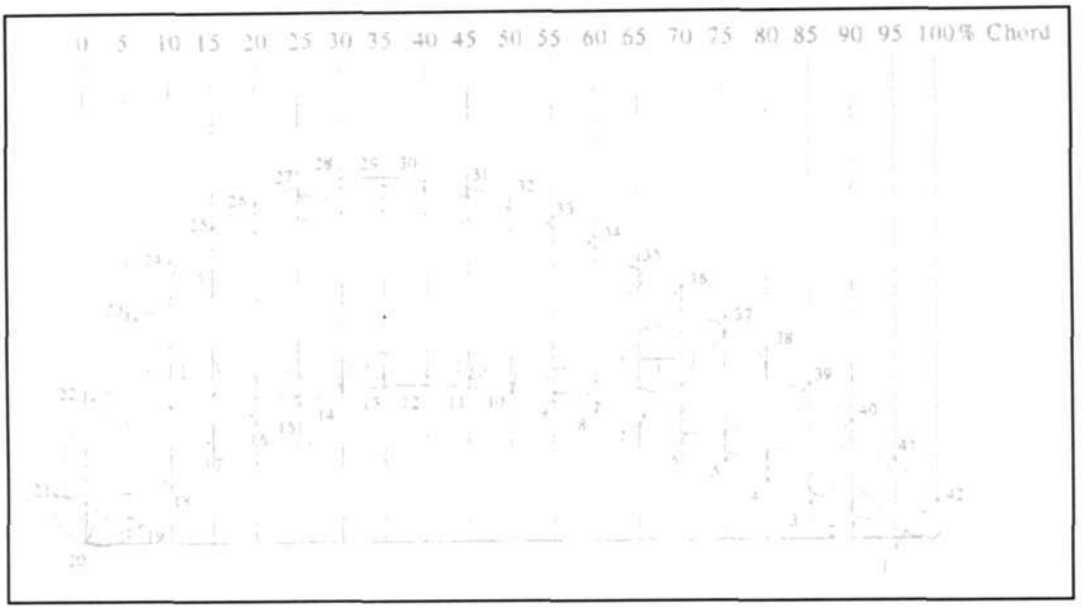

Figure 4-8 SMR-95 static pressure tapping positions (reproduced from Snedden (1995))

Table 4-3: Circumferential positioning of the pressure tappings on the SMR-95 (reproduced from de Villiers (2002))

Tapping Number	Circumferential Position (mm)	Tapping Number	Circumferential Position (mm)	Tapping Number	Circumferential Position (mm)
1	-101.5	15	-30.4	29	65.7
2	-96	16	-24.6	30	70.5
3	-90.5	17	-19.4	31	75.4
4	-85.1	18	-12.7	32	80.4
5	-79.5	19	-7.1	33	85.6
6	-74.4	20	0	34	90.8
7	-69.4	21	7.7	35	96.5
8	-64.2	22	20	36	102.3
9	-59.2	23	31	37	108.3
10	-54.4	24	39	38	114.5
11	-49.6	25	45.4	39	120.9
12	-45	26	50.8	40	127.4
13	-40	27	56.1	41	133.9
14	-35.5	28	60.7	42	141

4.4.2 Scanivalve

The scanivalve is a pressure measurement device that allows for the capturing of multiple pressure readings. It consists of two 1 pole – 24 throw fluid switch wafers that allows for 24 readings to be recorded in turn by a single pressure transducer. This is accomplished by switching 24 ports on the stator of the wafer in turn to a common port located on the rotor which is connected to a pressure transducer. Since the scanivalve has two fluid switch wafers allowing 48 pressure measurements to be recorded, the entire blade surface can be mapped in a single experimental run. Another port located on the cover is used to act as a pneumatic rotor thrust bearing enhancing sealing in the wafer. This is achieved when the port is supplied with a balance pressure equal to or greater than the average pressures being measured.

Silicon and PVC tubes are connected from the pressure measurement test blade to the stator ports of the respective wafer i.e. pressure side tappings to wafer 1 and suction side tappings to wafer 2 or vice versa. The inlet and outlet static pressures were also connected to the stator ports of the scanivalve measuring the pressure surface values. The total inlet pressure measured by a Kiel probe was then used to act as a supply of balance pressure to the scanivalve. Tubes were then connected from the rotor common ports of the wafers to two Rosemount pressure transducers.

The stepping of the scanivalve is achieved by the use of a stepper motor. This stepper motor rotates a single step once 24 volts is switched across its coil. This is achieved by supplying a 5 volt signal for 100 ms to a relay. The control wafer present within the stepping motor has a ratchet system that ensures the rotor is turned to its correct position. Details of the scanivalves control circuitry and wiring are given in Stieger (1998). A picture of the scanivalve is given below in Figure 4-9.

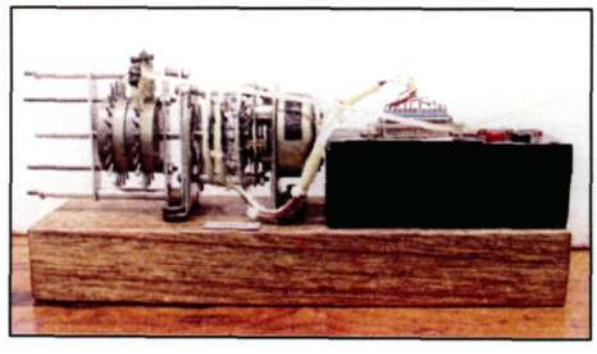

Figure 4-9 Scanivalve

4.4.3 Pressure Transducers

Two Rosemount 1151 Range 5 differential pressure transducers are used to measure the static pressure distributions around the profile of the SMR-95. The transducers operate in a closed loop system where it is supplied with a voltage input from the scanivalve and it outputs a current (4-20 mA) which is proportional to the differential pressure supplied. The output current is passed across a 470Ω resistor of which the voltage (1.88 – 9.4V) read across the resistor is captured by the data acquisition system.

These transducers have two ports i.e. a LP (low pressure) side and a HP (high pressure) side. The LP side is connected to the common port of the scanivalves rotor and the HP side is connected to a 0-100 mV Kulite ITQ – 1000 pressure transducer used to measure the cascades total inlet pressure. The output from the Rosemount transducers is therefore the difference between the cascades total inlet pressure and the blades static pressure. The captured voltages are then converted into pressures by the data acquisition system which is based on the respective transducers calibration data. The blades static pressures are then calculated by subtracting the output pressures with the cascades total inlet pressure.

4.4.4 Pressure Measurement Data Acquisition System

The pressure measurement data acquisition system is made up of a PC 71 interface card, a PC 30 PGL A/D card and LABview software. The output voltage readings from the scanivalve are input into a PC 71 interface card. This card, implemented by the author has significant benefits over its predecessor, which was the PC 30 U protection card used predominately to serve as a voltage protection card to the PC 30 PGL A/D. The use of the PC 71 interface card offers improved noise reduction, reduced ground noise pick up, easy interfacing, and voltage protection.

The voltage signals from the Rosemount pressure transducers that are fed into the scanivalve and then via a manually wired 32 pin D-type connector, connected to channels 0 and 1 on the PC 71 interfacing card. The jumpers corresponding to the channels in use are then removed to allow for LABview software to read the voltages. To ensure correct operation of the PC 71 card, a lug must be grounded from the card to the computer casing.

The PC 71 card is then connected to the PC 30 PGL A/D card, which is used to supply and record all signals relating to the data acquisition system. The PC 30 PGL card is jumpered to allow for differential input as this reduces the noise levels when sampling through a single ended channel. The available 8 analogue inputs were then set to read for 0-10V unipolar inputs, which was based on the output of the respective pressure transducers. It should be noted that numerous problems associated with the cards operation were encountered. These include blown fuses and operational amplifiers amongst others. The manufacturers of the card (Eagle Technologies) were contacted and the result was a replacement at no charge.

The acquisition and processing of all the experimental data occurs using an object oriented LABview program that was written by de Villiers (2002). The program is responsible for the stepping of the scanivalve rotor, the digital reading of the position of the rotor, and the reading of the voltages from the pressure transducer. The program also converts the transducer voltages into meaningful differential pressure readings through the use of pre-inputted transducer calibration data. The program and its sub-programs include Virtual Instruments (VI) which were developed by Eagle Technologies to provide an easy interface between LABview and the PC30 PGL card.

The program consists of various functions, such as "Go Home" which is used to check if the scanivalve is in its correct starting position before a test is run. If this is not the case, the program will step the scanivalve until the rotor is in its starting position. A "Step Once" command is used to step the scanivalves rotor to check if the PC 30 PGL card and its associated equipment is operating correctly. The "Perform Measurement" command is used to acquire the respective pressure measurements by stepping the scanivalve, reading the transducer voltages and then finally converting the voltages into to a pressure value. A detailed description of the program and its operation can be found in Appendix 2 of de Villiers (2002).

4.5 Heat Transfer Measurement Equipment

The heat transfer measurement equipment is made up of a heat transfer test blade stack which is fastened to a sliding mechanism that allows for the transient measurements of heat transfer. A heat transfer analogue and data acquisition system is then used to process the acquired results brought about by the transient conditions.

4.5.1 Heat Transfer Blade Stack

The heat transfer blade stack, shown in Figure 4-10 is made up of a number of sections that are held together by two tie bolts. The un-instrumented bottom section of the blade stack is made up of aluminium and is used to serve as a dummy blade to which an instrumented section displaces. This dummy blade fills the void within the cascade, thus maintaining flow conditions while the instrumented section is cooled in the cooling box.

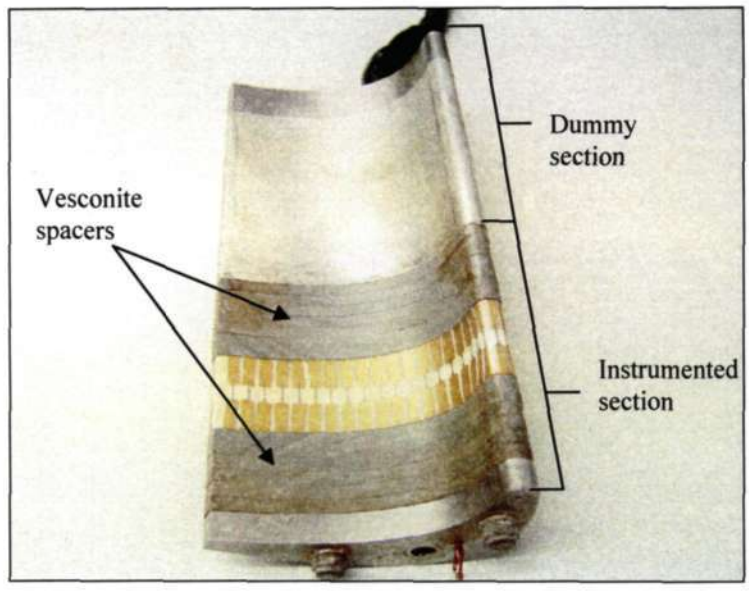

Figure 4-10 Heat transfer blade stack

The instrumented section of the blade stack consists of a number of Vesconite spacers that are machined to the profile of the test blade. These spacers surround an instrumented Macor section on either side preventing heat conduction from its aluminium counterparts. The Macor section shown in Figure 4-11, is the heart of the test blade and consists of 48 platinum thin film heat flux gauges that are painted on its surface. Flying gold lead attachments are connected to either side of each gauge and are in turn wired to 6 D-type, 25 pin connectors with each D-type connector consisting of eight sensors. The sensor numbers and its respective circumferential positioning are given below in Table 4-4. In addition to the heat flux gauges, there are four K-type thermocouples which are embedded within the Macor section to serve as an indication of plunging temperatures as well as to provide an understanding of the blades internal heat transfer conduction aspects. A description on the construction of the heat flux gauges can be found in section 4.7 of Snedden (1995), Ligrani et al (1982) and section 6.3.1 of this dissertation.

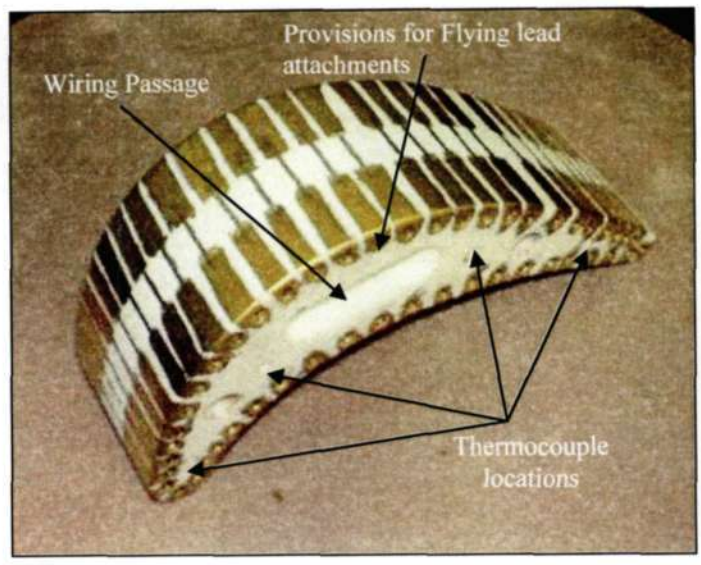

Figure 4-11 Macor test section

Table 4-4: Thin-film heat flux gauge positioning

Sensor Number	Circumferential Position (mm)	Sensor Number	Circumferential Position (mm)
LE 1	0.3	25	121
2	3.5	26	126.6
3	6.9	27	131.5
4	13	28	136.5
5	18.1	29	107
6	23.1	30	98.2
7	28.3	31	92.8
8	33	32	87.6
9	37.8	33	81.9
10	43.1	34	76.2
11	48.3	35	70.8
12	53.3	36	66
13	58.4	37	60.4
14	64.3	38	55
15	69.4	39	49
16	74.6	40	44.5
17	79.5	41	38.9
18	84.5	42	33.5
19	88.7	43	28.2
20	94.4	44	22.7
21	99.7	45	17.3
22	105.4	46	12
23	110.5	47	6.7
24	115.4	48	3.7

4.5.2 Sliding Mechanism and Pneumatic Ram

The blade stack is fastened to a sliding mechanism at the bottom and to a pneumatic ram at the top. The sliding mechanism consists of a plate with four linear bearings, each running on nitrided rods. The sliding mechanism is connected to the underside of the cascade by two 10mm cap screws and is positioned to allow the heat transfer blade stack to slide freely through the cascade. At the end of the sliding mechanism are two 6 mm FESTO shock absorbers and a helical wound spring which both absorb the impact of the blade stack after plunging. A FESTO DSG-20-100-PPV-A pneumatic ram is bolted onto the top end of the blade stack and is used for firing and retracting the blade stack within the cascade. A two way solenoid valve which is actuated by an external switch is used to control the direction of the pneumatic ram. The helical spring was implemented by the author to assist in the retraction of the blade stack after firing. Its implementation was brought about due to the extensive amount of corrosion present on the nitrided surfaces which hampered the performance of the pneumatic ram upon retraction. Figure 4-12 shows a schematic of the sliding mechanism arrangement.

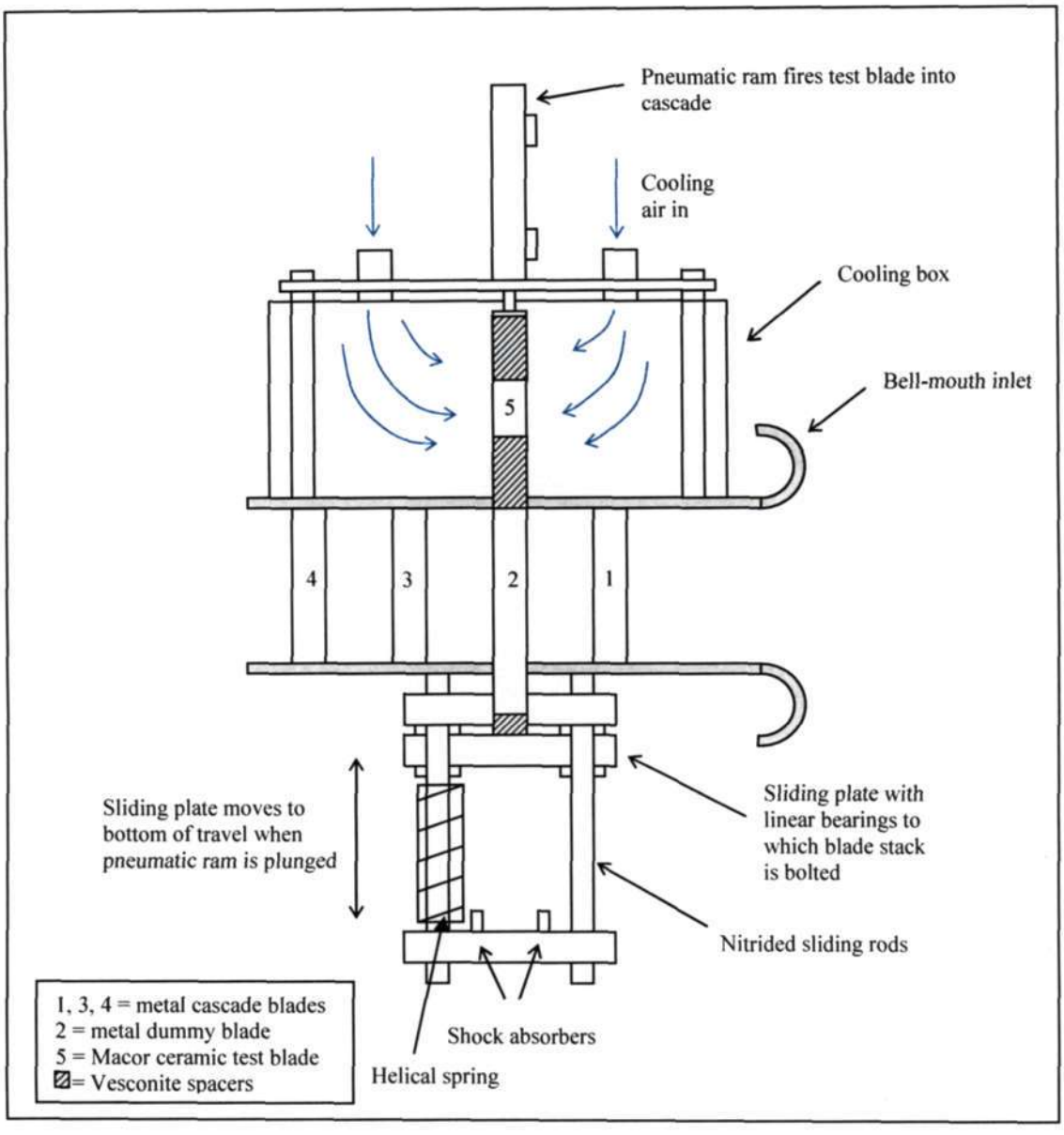

Figure 4-12 Schematic of the sliding mechanism layout

4.5.3 Heat Transfer Analogue and Data Acquisition System

The six 25 pin D-type connectors which are wired to the thin film heat flux gauges are pulled through an access port in the plenum and connected to a heat transfer analogue. The heat transfer analogue consists of 8 analogue cards which were based on the design of Oldfield et al. (1985) and implemented by Snedden (1995). The design of Snedden (1995) however includes modifications that allow for improved noise reduction. Each of the 8 cards in the heat transfer analogue sequentially corresponds to a sensor on the heat transfer blade stack. These cards in conjunction with the painted thin film heat flux gauges allow for the simultaneous measurement

of heat transfer from the blade surface. Each card is made up of a resistive-capacitive network that is designed to convert a varying voltage which is proportional to temperature into a current that is proportional to the heat flux. The details of the design and construction of the cards can be found in Appendix 5 of Snedden (1995).

Every card is powered by a ± 15V supply and produces a constant current to its corresponding heat flux gauge. The amount of current supplied by the analogy can by varied by adjusting a trimpot located on each analogue card. The heat flux gauges which may be described as variable temperature resistors therefore produce a varying voltage when exposed to a change in temperature, according to Ohm's law. The voltage is then passed across the analogy's resistive-capacitive network to produce a current proportional to heat flux. This current is then converted to a voltage, amplified and filtered of high frequency noise by a 0.01 Hz – 100 kHz bandpass filter. An analysis of the theory behind these cards can be found in Chapter 3 of this dissertation and the circuit diagram is presented below in Figure 4-13.

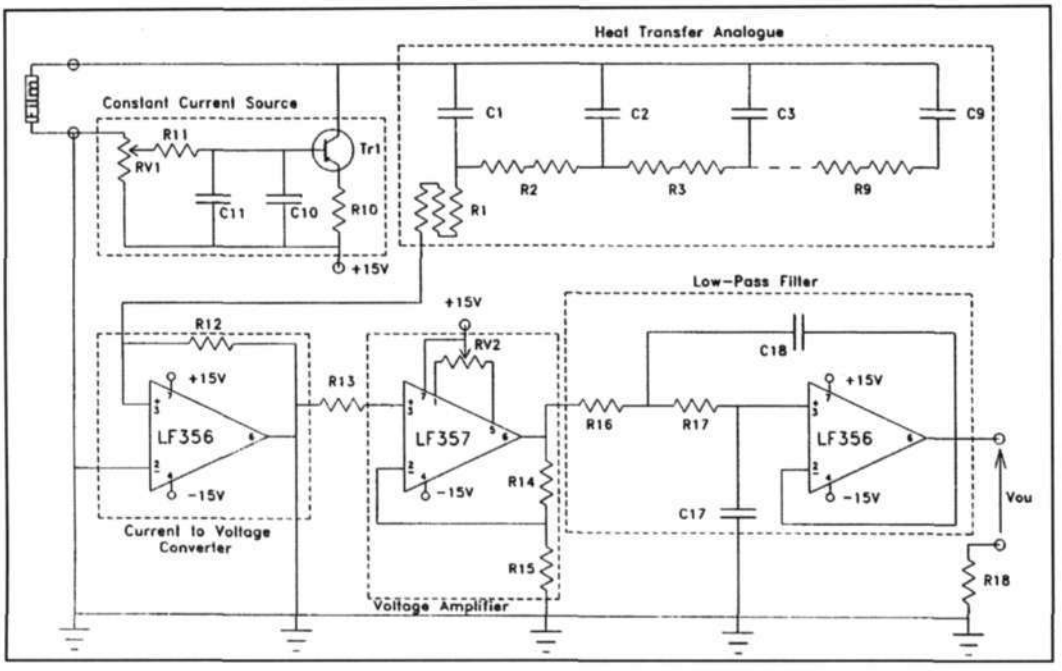

Figure 4-13: Electrical analogue circuit (reproduced from Snedden (1995))

The output from each card is then wired to a 32 pin D-type connecter which is connected to the 8 analogue inputs of the PC 71 interface card. The PC 71 card is then connected to the PC 30 PGL A/D card which is configured for a ± 5V bipolar output in differential mode. Waveview software is then used to view the outputs of the cards and capture the data. The sampling of the data occurs for 3s at 4000 Hz and is initiated when the pre-chilled blade displaces the dummy blade within the cascade.

Post processing of the sampled data to obtain the isothermal heat transfer co-efficient results occurs using LABview software. The program is called "Isotemp1" and was written by Snedden (1995). A detailed description of its operation and code can be found in Appendix 4 of Snedden (1995). The program is used to reconstruct the wall temperature history from the sampled data captured by Waveview. The isothermal heat flux is then calculated by plotting the corresponding heat flux versus temperature graphs.

The ISOTEMP1 uses the following procedure to acquire the isothermal heat transfer co-efficient:

1. Reads in the sampled data in text format (Note that there can be no headings or descriptions within the data text file and delimiters must be used to separate each channel's readings. This is done in Waveview)
2. Removes the time data from the voltage data and performs the calculation from the first acquisition time step
3. Separates each channel voltages and saves it separately to disc
4. Filters and trims the sampled voltages based on user defined instructions before saving the significant data
5. Converts the voltage readings to a corresponding heat flux using the calibration information entered by the user
6. Numerically reconstructs the wall temperature history from the heat flux data
7. Saves both the heat flux and temperature data and presents the final heat transfer coefficient results

CHAPTER 5

FEASIBILITY STUDY OF FILM COOLING

5.1 Introduction

An ambitious concept considered at the start of this project was to implement a film-cooled turbine test blade into the existing supersonic cascade facility. The goal of this project was to obtain static pressure and heat transfer co-efficient distributions over the surface of a film-cooled turbine test blade. In order to address the issues surrounding its implementation a feasibility study was thus undertaken. The purpose of this study was to assess the viability in terms of cost and time incurred towards its implementation.

The main areas surrounding this study are test blade and cascade design, a coolant supply line, and a capable data acquisition system. The profile of the test blade incorporating film-cooling technology was chosen on the basis of having well documented results. Naturally, a new turbine test blade would require the design of a new cascade. Both the test blade and cascade would therefore have to be capable of incorporating the existing experimental setup to aid in cost expenditure. Since a pressure distribution and heat transfer distribution is required, two separate test blades would have to be constructed to obtain the required results. Basic numerical simulations using the CFD package FLUENT, were to be conducted to aid in the design of the test blade and cascade. Although these simulations can not be validated against experimental data, the outcome of such simulations was to obtain general flow field data to provide support in the design of film-cooling.

A primary requirement of film-cooling is a supply of coolant flow to the test blade. This requirement saw that a modification to the experimental facility was in order. Various concepts were considered and the outcome was one which could be easily integrated with the experimental facilities general operation without causing damage to any components. The instrumentation of the respective test blades for pressure and heat transfer distributions was to be done in accordance with the existing SMR-95 setup. In doing so, the usage of the existing data acquisition systems could be possible with little or no modifications required.

It should be noted that above all these required needs and proposed solutions to accommodate for film-cooling; the most important is an operational experimental facility and effective data acquisition system, of which at the start of this project, neither was available.

5.2 Fundamentals of Film-Cooling

In order to design for film-cooling, one must have a basic understanding of such a complex cooling strategy. Goldstein (1971) describes film-cooling as "the introduction of a secondary fluid (coolant or injected fluid) at one or more discrete locations along a surface exposed to a high temperature environment to protect that surface not only in the immediate region of injection but also in the downstream region". Film-cooling prevents the blade surface from being exposed to the combustor exit temperature directly, and thus reduces the thermal stresses that the blade would otherwise be exposed to. The heat flux that the blade would experience in the absence of film cooling is given below by:

$$q_0'' = h_0\left(T_g - T_w\right) \tag{5.2.1}$$

where, q_0'' is the heat flux, h_0 is the heat transfer co-efficient and $\left(T_g - T_w\right)$ is the temperature difference between the oncoming gas and wall.

When film cooling is employed, the driving temperature is no longer gas temperature, T_g but rather the film temperature, T_f which is the temperature resulting from the mixture of hot gas to the coolant, as shown in Figure 5-1 below.

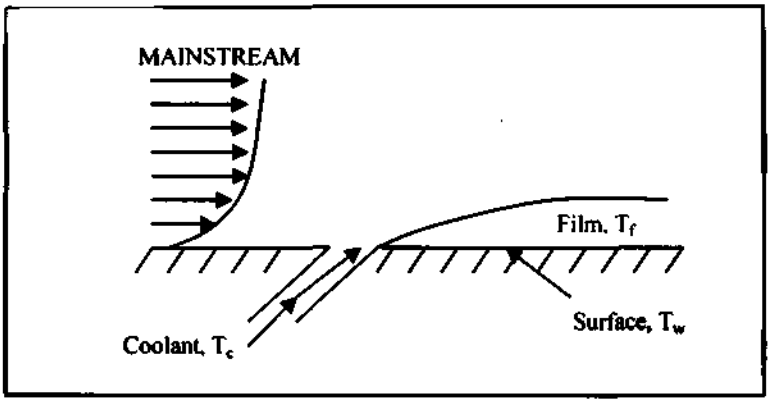

Figure 5-1 Coolant injection into a mainstream flow

Thus the new heat flux will therefore be given as:

$$q^{\cdot} = h(T_f - T_w) \tag{5.2.2}$$

Where, h is the heat transfer co-efficient on the surface with film injection and $(T_f - T_w)$ is the temperature difference between the film gas and wall.

The film effectiveness is given by:

$$\eta = \frac{(T_g - T_f)}{(T_g - T_c)} \tag{5.2.3}$$

Where T_c is the coolant temperature.

In order to design for effective film cooling the ratio of $q^{\cdot}$ to $q_0^{\cdot}$ should be less than 1, as shown below in equation 5.2.4

$$\frac{q^{\cdot}}{q_0^{\cdot}} = \frac{h}{h_0}\frac{(T_f - T_w)}{(T_g - T_w)} = \frac{h}{h_0}\left\{1 - \eta\frac{(T_g - T_c)}{(T_g - T_w)}\right\} \tag{5.2.4}$$

Many researchers such as Camci and Arts (1990) found that by introducing film cooling, the heat transfer co-efficient was lower than that of a regular, solid turbine blade. This reduction in heat flux is influenced by a variety of factors. The external factors that affect the film cooling effectiveness in normal operating environments are oncoming mainstream flow, blade wakes, rotation, secondary flow effects on endwalls, and tip flows. The configuration, coolant temperature, mass flow through the holes, and the film-hole geometry, also affect the film cooling effectiveness. A large amount of experimental test results for film-cooled turbine blades are achieved using a cascade and flat plate models which simulates engine flow conditions. These models have proved themselves to be extremely useful in determining the flow phenomena brought about by film-cooling.

5.3 Test Blade and Cascade Design

The first step into implementing a film-cooled turbine test blade into the supersonic cascade experimental facility is to choose a profile. Based on the profile, a new cascade would then have to be designed. The design of the cascade would be done using the CFD suite, FLUENT. Coolant holes on the test blade would then have to be incorporated into the CFD model to determine its optimal locations. Two separate test blades, one for pressure measurements and one for heat transfer predictions would then have to be constructed. The instrumentation of these blades would have to be such that it can be easily integrated to provide reliable experimental data using the existing data acquisition systems.

5.3.1 Test Blade Profile

The profile of the test blade was chosen on the criteria of having well documented heat transfer results with and without film-cooling. On dong so, one blade which has had a considerable amount of research performed on it was the high pressure gas turbine rotor blade used by Consigny and Richards (1982) and Camci and Arts (1985a, 1985b, 1989). As discussed earlier in section 2.2.1, Consigny and Richards (1982) performed short duration heat transfer measurements without film-cooling, investigating the effects of Mach numbers, Reynolds numbers, inlet flow angles and free stream turbulence levels on the heat transfer rate over the rotor profile. Camci and Arts (1985a, 1985b) furthered the study by implementing leading edge and suction side film-cooling, respectively. Camci and Arts (1989) furthered the study by investigating the effects of film cooling on the heat transfer rate by simultaneously ejecting coolant flow through the leading edge, suction side, and the pressure side. Numerous aspects such as the effects of overall mass weight ratio, coolant to free-stream temperature ratio and free stream turbulence on the heat transfer rate distributions were also successfully investigated by Camci and Arts (1989). The co-ordinates of this profile are given in Table A1-2. The blade and cascade details can be found in Consigny and Richards (1982), and the cooling configuration used by Camci and Arts (1989) is shown below in Figure 5-2.

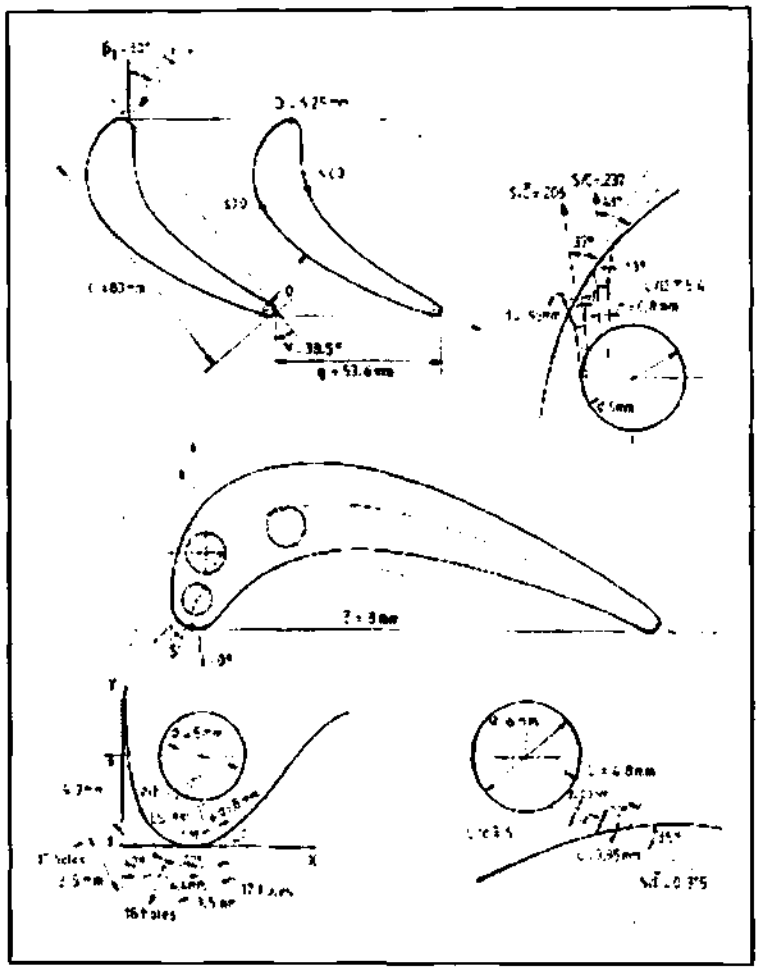

Figure 5-2 Cooling Configuration used by Camci and Arts (1989)

5.3.2 Cascade Design

The cascade was designed using the CFD package, FLUENT. In order to accommodate for the imposing space restrictions within the plenum of the experimental facility, a four blade cascade with blade chord length of 100mm was imported into FLUENT with geometry created in its pre-processor GAMBIT. A schematic of the proposed cascade is given below in Figure 5-3.

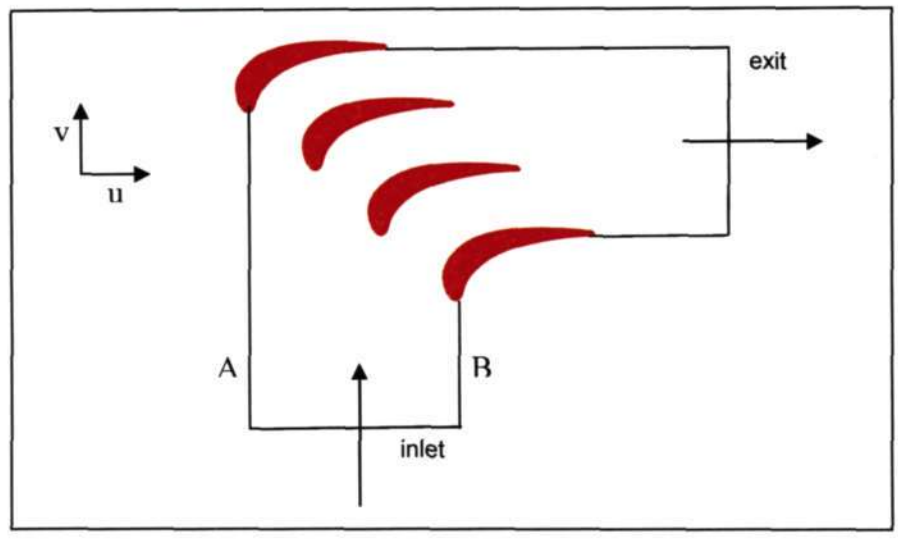

Figure 5-3 Schematic of the proposed cascade

The numerical simulations performed on the cascade were to output basic data such as general static pressure and velocity distributions. The main objective was to avoid recirculation within the cascade. A simple 2-D model was created and a coupled solver was used with an implicit formulation. The problems were solved for steady state conditions with an absolute velocity formulation and cell based gradient option. All simulations were carried out using the standard version of the $k-\varepsilon$ turbulence model with a turbulence intensity of 3%. The inlet of the cascade was modelled as a pressure inlet boundary condition with a total gauge pressure of 40 kPa and a total temperature of 373 K. The outlet of the cascade was modelled as a pressure outlet boundary condition with total gauge pressure of 30 kPa and backflow total temperature of 350 K. With the absence of experimental data, most of the required simulation parameters were estimated according to the available experimental data on the SMR-95 profile. For stability of the solution, the first order upwind scheme was used in the beginning, once stabilized a second order upwind differencing scheme was used.

Presented in Figure 5-4 and Figure 5-5 are the velocity vectors and static pressure distributions over the proposed cascade. After numerous simulations and geometry modifications, the simulation converged with no sign of recirculation. The design was thereafter put forward to accommodate for film-cooling effects.

The cascade could be manufactured using mild steel and given an enamel coating to prevent corrosion. It would consist of an inlet bellmouth cut from steel pipes, brackets, plates and side plates on either side to accommodate for the existing pneumatic ram and plunging device. The cascade exit would consist of a laser cut front connector that attaches to the compressor diffuser. An illustration of the proposed cascade is given in Figure 5-6

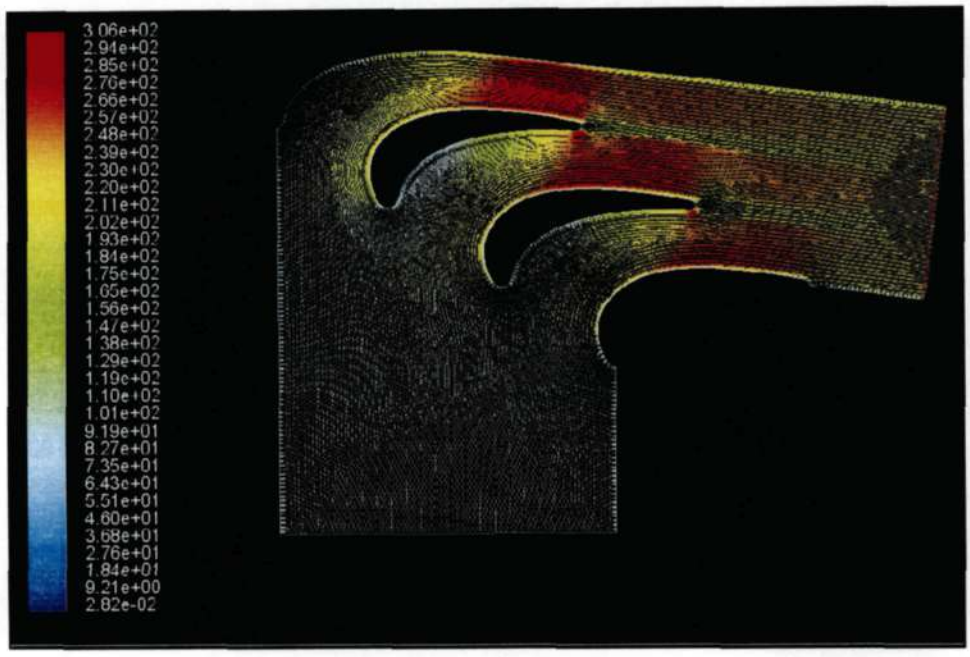

Figure 5-4 Velocity vectors for new cascade

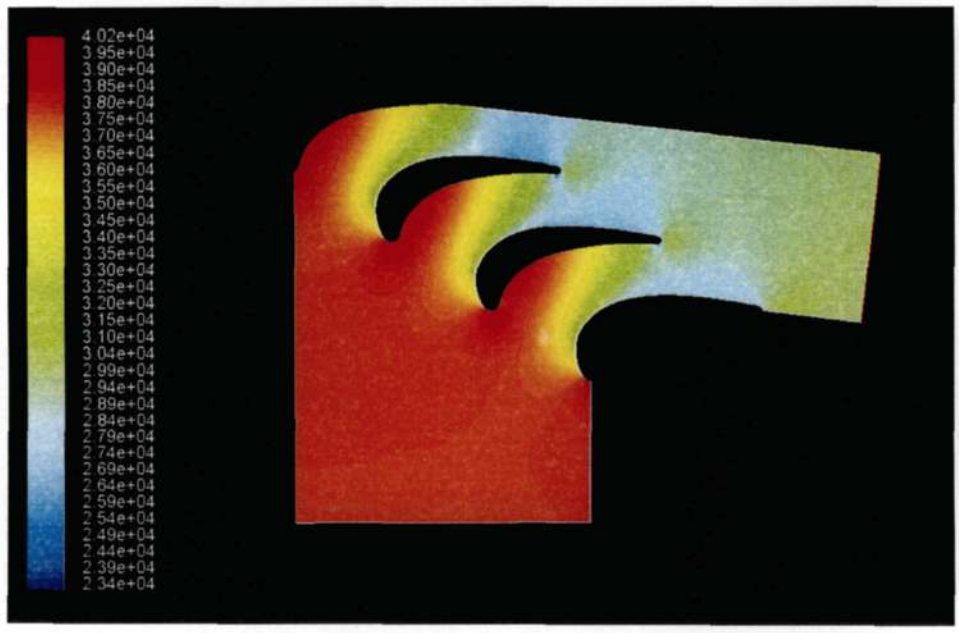

Figure 5-5 Static pressure contours for new cascade

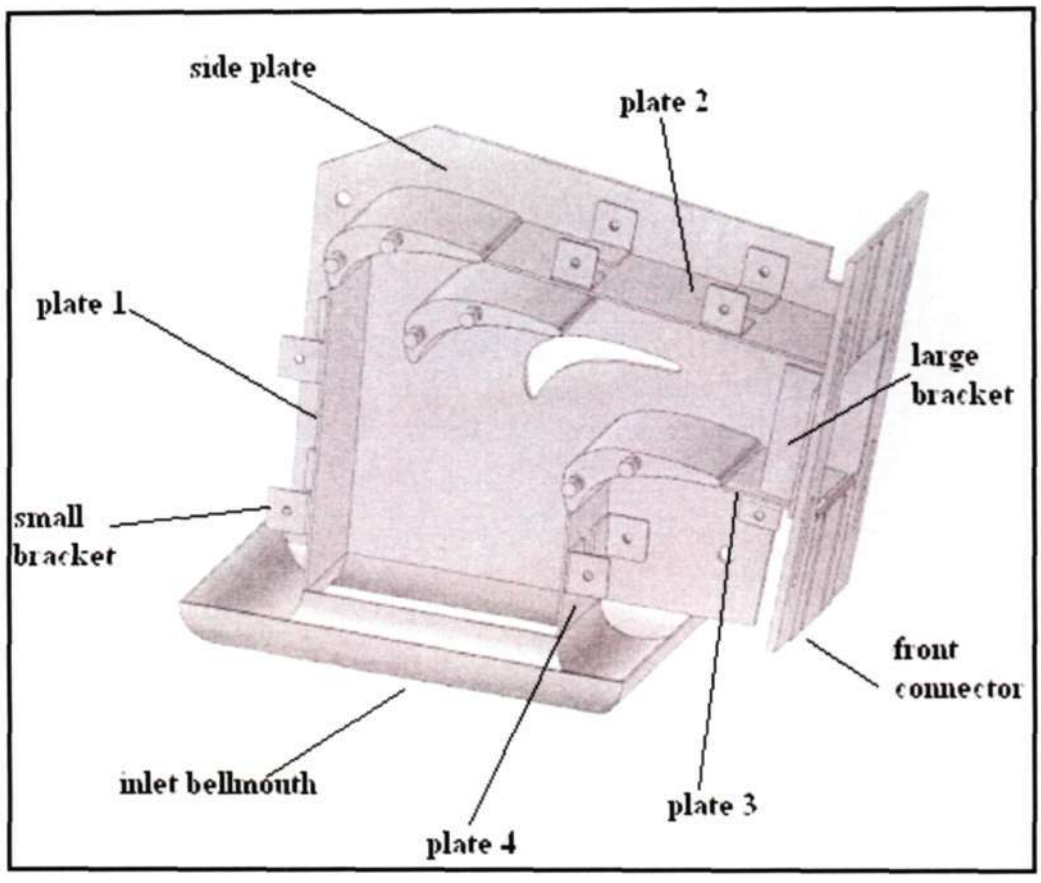

Figure 5-6 Proposed film-cooled cascade

5.3.3 Design for Film-Cooling

Designing the test blade for film-cooling is not an independent task. A suitable film-cooling design that protects the blade may be generated but may not thereafter be instrumented effectively. The design of a blade would therefore have to accommodate for film cooling, heat-transfer instrumentation and pressure instrumentation.

To employ the film-cooling, tiny chambers would be created within the test blade from which the film-cooling holes will lead to the blade surface. The use of independent chambers, instead of hollowing out large sections of the blade, allows for different coolant pressures. This is needed for different rows of holes as the pressure distribution over the blade surface varies. Also, provisions have to be made to accommodate for the wiring of the heat transfer blade stack.

It was proposed that the design incorporate leading edge film-cooling. Various concepts were generated and the two that were considered are shown in Figure 5-7 and Figure 5-8. The first concept was to use a single pipe running out from the blades internal plenum to the blade's

leading edge. This idea was seen as the most obvious approach however issues regarding effective blade surface cooling on both the pressure and suction side arose. This concept demanded that the orientation of the blade profile be ideal to avoid an overflow of coolant on a particular side of the blade. In order to increase the allowable orientation tolerances and provide better cooling effects, a second concept implementing two pipes from the blades plenum was considered. However, in order to better understand the flow dynamics of these arrangements, both these concepts were imported into FLUENT for analysis.

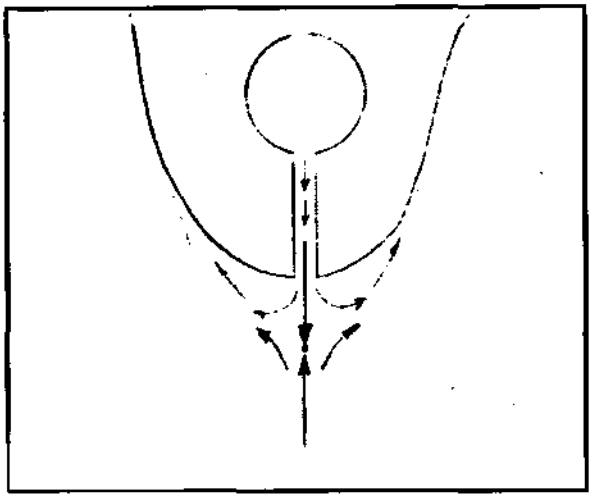

Figure 5-7 Leading edge film-cooling using a single outlet

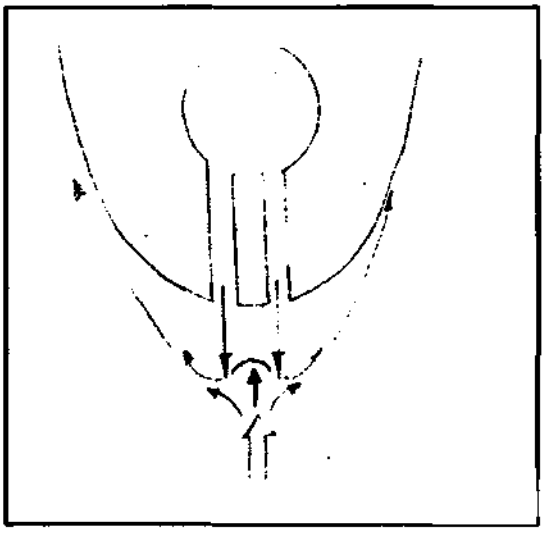

Figure 5-8 Leading edge film-cooling using two outlets

The mesh for the film-cooled cascade was set up in a similar manner to that of the previous cascade. The only difference was the addition of a chamber and cooling hole. The chamber and cooling hole were meshed with quadrilaterals. The chamber was set as a pressure-inlet and the pressure was set at 42kpa. A turbulence intensity of 1% and a viscosity ratio of 10 were implemented as suggested by the FLUENT 6.2 tutorial guide. A typical example of the meshing strategy used is presented in Figure 5-9 with the respective static pressure contours of the single outlet and double outlet given in Figure 5-10 and Figure 5-11.

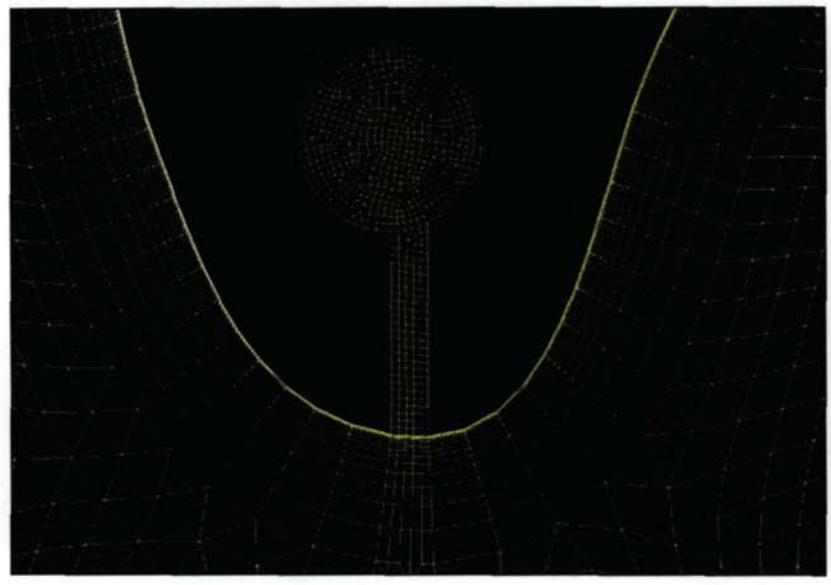

Figure 5-9 Meshing approach for film-cooling

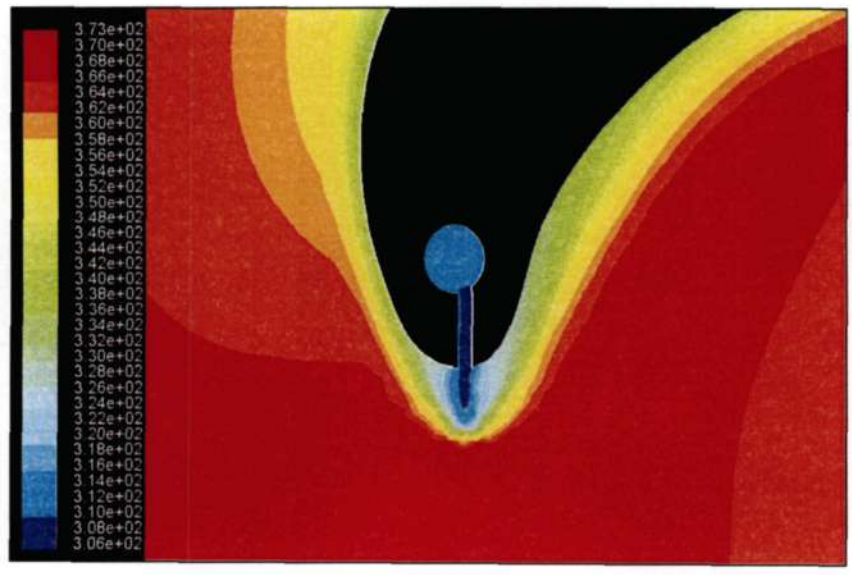

Figure 5-10 Static pressure contours using a single cooling pipe

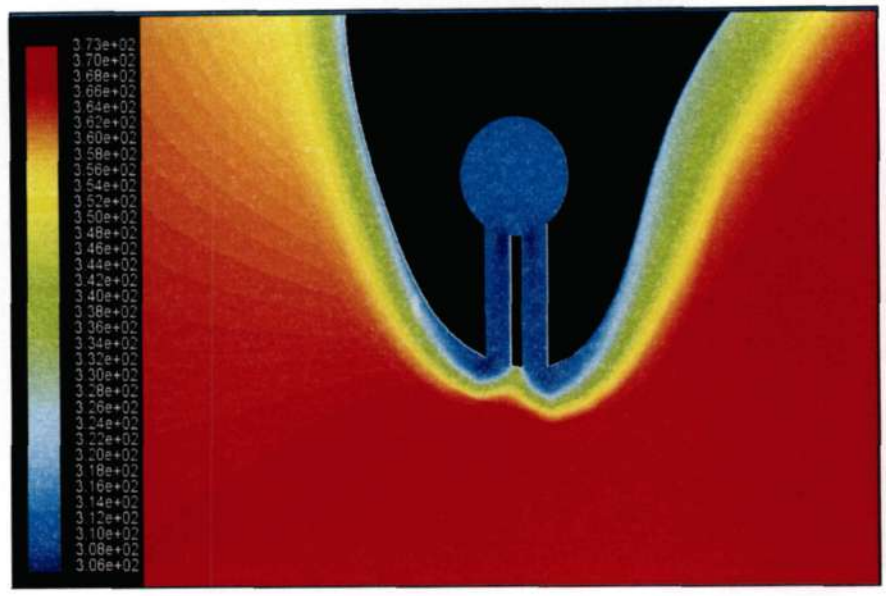

Figure 5-11 Static pressure contours using two cooling pipes

The static pressure contours presented in Figure 5-11 was achieved with great difficulty. Although the distribution depicts uniform cooling on either side, numerous simulations were attempted in order to achieve this effect. Variations in millimetres regarding the location of the cooling pipe resulted in an overcompensation of flow towards a certain side of the blade. The static pressure contours of the double arrangement showed a much better cooling efficiency on both sides of the blade as compared to the single piping. It was therefore decided to progress on this concept to improve on its design.

The two leading edge holes have a significant cooling effect over the entire blade, but the protection prescribed was to maintain the blade temperature below 60°C. When the coolant is ejected at 40 °C it passes over the blade surface and the temperature gradually increases. This is because of the temperature differential and occurs via diffusion with the mainstream flow. It was evident from the static temperature contours shown in Figure 5-12 that another coolant location was necessary. The static temperature contours illustrates that a temperature of below 60 °C is maintained over the entire suction surface. The pressure surface on the other hand illustrated a region where the temperature reached 60 °C. This is given as point c in Figure 5-12. It was then decided that a cooling hole should be placed at, or before, this point.

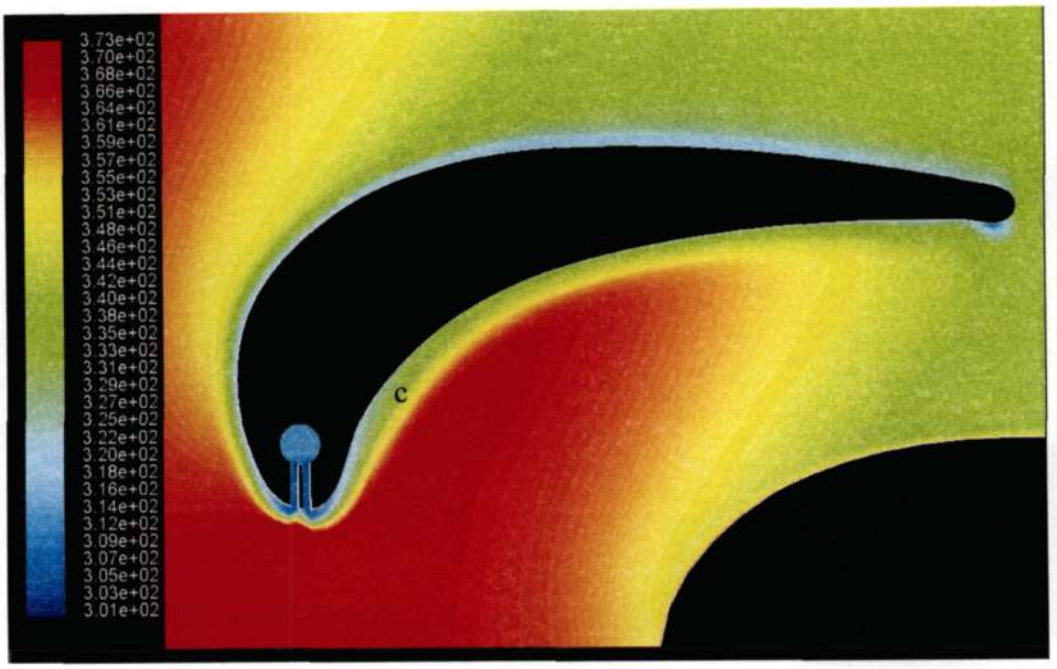

Figure 5-12 Static temperature distribution of the double piping arrangement

The placement of a second hole would require the creation of a second plenum and another pipe projecting out of the surface. The pipe would have to be slightly angled with the direction of the mainstream flow as to prevent excessive spraying. This is illustrated in Figure 5-13, where the cooling hole on the pressure side comes in normal to the blade surface. The implication of this concept is that the momentum carrying the coolant out of the hole may cause the jet to lift off the surface. The coolant will then tend to dissipate into the hot air-stream leaving the pressure surface downstream unprotected. It was for this reason that the idea was rejected.

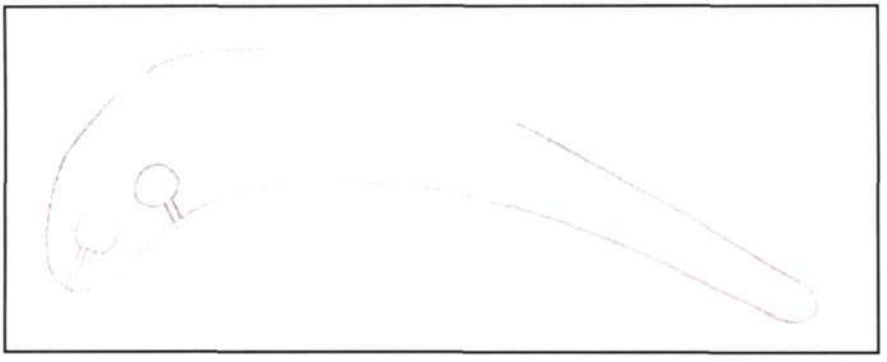

Figure 5-13 Coolant pipe coming in normal to the pressure side of the blade surface

Figure 5-14 below shows the static temperature distribution of the blade with the pressure side cooling pipe entering at an angle. It was clearly evident that the blade static temperatures did not exceed 60 ^{0}C. The velocity and static pressure contours for the proposed cascade with

simultaneous leading edge and suction side film-cooling given in Figures 5-15 and 5-16 respectively, indicated no major separation effects with all parameters lying within acceptable limits. This arrangement was therefore deemed as sufficient for design for the pressure and heat transfer measurement test blades.

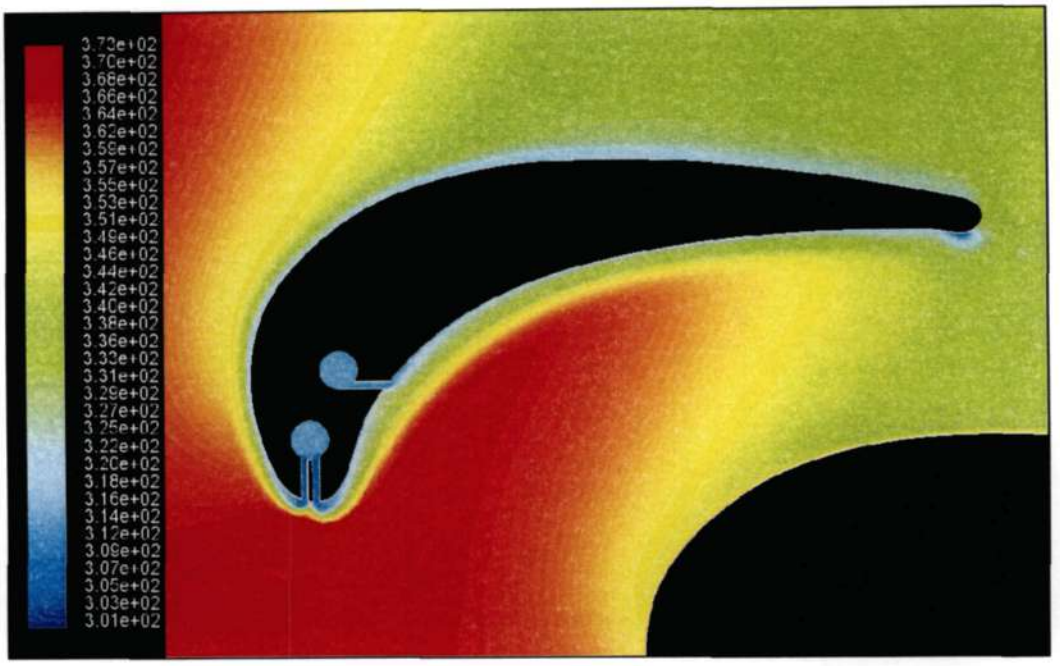

Figure 5-14 Static temperature contours with simultaneous leading edge and pressure side cooling

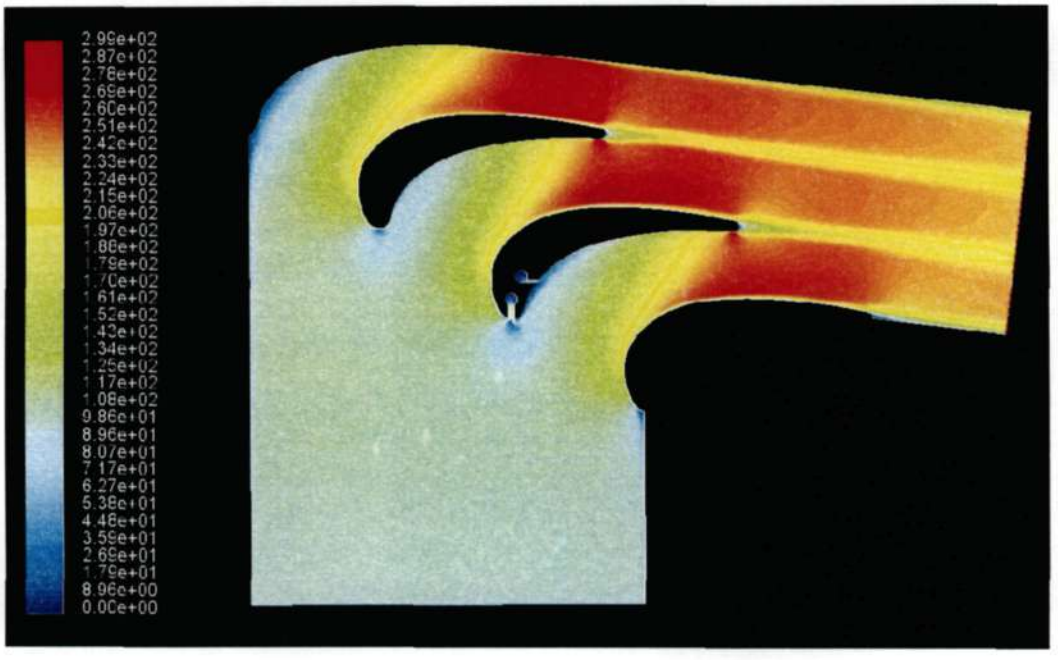

Figure 5-15 Velocity contours with simultaneous leading edge and pressure side cooling

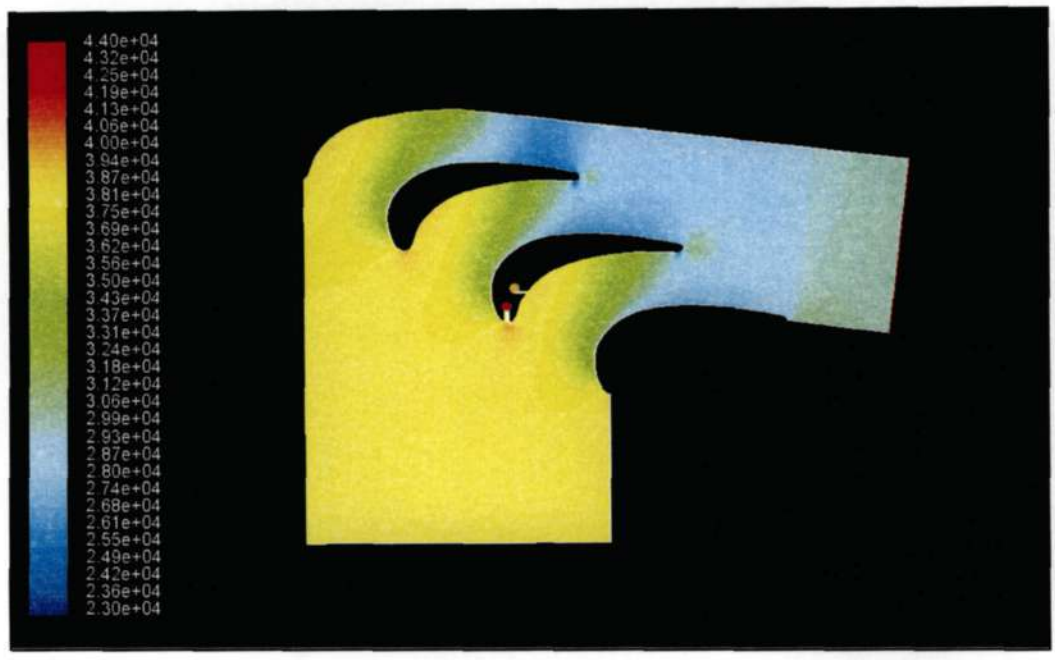

Figure 5-16 Static pressure contours with simultaneous leading edge and pressure side cooling

The design for film-cooling was conducted using a 2-D CFD model. Naturally the flow through the cascade is of a three dimensional nature and secondary effects were neglected in the CFD model. In order to allow for cooling protection in the spanwise direction of the profile, the cooling holes were mirrored in the lateral direction of the blade. The spanwise spacing of the cooling holes was made in accordance to that used by Camci and Arts (1989). The arrangement of the cooling holes at the leading edge was staggered over the 80mm span of the blade. This was intended to provide for more efficient cooling effects. Studies of Han et al. (2000) have indicated that the staggered rows do actually provide better protection than inline rows. The proposed film-cooled blade with staggered row arrangement and pressure side cooling is shown in a 3-D translucent view below in Figure 5-17. The cooling chambers run through the blade in a spanwise direction until 2mm away from the endwall. One end is left open for the supply pressure and the other end is blocked by the blades material. This forces the air through cooling holes and into the mainstream at high velocities. The configurations of the cooling holes are shown in further detail in Figure 5-18.

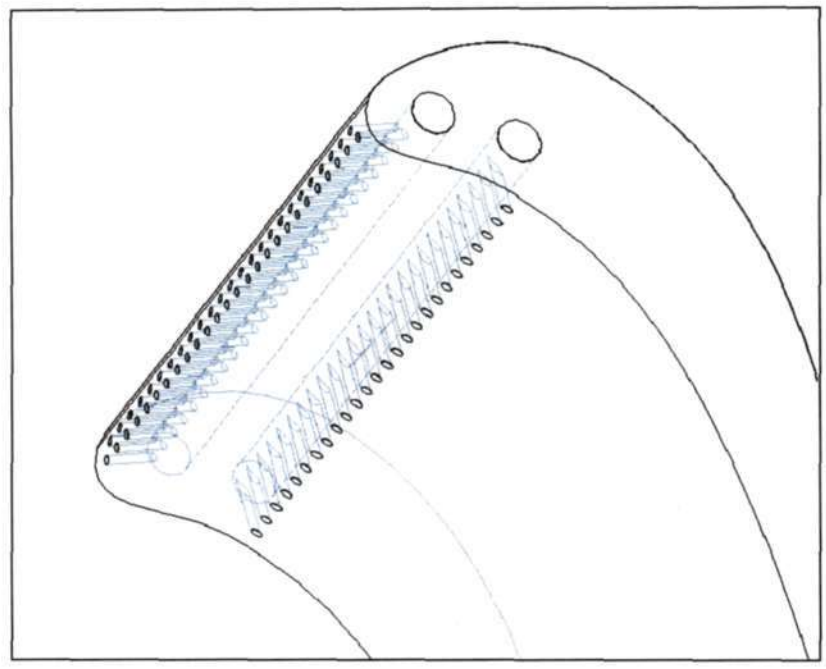

Figure 5-17 3-D Translucent view of the proposed film-cooled test blade

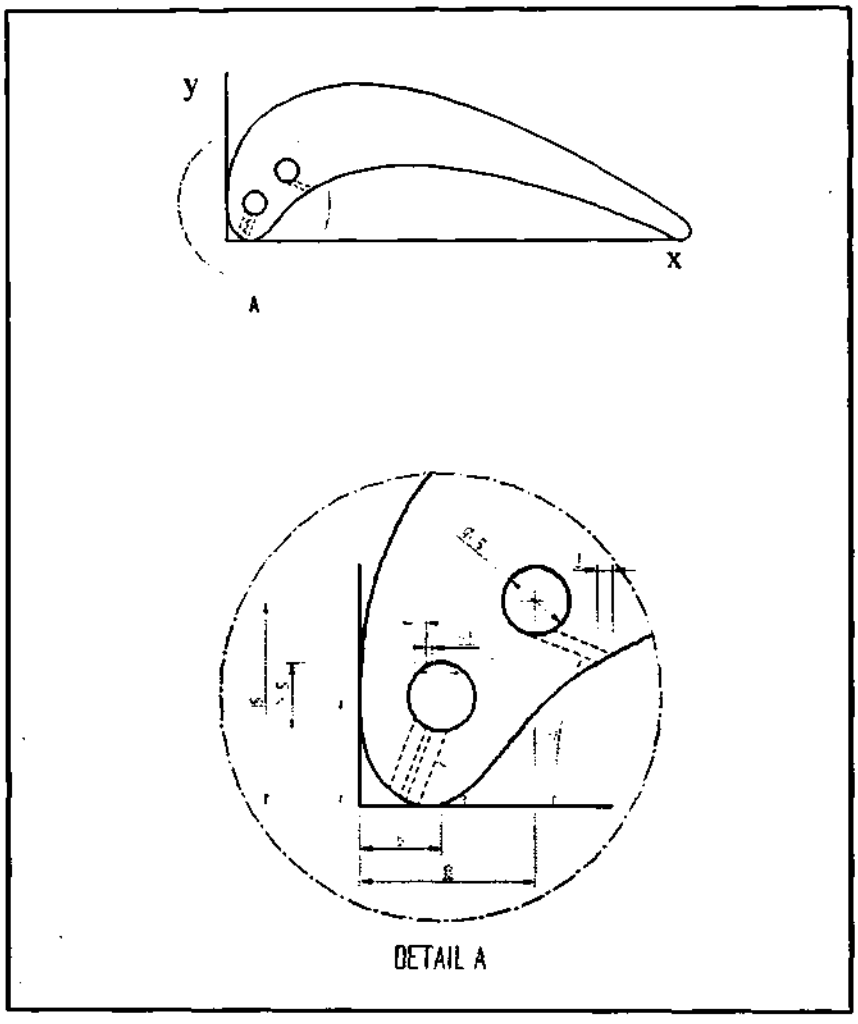

Figure 5-18 Proposed film-cooling blade configurations

5.3.4 Film-Cooled Static Pressure Measurement Test blade

The static pressure measurement test blade would span 90mm and be implemented with 39 0.5mm pressure tapings drilled perpendicularly to the blade surface along its midspan. The pressure surface would have 18 tappings and the suction surface 21 tappings. The static pressure tapping measurement chambers would be offset 2mm from the edge of the blade profile. Because of the tapering nature on the profiles trailing edge, a staggered arrangement of the chambers was implemented. Two 5mm brass tubing, 25mm long, would be fitted to the supply cooling chambers with coolant. The tubings would be instrumented at a depth of 5mm into chambers and serves as an attachment for the coolant supply. Similarly 39, 1mm brass tubing 15mm in length would be fitted into the pressure tapping measurement chambers. Similar provisions were made to accommodate for the temperature and pressure monitoring of each cooling chamber. These provisions are instrumented to the same dimensions as the pressure

tappings but are located on the opposite side of the blade. One of the tappings is used to measure the total pressure within the plenum and the other is instrumented with a thermocouple wire which is sealed to prevent coolant leakages. The 3-D view of the proposed pressure measurement test blade is shown below in Figure 5-19.

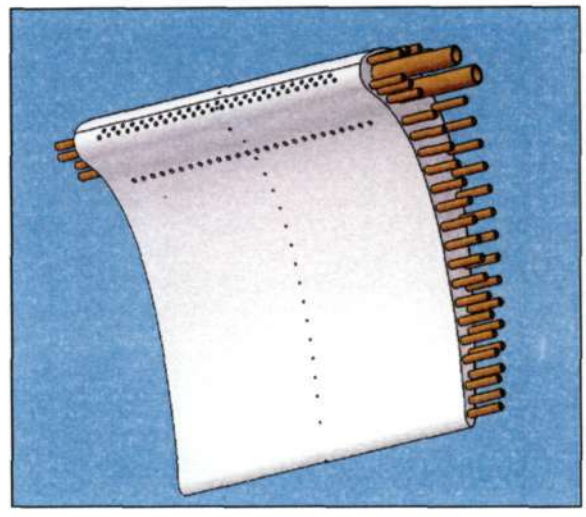

Figure 5-19 3-D view of the proposed film-cooling blade

5.3.5 Film-Cooled Heat Transfer Blade Stack

The film-cooled heat transfer blade stack was designed using the SMR-95 heat transfer test blade as a guideline. This is because the same guillotine technique (see section 4.5.2) was to be used to bring about the transient conditions within the cascade. The featured design would therefore be made of an aluminium dummy blade and an instrumented test section which are held together by two tie rods.

The instrumented segment would consist of Vesconite spacers on either side of a Macor test section. The Macor test section would be instrumented with platinum thin film heat flux gauges and drilled coolant holes in the same configuration as shown in Figure 5-18. Provisions would also be made on the Macor test section to accommodate for the flying lead attachments which are connected to each thin film gauge on either side. These attachments would then be wired to a number of 25 pin D-type connectors which are in turn connected to the heat transfer analogue. An assembled view of the proposed film-cooled heat transfer blade stack is given in Figure 5-20 indicating the various sections.

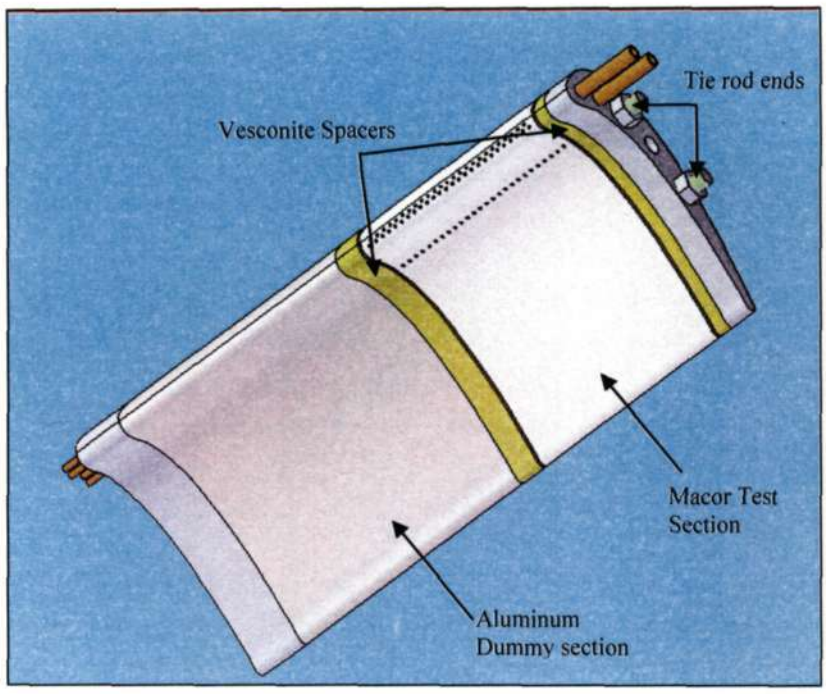

Figure 5-20 3-D view of the proposed film-cooled heat transfer blade stack

5.4 Coolant Supply Line

A fundamental requirement for film-cooling is a supply of coolant to the respective test blades. In doing so, the experimental facility would have to be modified to accommodate for an extra supply line. The most obvious and feasible choice was to use the blower. The blower has been used previously in the heat transfer experiments to pre-chill the instrumented section of the blade stack. This is done so that the required gas to wall temperature ratio can be achieved. A 1.5 kW DC motor is linked to the blower through a flat belt. The blower then sucks air in from the plenum through a shell and tube heat exchanger. The air is then exhausted through another water-cooled shell and tube heat exchanger before it re-enters the plenum at approximately 20 $^{\circ}$ C. Figure 5-21 shows the supply line of the blower just before it enters the plenum.

The idea conceived is to bleed off some cooling air from this line. This means making a junction just before the line splits and supplying the film-cooled blade from this source as shown in Figure 5-22. Monitoring equipment such as a pressure gauge and thermocouple could then be placed at points on the line. A valve would also be placed on the line so that the flow can be turned off when no cooling is needed. The amount of coolant supplied could be controlled via a DC motor speed controller.

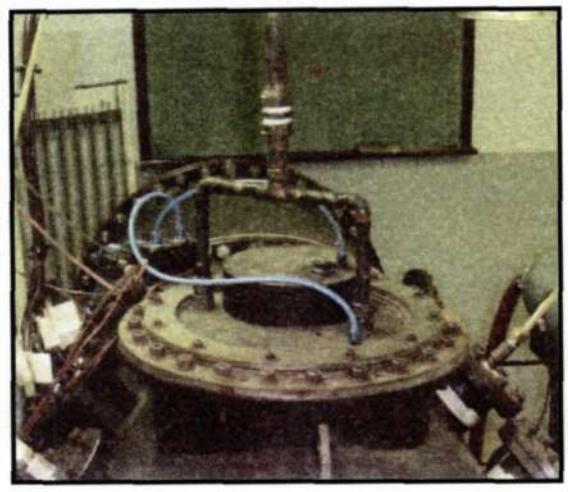

Figure 5-21 Blower supply line to the plenum

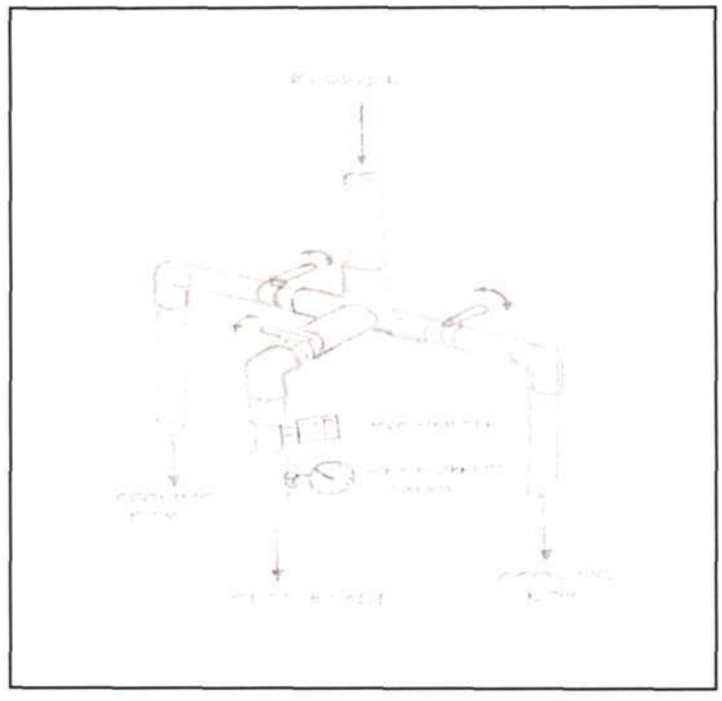

Figure 5-22 Proposed blower supply line

5.5 Conclusions

The study produced a means of implementing film-cooling in the supersonic cascade facility present at UKZN. However, its implementation required that the supersonic cascade facility and its associated data acquisition system be operational. These requirements were not available at the outset of this project. It was therefore concluded that in order to proceed with the project, the operation of the experimental facility and data acquisition system first be verified by

experimental testing. The testing required that a static pressure and heat transfer distribution be acquired around the profile of the SMR-95. This left very little time to proceed with implementing film-cooling technology at UKZN. The project then deviated towards developing the numerical codes used to predict the pressure and heat transfer distributions around gas turbines. The subsequent chapters therefore deal with the experimental methodology and results obtained. These results were then used as validation for a numerical model developed in the CFD package, FLUENT.

CHAPTER 6

EXPERIMENTAL METHODOLOGY AND RESULTS

6.1 Introduction

Experimental results of heat transfer and static pressures over the high turning angle SMR-95 blade profile have been generated using the supersonic cascade facility. The purpose of conducting an experimental investigation was to validate and develop existing numerical modelling techniques. The measurement of turbine blade heat transfer however, is useless as a means of validating numerical predictions without a detailed knowledge of the flow field within the cascade. The investigation was therefore broken down into an aerodynamic characterisation and thermodynamic analysis.

The aerodynamic analysis included a periodicity study of the flow field within the cascade and an evaluation of the static pressures around the blade profile. The static pressure distributions were compared against previous experimental data sets of de Villiers (2002), Stieger (1998) and Snedden (1995) for validity. Once validated, the results were then post processed to obtain an experimental Mach number distribution which is a useful tool for comparison against heat transfer results.

The determination of an experimental heat transfer distribution however, entailed a re-instrumentation of the heat transfer blade stack. This was necessitated due to the limited amount of sensors available as well as the poor sensitivity of the gauges. In an effort to repair damaged sensors and improve on the quality of results, the heat transfer blade stack was successfully re-instrumented with platinum thin film heat flux gauges with increased sensitivity. An isothermal heat transfer co-efficient distribution was then generated using the existing transient measurement technique.

6.2 Aerodynamic Analysis

The process of conducting an aerodynamic analysis was facilitated by the calibration of the respective pressure transducers. Once accurate calibration data was attained, the cascade was checked for periodicity. Experimental static pressure distributions were then generated at the

base test conditions given below in Table 6-1. All subsequent testing of heat transfer had also occurred under these conditions. The test conditions prescribed by Stieger (1998) were used for the investigations because of the vast amount of available experimental data sets. The existing data sets obtained by previous researchers were used a guideline to minimise experimental errors and optimise on the quality of results.

Table 6-1: Base Test Conditions

Total inlet pressure [Pa]	40 000
Compressor motor speed [rpm]	2500
Turbulence intensity [%]	3 %
Reynolds Number	$\pm 2.8 \times 10^5$
Inlet Mach Number	±0.42
Outlet Mach Number	±0.68
$T_{wall}/T_{freestream}$	±0.8

6.2.1 Calibration of Pressure Transducers

The accuracy of experimental pressure results depends largely upon the accuracy of the transducers calibration data. Two types of pressure transducers were used for the aerodynamic investigation i.e. a Rosemount differential pressure transducer and a Kulite ITQ – 1000 pressure transducer of which both are described in section 4.4.3.

The calibration curves for the Rosemount transducers were plotted to calculate the relationship between differential pressure and its output signal voltage. The calibration curves were drawn to show how the output voltage, which is converted by passing a proportional current through a 470 Ω resistor, varied with the measured differential pressure. This was accomplished by connecting the total inlet pressure of the plenum to the LP side of each transducer and leaving the HP side open to atmosphere.

The pressures were monitored using a mercury filled U-tube manometer and the vacuum pump was initiated to lower the pressure within the plenum. The output signal proportional to the differential pressure supplied was captured by Waveview software through channels 0 and 1 on

the PC30 PGL A/D card. The software recorded the changing voltage signal as a function of time while a stopwatch was activated to monitor the changing manometer height with time. The manometer heights are then converted into pressures and plotted against the corresponding voltage readings to determine the calibration constants. A typical calibration curve of the Rosemount transducers is given below in Figure 6-1.

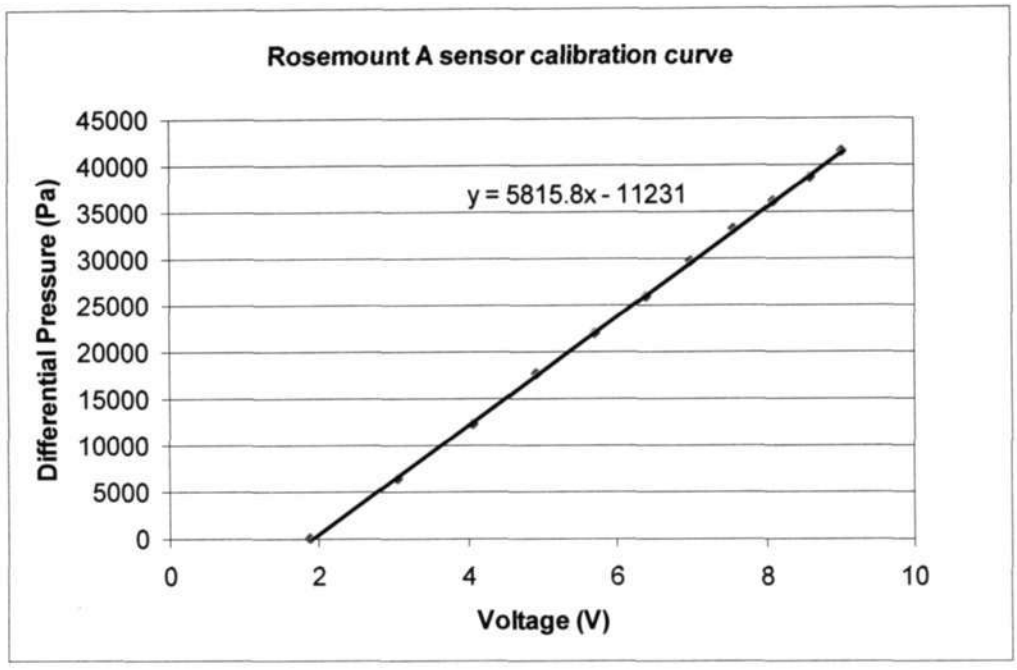

Figure 6-1 Typical Rosemount pressure transducer calibration curve

The calibration procedure for the Kulite pressure transducers were done in a similar manner as the Rosemount pressure transducers. The only difference is that the Kulite transducer measures the total pressures, so the calibration plot can be directly drawn by plotting the total pressure directly against the voltage output. The Kulite transducer has an output range of 0-100 mV and the signal was sampled through channel 3 of the PC30 PGL A/D card. A detailed description of all the calibration procedures can be found in Appendix B with the pressure calibration curves in Figures B-1 and B-2. The calibration constants used for the periodicity and static pressure measurement experiments are given below in Table 6-2.

Table 6-2: Final Calibration constants for pressure transducers (See Appendix B1.1 for graphs)

Rosemount A (Suction Side)		**Rosemount B (Pressure Side)**		**Kulite (Total Inlet)**	
dP/dV_1 (Pa/V)	P_{01} (Pa)	dP/dV_1 (Pa/V)	P_{01} (Pa)	dP/dV_1 (Pa/V)	P_{01} (Pa)
5815.8	-11231	5438	-10338	1066899.7	-2903.7

6.2.2 Periodicity Study

The periodicity and repetitivity of the cascade was evaluated by measuring the outlet static pressure distributions in the pitchwise traverse direction. The experiment was setup with the static pressure measurement test blade bolted to the cascade. Silicon tubing was attached from the exit static pressure tappings to the scanivalve and the pressure measurement data acquisition system (described in section 4.4.4) was used to acquire the experimental data. The locations of the exit periodicity tappings are shown below in Figure 6-2.

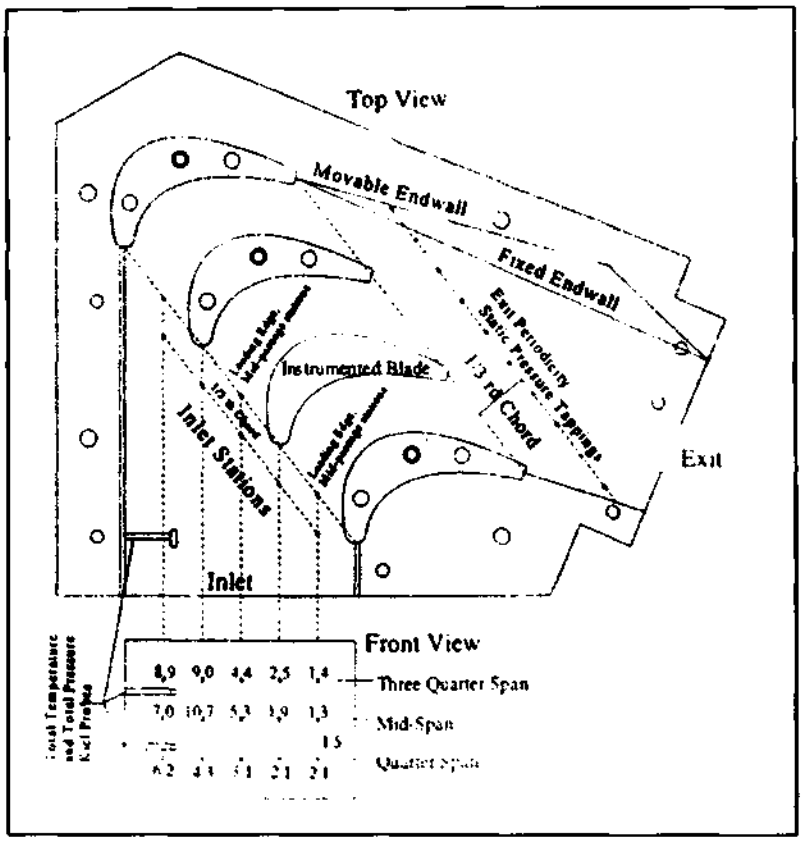

Figure 6-2 Cascade measurement stations (reproduced from Snedden (1998))

The periodicity measurements were conducted at base test conditions with a fixed endwall and the results are presented below in Figure 6-3. The static pressure measurements across the exit plane illustrated poor periodicity of the cascade, with a variation of approximately 500 Pa. Snedden (1998) conducted a similar aerodynamic characterisation of the same cascade. The outcome of his investigation further validated the current measurements and noted that the usage of a two-piece side-wall resulted in poor cascade periodicity.

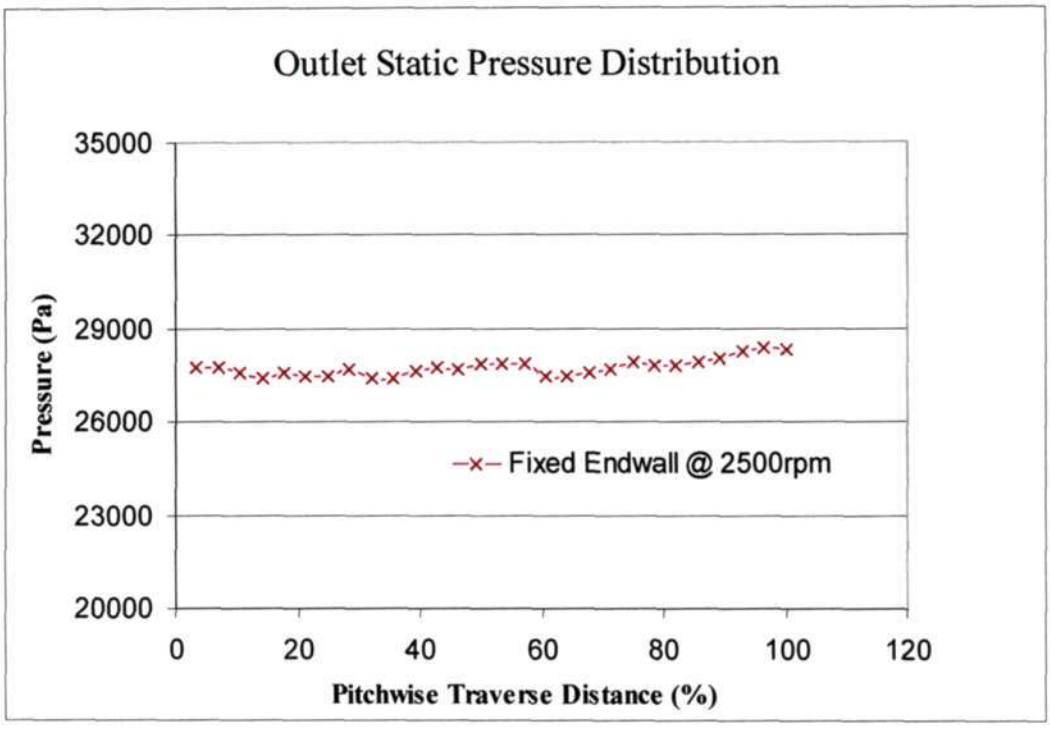

Figure 6-3 Cascade outlet static pressure distribution with a fixed endwall

6.2.3 Experimental Static Pressure Distributions

The experimental predictions of static pressures over scaled turbine airfoils are an extremely useful tool when predicting the corresponding heat transfer distributions. In general, accelerating flows are usually associated with thin boundary layer formations and consequently high levels of heat transfer.

The experiment was set up using the equipment described in section 4.4 and the rig was started up following the procedure outlined in Appendix C1.1. The process of acquiring the actual static pressure measurements are given in Appendix C1.2. In order to acquire reliable data measurements it is vital that the silicon tubings be fastened away from the inlet bellmouth and are checked for any cracks or slits. The data was sampled at base test conditions with a total cascade inlet pressure remaining constant at 0.4 kPa. This was monitored by connecting the cascades total inlet pressure Kiel probe to the Kulite pressure transducer on the display box. The pressure was then maintained using the vacuum pump control circuitry described in section 4.2.2. This is accomplished by manually setting the maximum desired plenum gauge pressure, which is read on the yoke box according to the cascade's total inlet pressure read on the display box. The only two variables which then have to be constantly monitored through out the

experiment are the compressor speed and cascade total temperature. The compressor speed is controlled via a toggle switch located on the display box and the cascade temperature was varied by regulating the amount of water supplied to the radiator.

The initial pressure measurements were conducted using only one Rosemount pressure transducer. This was because of the inability to achieve accurate calibration data on Rosemount A. The outcome of the experimental procedure therefore required that two sets of sampling be done. This deficiency in the measurement system further added towards experimental error as great difficulty was encountered when controlling the compressor speed. The initial test results are presented below in Figure 6-4, and are compared against the data sets of Snedden (1995) and de Villiers (2002).

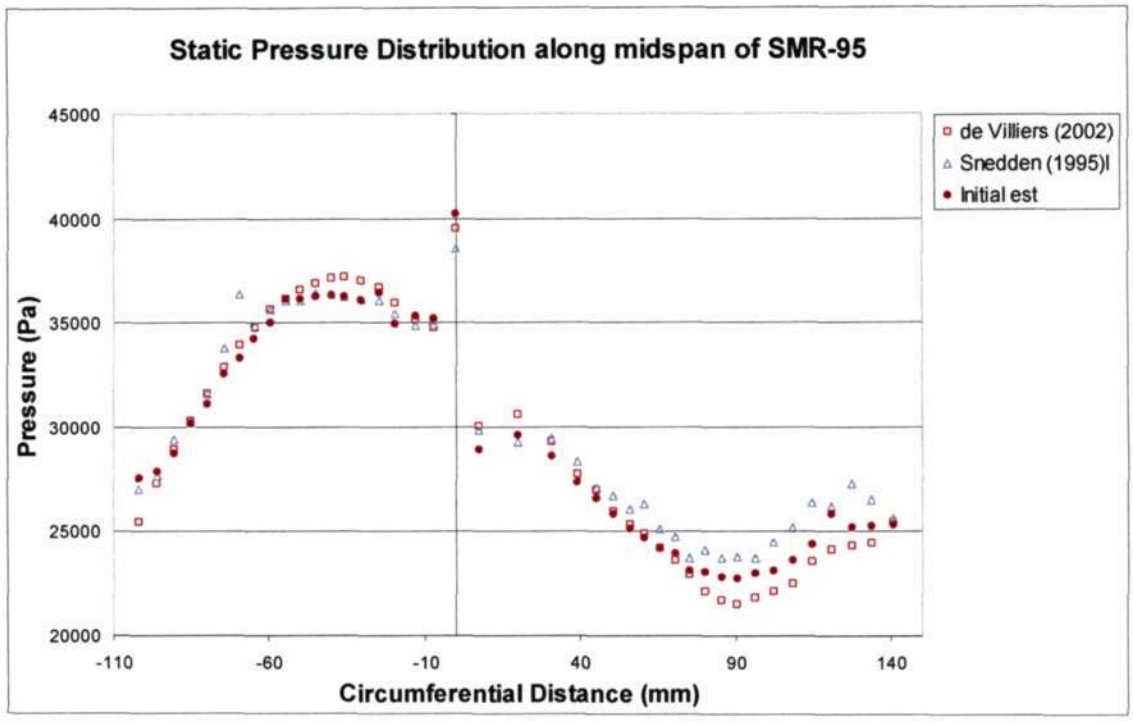

Figure 6-4 Static pressure measurement test 1 compared to previous researchers

The outcome of the experimental validation on the pressure side revealed an increasing trend of static pressures from the trailing edge (TE) to about 50mm circumferential distance (CD). This trend was common to both sets of previously recorded data however, from 50mm (CD) up unto leading edge (LE) the results tend to follow the pattern of Snedden (1995). The results on the suction side had the tendency to maintain the flow pattern of Snedden (1995) from the LE right up to 65mm CD. From 65mm CD till the TE, a deviation of approximately 300 Pa split the initial test results from the results of previous researchers. Although the general flow pattern

was confirmed, more testing was in order to improve on the quality of the test data by repairing and re-calibrating the faulty pressure transducer.

The faulty pressure transducer was sent to specialists and the calibration ranges adjusted and set. The second test produced albeit more conclusive results and these are presented below in Figure 6-5. The use of two transducers reduced the sampling time in half and brought about more confidence with regard to experimental errors.

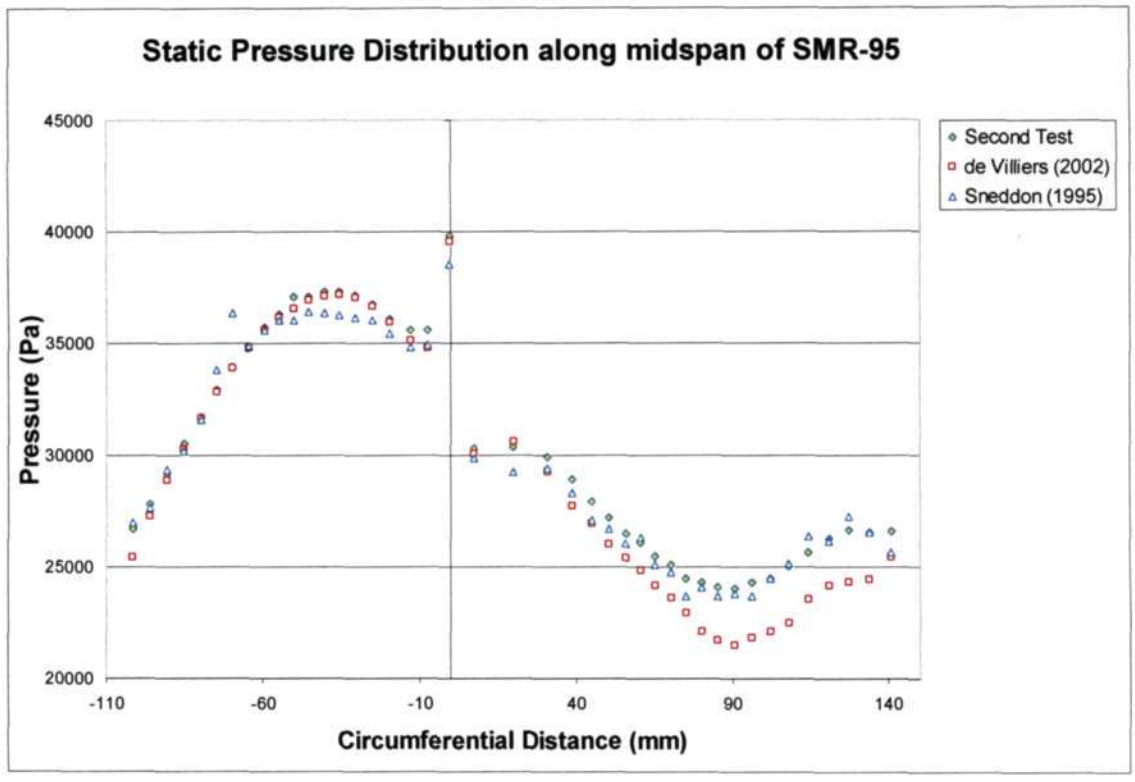

Figure 6-5 Static pressure measurement test 2 compared to previous researchers

The results from the TE till LE on the pressure surface clearly showed a distinct comparison to the results of de Villiers (2002). The results from the LE to the TE on the suction side however, resembled a pattern more closely followed by Snedden (1995). This divergence in experimental results amongst researchers was further investigated by analysing the raw data files of de Villiers. The outcome of which indicated that de Villiers used a single pressure transducer for his measurements and noted a higher compressor rpm when sampling measurements on the suction side. The hydraulic motor speed was approximately 100 rpm higher than the base test conditions. This speed is stepped up 6 times by the gearbox and the result is elevated inlet Mach numbers with greater differential pressures. It was therefore concluded that the results of de Villiers was slightly under predicted on the suction side and a repeatability test was to be

conducted to further validate the current pressure distribution. The results of repeatability are presented below in Figure 6-6.

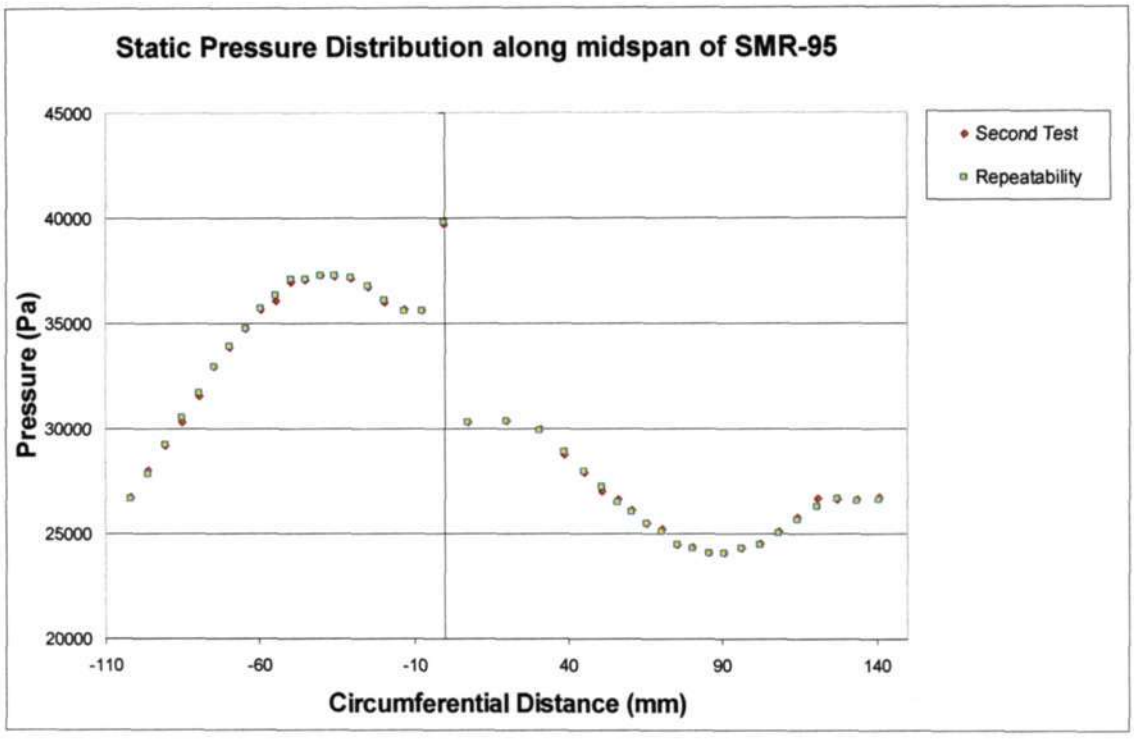

Figure 6-6 Repeatability test

The correlation between repeatability and the second test were excellent, with no significant deviations in results. This had concluded the static pressure experimentation over the profile and an analysis into the results was the next step. The static pressure measurements were then converted in an experimental Mach number plot using the general high speed flow equations. The experimental Mach numbers were plotted against percentage chord (%) and are given in Figure 6-7. The graphs of static pressures and Mach numbers were then used to assist in the flow characterisation and analysis.

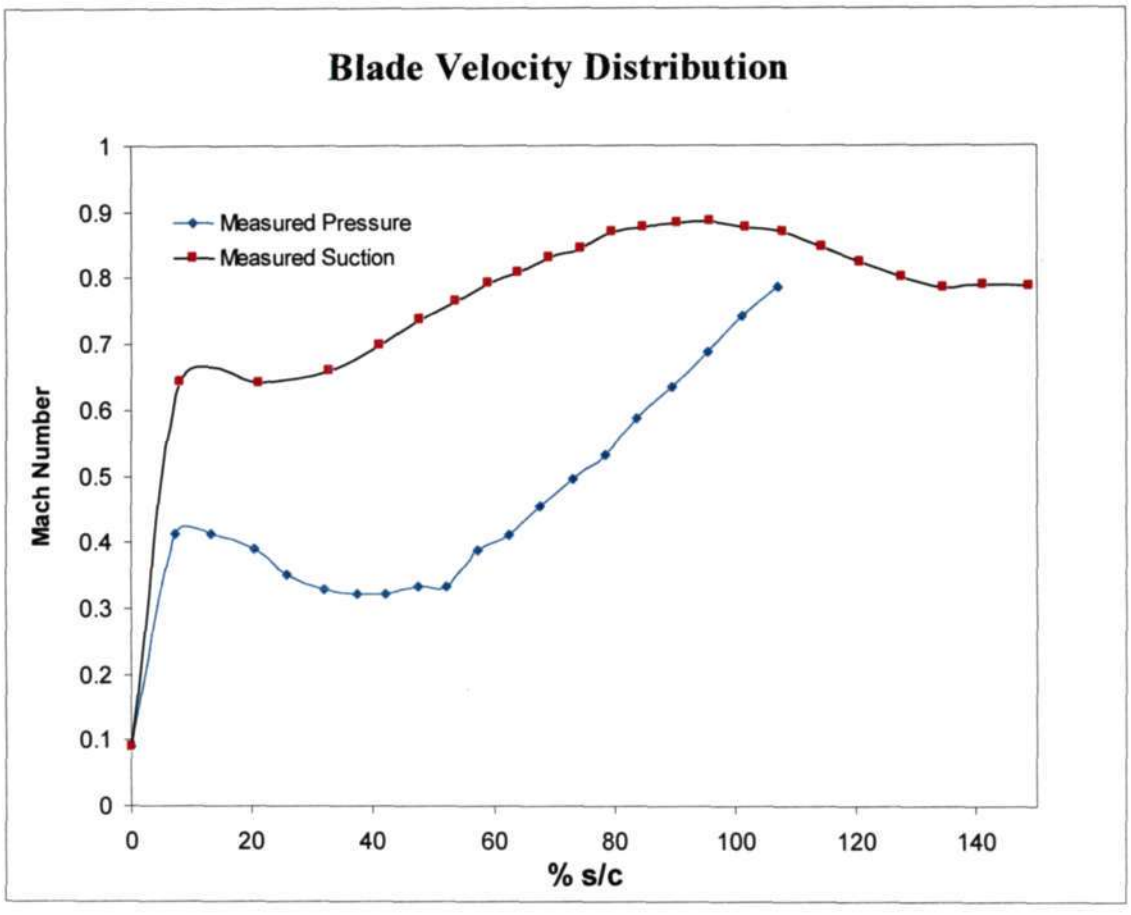

Figure 6-7 Experimental Mach number plot for the SMR-95

6.2.4 Flow Characterisation and Analysis

The analyses of the experimental static pressure distributions indicate a highest pressure in the region of 40 kPa to be at the leading edge of the blade profile. This is expected as the flow impinges at right angles to the blade surface creating a stagnation point therefore causing the kinematic component of pressure to tend to zero. The result would therefore be validated by the total inlet pressure within the cascade which was measured and regulated by the Kiel probe.

The experimental Mach number distribution in Figure 6-7, demonstrates the rapidly accelerating flow conditions to about 7 % chord on both the pressure and suction surface. This is brought about by the sudden change in curvature on the high turning angle SMR-95 rotor blade design. The step change is so sudden that the flow develops a leading edge separation bubble. This was noted by the visualisation experiments conducted by Stieger (1998). An illustration of his experiment taken at the same base test conditions of this dissertation is given in Figure 6-8.

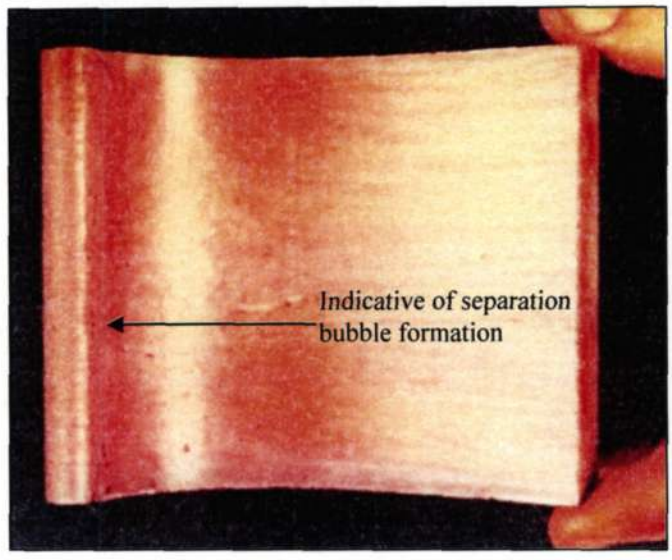

Figure 6-8 Flow visualisation experiment seen on the pressure at base test conditions (reproduced from Stieger (1998))

The separation bubble is followed by turbulent reattachment of the flow which then accelerates into transonic conditions at the throat section of the blades passage. The throat section which is at about 90 mm CD suction surface is indicative by the change in velocity gradient. Here, the flow attains transonic conditions and results in the formation of a shock wave which causes the change in velocities. It should be noted that the pressure result at the TE is an average of two tappings and its slight decrease in pressure could be attributed to this experimental error.

Although these measurements are of a low resolution and predicting the complex flow patterns would be difficult, the sole purpose of conducting the experiments is to validate numerical predictions. Once a proper validation has been attained, CFD analysis would be able to provide much higher resolutions of data as well as expanding the results into flow visualisations for better understanding and assessment.

6.3 Thermodynamic Analysis

The thermodynamic analysis entailed generating isothermal heat transfer coefficients over the SMR-95 blade profile. As discussed in preceding sections, the heat flux data is generated using thin film heat flux gauges and an electrical analogy. This instrumentation, which had been designed and constructed by Snedden (1995), was over a decade old and had numerous amounts of broken sensors and faulty cards. Although the setup had also been used by Stieger (1998) and

de Villiers (2002) to generate heat transfer data, based on its current state at the beginning of the project, the probability of producing quality heat flux data seemed dismal.

Nevertheless, testing using the setup was conducted and the results were not far from the expected predictions. The outcome of the initial testing revealed highly noisy signals and inadequate gauge sensitivity to produce a decent set of heat transfer results. It was therefore recommended that the blade stack be re-instrumented with gauges of higher sensitivity and the heat transfer analogy be repaired. This procedure required acquiring the relevant paint for the heat flux gauges, which was generously supplied by the CSIR ballast group and following the procedures outlined by Ligrani et al (1982) and Snedden (1995) into its application. The electrical analogy had to be dismantled and each individual component checked for faults. The result of the fault finding revealed broken op-amps which were replaced.

6.3.1 Thin Film Gauge Construction

The construction of the new platinum thin film heat flux gauges meant dismantling the entire blade stack and removing the Macor test section. Macor is used as the substrate because of its highly attractive properties for the intended application. It has a low thermal conductivity and good insulation properties which ensures the validity of the semi-infinite slab assumption. It is easily machinable and has the ability to be heated up to temperatures of 1000 °C without any significant geometric deformation. The section was prepared by removing the existing gauges and polishing to a high quality finish. The heat flux gauges are then painted and fired onto the surface. Electrical connections complete the construction and the blade stack is reassembled. These processes are described in more detail below.

6.3.1.1 Substrate Surface Preparation

In order to apply the gauge material, the substrate must be extremely smooth and highly polished. The resulting film should be only microns thick and sharp irregularities on the surface have to be removed. Any form of cracks or non uniformities on the substrate surface could lead to poor gauge quality and have detrimental effects on results.

The existing gauges were removed by hand using #800 grade silicon carbide water paper. To obtain a smooth, polished surface, the removal was continued using #1000 and then #1200 grain

sandpapers. The period of polishing the surface was approximately 10 minutes per grade of sandpaper used. The edges of the blade were then slightly chamfered using #1200 grade water paper. The rounding of the edges is required to avoid wrapping the lead connections around sharp corners, which would result in poor electrical contact.

Ligrani et al (1982) recommended completing the polishing process using cerium oxide powder. Snedden (1995) used this technique, however due to the high toxicity levels of the substance, it was not available. Cerium oxide was therefore replaced with OPS suspended silica solution which was readily available from any metallurgical company. The solution was applied to the substrate by hand using a crocus cloth, after which the surface was washed with water and dried in an industrial convection oven. The substrate was then further investigated under a microscope for fine cracks and cavities until it was of sufficient quality to apply to the gauges.

6.3.1.2 Gauge Application

After the substrate surface had been adequately polished, the platinum film was applied. Platinum films were formed on the insulating substrates by using commercially available preparations of metallo-organics, such as that specified by Ligrani et al (1982). The "Liquid Bright Platinum 05-X" from Engelhard Industries supplied by the CSIR is solutions of metal compounds in organic solvents. The liquid contains fine metallic particles in suspension and chemical agents that attack the surface of the substrate to provide a highly adherent film.

Before application to the substrate, the Liquid Bright Platinum solution was mixed with 730 thinning essence, also from Engelhard Industries. Several factors were considered when preparing the solution, including purity, concentration and film thickness. The materials were mixed in a clean environment since any impurities would result in faulty gauges. The relative concentration of the platinum and thinner is also important because the final resistance of the gauge depends strongly on the amount of platinum deposited on the surface. Furthermore, poor adhesion may arise from too thick an application of liquid hence, the liquid should be thin enough for application marks to flow out and take on lustre. In the present investigation it was found that in accordance to Ligrani et al (1982), a mixture of 50% paint and thinner produced the best films.

The preferred method for applying the platinum films to the substrate surface consisted of painting a strip of platinum about 1mm wide on the surface of the substrate. In order to ensure

uniform film thickness, a single stroke using a 0.3mm calligraphy pen was used. Although regulating the amount of platinum applied to the surface is difficult, this method ensures the validity of the one-dimensional analysis assumption. Typically, thicker gauges are accompanied by lower resistance values. The positioning of the gauges was placed in accordance to the existing lead connection holes using a paper template maintaining the existing circumferential positioning.

Immediately after application of the platinum, the gauges were dried under high powered lamps. The total drying time under the lamps ranged from 30 – 40 minutes. Drying was performed in a clean environment to avoid the collection of dust or other impurities on the gauge surface. In order for the liquid platinum to form on the surface of the substrate, the piece must be baked at very high temperatures to remove the carriers. The substrate was therefore suspended using ceramic blocks and placed in an electric furnace. The temperature of the furnace was then gradually increased to 350 °C with the door remaining open and held at this temperature for 30 minutes. This draws all the solvents from the paint, which is removed by the ventilation so that it can not interfere with the sintering process. The door of the furnace is then closed and the temperature increased to 700 °C. The electric furnace at UKZN usually takes about 45 minutes to reach this temperature after which it is held constant for 30 minutes to sinter the metal particles together. During the firing process, it is necessary that the rate of increase be gradual so that blistering or boiling of the film does not occur.

Once the gauges have been fired, the furnace is then switched off leaving the blade housed within to cool overnight. This annealing process is done to avoid the development of cracks which would have caused the film's resistance to increase with time due to the stress relief. Two layers of platinum were applied to attain the required resistance levels, of which each layer took a day to paint, fire and cool. After each application, the blade was removed and the resistances were checked. Once resistances in the range of 50-145Ω were achieved, the blade was annealed at 180 °C for three days, monitoring the resistances every day for any variations. The annealing process ensures that the temperature resistance changes remains constant during calibration and testing.

6.3.1.3 Lead and Electrical Connections

The thin film leads to the platinum film were made using the metallo-organic solution "Liquid Bright Gold NW" from Engelhard Industries also supplied by the CSIR. Gold is a convenient

material for thin film platinum gauges because the same baking temperatures and procedure may be used as for platinum. The gold leads were applied using the same thinning essence and concentration as the platinum gauges. The connections may be used to shorten the effective length of the platinum gauges thus lowering the resistances further to obtain the desired value of approximately 50 Ω. The gold is therefore always applied after the platinum gauges.

As indicated earlier, after application of each layer the same baking procedure is followed as the platinum gauges. Only one layer is required, but poor electrical contact around some edges usually results in a second application. The gold leads were made using a single stroke of a very fine paint brush and a template made from masking tape which prevents parallel connections of gauges.

The final step in the gauge construction is making electrical connections to the gold leads. The flying lead attachments utilizsd by Snedden (1995), were repaired using solder and completed the gauges instrumentation. The resistance were checked and a final application of suspended silica with a cotton swab was used to bring the resistances down to the required range. Figure 6-9 below shows the completed Macor test section. The blade stack was then reassembled and ready for calibration.

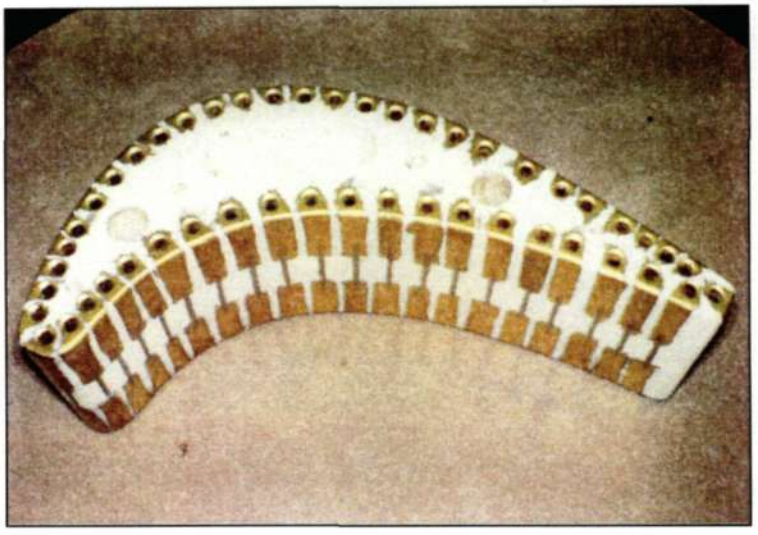

Figure 6-9 Completed Macor test section

6.3.2 Thin Film Gauge Calibration

Before any experimentation could commence, all the thin film gauges had to be calibrated to determine their resistance-to-temperature relationship. As discussed in Chapter 3 of this dissertation, the required data for the calculation of the isothermal heat transfer coefficients is to obtain the parameter constants α_R and R_0. These correspond to the film temperature coefficient of resistance and resistance at 0 °C respectively, which are entered into the LABview program "Isotemp".

The calculation of α_R requires the measurement of the resistance against changing wall temperatures. These values are plotted against each other and the gradient, $\Delta R/\Delta T$ which is the change in resistance over change in temperature, is extrapolated. The y-intercept is also calculated and this corresponds to the resistance when the blade wall temperature is 0 °C. The gradient and the y-intercept are then used to calculate the resistances for which the blade surface is at 40 °C, i.e. the plunging temperature. The sensor calibration constants α_R are determined by dividing the gradient by the resistance at 40 °C. The theory is given in Ligrani et al. (1982) as well as Chapter 3 of this dissertation.

The blade was calibrated by assembling the entire blade stack inside an industrial convection oven and heating it to five different temperatures. The heat transfer analogue and selector box was also used to make acquiring the resistances at the different temperatures easier and faster. This setup also accommodates for the internal resistances of the electrical analogue and selector box as it calibrates the entire system, minimising errors. The resistances were measured with an LG digital multimeter with an accuracy of ±0.001 Ω and the temperatures were measured using the oven display and Fluke 52 K/J thermometers. The calibration procedure for the gauges and results are given in Appendix B 2.1.

Snedden (1995) highlighted the need for increased gauge sensitivity and higher gains on the heat transfer analogue. This re-instrumentation of the blade stack was to achieve exactly that. Initial heat transfer testing of the blade stack used by Snedden (1995) saw calibration data being reproduced for experimental testing. Although the heat transfer results were not of sufficient quality, the calibration data of those gauges were to be used as a comparison for sensitivity of the new gauges. Typical calibration curves for the old and new gauges are given in Figures 6-10 and 6-11 respectively.

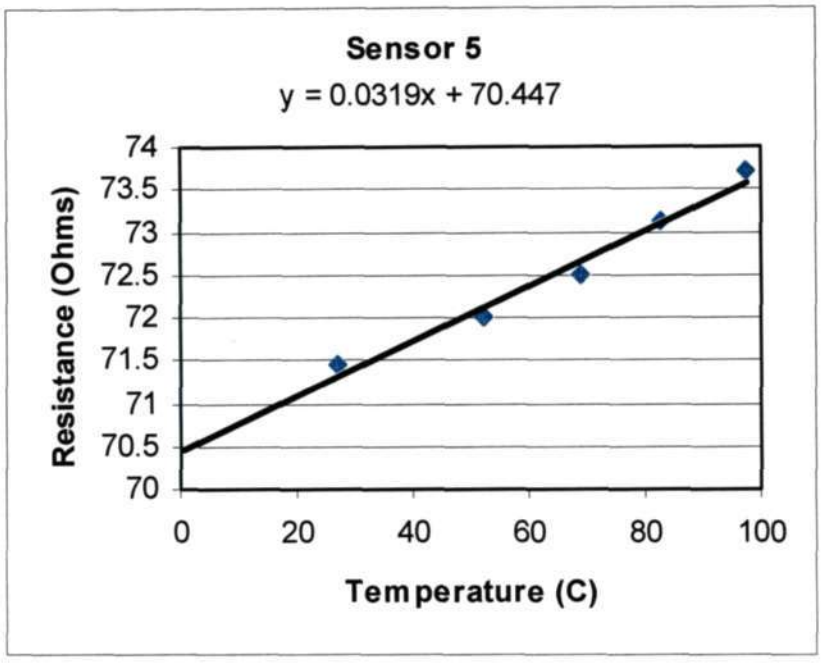

Figure 6-10 Typical calibration plot of old gauges

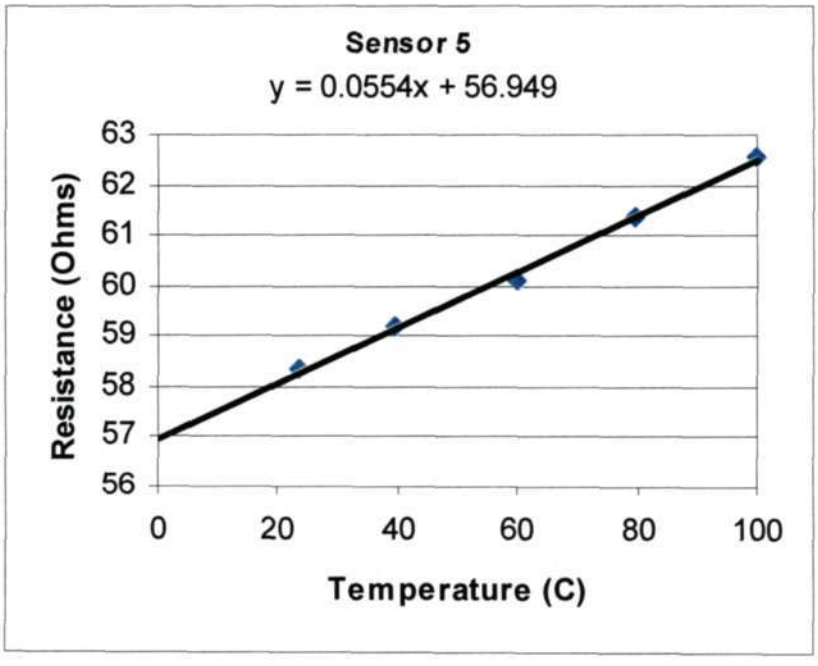

Figure 6-11 Typical calibration plot of new gauges

Although the linearity of the new gauges was more consistent when compared to the old gauges, the sensitivity increase of gauges was marginal. This distressing fact could only be verified by experimental testing.

6.3.3 Circuit Calibration

The calibration of the electrical analogue is achieved by generating and supplying each individual heat transfer card with a parabolic input. The voltage step output from each card is then measured corresponding to its parabolic input to determine the calibration constant which is entered into the LABview program "Isotemp".

The parabola is generated using the program "CAL30", which was written by Snedden (1995). The program also outputs the step output data which is used to determine the respective parameter constant. It is essential that the current source be excluded from the calibration process. This is done by not connecting the heat transfer blade stack to the analogy, thus having an open circuit deeming the current source redundant.

The calibration process requires that an extremely small amplitude parabola be generated and supplied to each individual card. Being that it is difficult to generate such a parabola, Snedden (1995) constructed a prototype circuit that reduced a large parabola some 22 times and supplied it to the respective heat transfer cards. The supply to the respective cards is controlled by a switch which is mounted to the electrical analogy housing. More details can be found in section 4.12 and Appendix 5 of Snedden (1995). The results and procedure for the calibration process can be found in Appendix B 2.2 of this dissertation. Figure 6-12 shows the generated calibration parabola and Figure 6-13 shows a typical step output response. It should be noted that the step outputs were very noisy resulting in numerous calibration data sets to be generated and its averages taken.

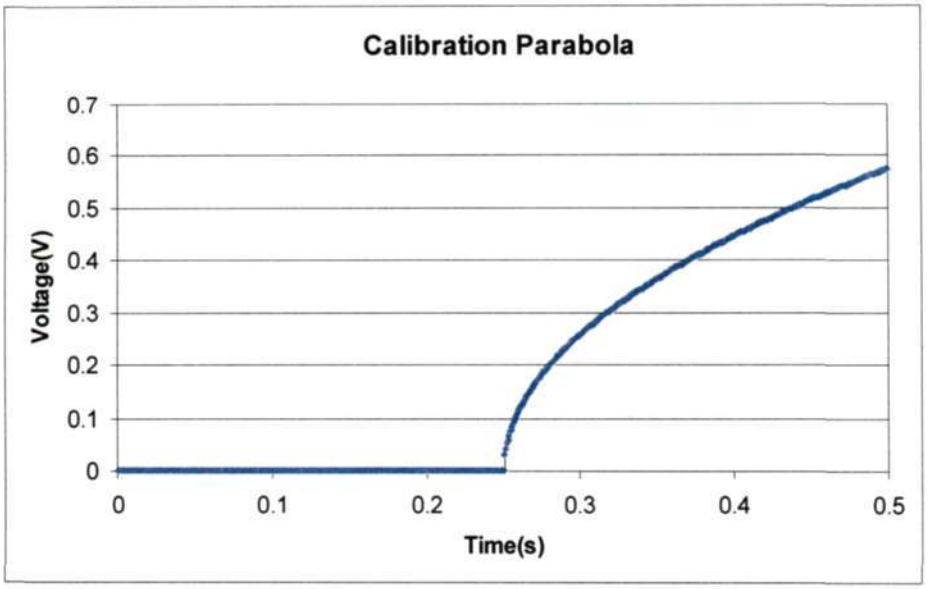

Figure 6-12 Generated calibration parabola

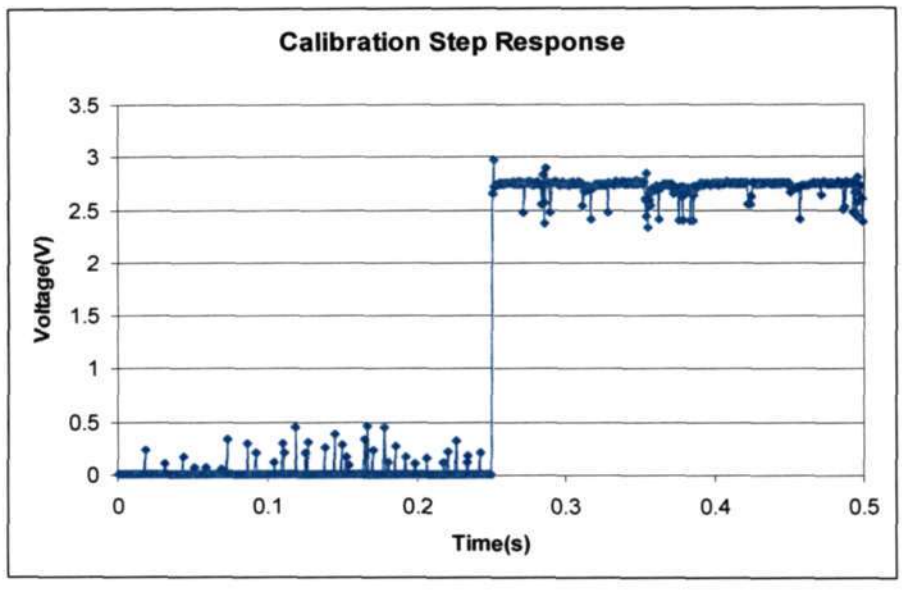

Figure 6-13 Typical circuit step response

6.3.4 Experimental Heat Transfer Results

The determination of the isothermal heat transfer coefficients is accomplished by following the procedure outlined in Appendix C1.3. The most important requirements of the test are that repeatable flow conditions exist between data sampling and that a stipulated temperature differential exist between the cooling box and cascade flow.

Because data sampling occurs sequentially for six different groups of sensors, the test flow parameters such as total temperature, pressure and compressor speed must be kept constant for each test. Although the total pressure is controlled remotely, the plenum temperature and compressor rpm have to be continuously manually adjusted. Fluctuations in any of the test parameters will result in experimental error as a result of the different flow conditions. The author experienced great difficulty in attaining repeatable flow conditions and slight deviations in experimental results could be owed to this deficiency in experimental procedure.

The required temperature differential is accomplished by keeping the cooling box as cold as possible. This is made possible by keeping the water flow to its cooling circuit fully open throughout the protracted duration of the test. To prevent heat loss when running at base test conditions, insulation material is packed within the cooling box so as to minimise the heat transfer to its hot surroundings. The plunging temperature of the instrumented test section is determined by monitoring the resistances on the blade sensors corresponding to 40 °C as well as

checking the temperatures of the four internal thermocouples. Once the instrumented section of the blade was sufficiently chilled to begin testing, the cascade flow temperature was rapidly increased by cutting off the water supply to the internal radiator and increasing the compressor rpm to it maximum.

At sufficiently high cascade temperatures, in the range of 110 °C, the relevant test parameters were adjusted as fast as possible to attain base test conditions. The water supply to the cooling box was then shut off to prevent air leakages into the cascade and the Macor test section was plunged by actuating the solenoid pneumatic ram. Immediately upon actuation, the data acquisition system was started to capture 3 seconds worth of data at 4000 Hz. The data was then saved as a text file and imported into the LABview program "Isotemp" to obtain the isothermal heat transfer coefficients. The initial voltages, sensor resistances and static pressures were also recorded before plunging as these are required inputs for the heat transfer coefficient evaluation and CFD analysis.

As mentioned earlier, the blade stack developed by Snedden (1995) had numerous sensors which were not operational. Furthermore, the sampled step outputs were extremely noisy and of inadequate sensitivity to generate any means of reliable heat transfer data. Nevertheless, experimentation did continue to evaluate its status by a comparison to previously documented results. The initial isothermal heat transfer coefficient distribution generated is given below in Figure 6-14.

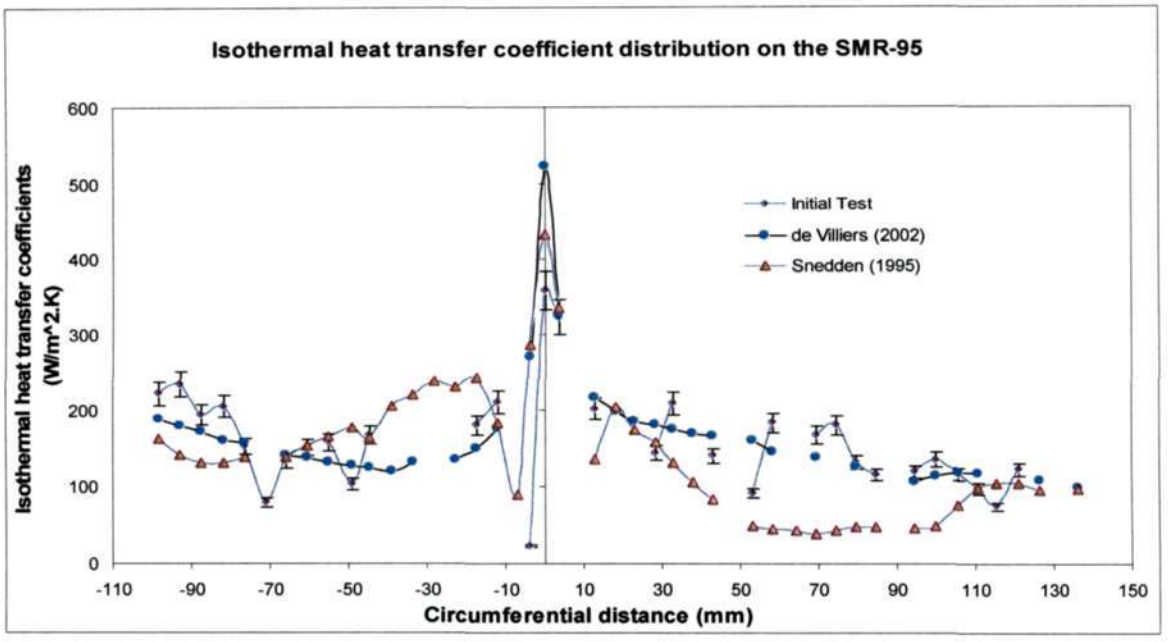

Figure 6-14 Initial isothermal heat transfer coefficient distribution

The highly irregular distribution depicted above and absence of critical sensors further necessitated the need for the re-instrumentation of the heat transfer blade stack. New platinum gauges of higher sensitivity were therefore painted on the Macor substrate and the results are presented in Figure 6-15.

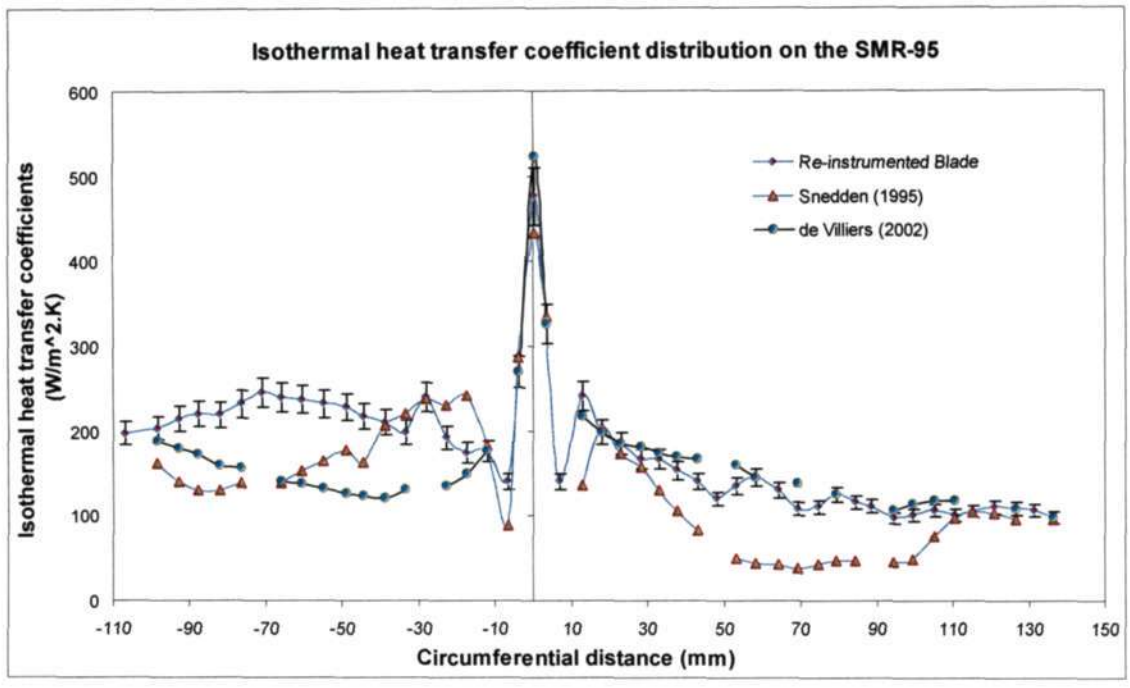

Figure 6-15 Isothermal heat transfer coefficient distribution using the re-instrumented test section

Although the sensitivity of the gauges using the new platinum paint did not sufficiently increase when compared to the old gauges, a more consistent distribution of heat transfer coefficients was generated. The sensitivity of the gauges was tested using a hot air gun and the step output noted using Waveview software. The noted electrical noise picked up was also in line with the old gauges and this was expected as no modifications were made to the existing heat transfer analogy. The results on the pressure surface did not correlate with either Snedden (1995) or de Villiers (2002). The results on the suction surface however, closely resembled that of de Villiers (2002). This deviation of results on the pressure surface further facilitated the need for a repeatability test to determine its experimental validation. The result for experimental repeatability is presented below in Figure 6-16.

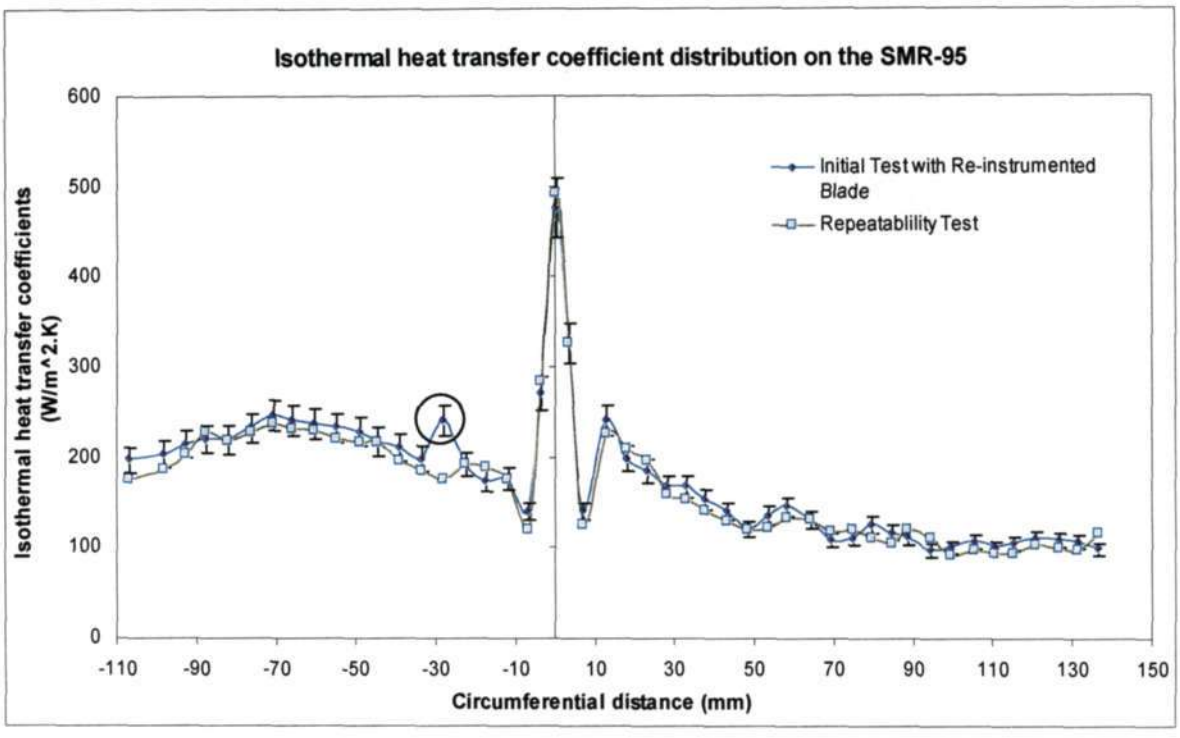

Figure 6-16 Isothermal heat transfer coefficient repeatability test

The results of repeatability validated the heat transfer distribution on both the pressure surface and suction surface. With the general trend of experimental data sets being confirmed, only one data point was corrected and this is encircled in Figure 6-13. The final heat transfer coefficient distribution which was to be used for CFD validation and experimental analysis is presented below in Figure 6-17.

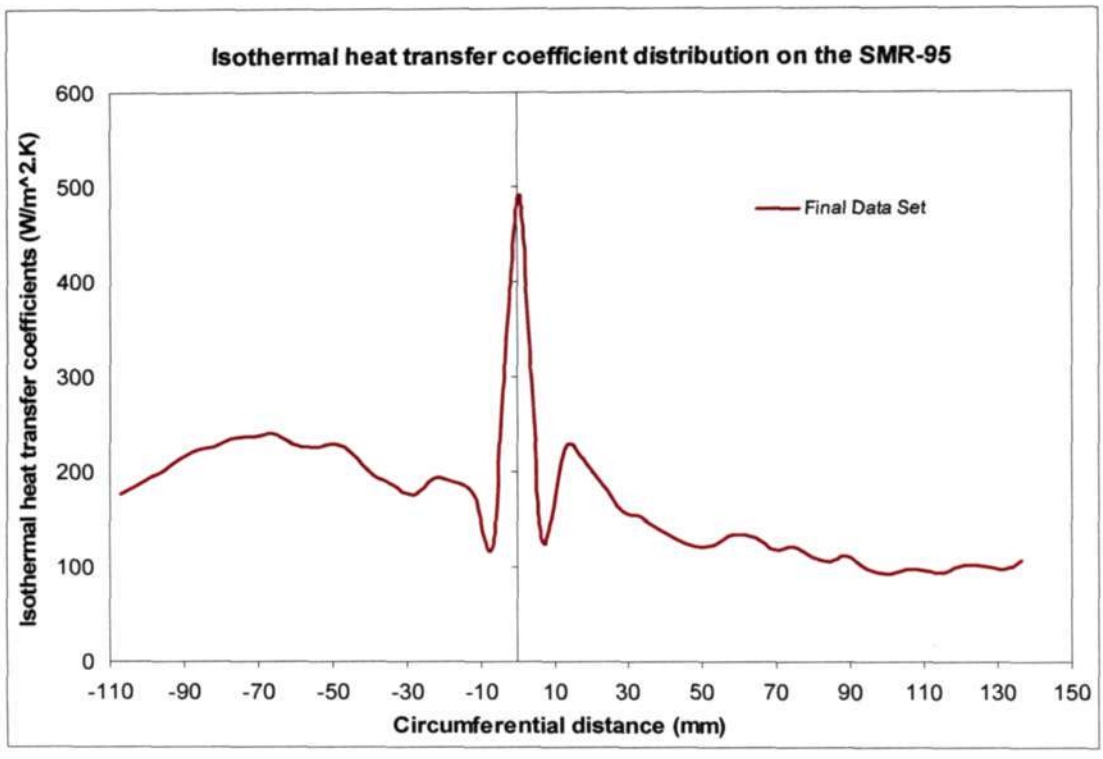

Figure 6-17 Final isothermal heat transfer coefficient distribution

6.3.5 Experimental Heat Transfer Analysis

In this analysis, the experimental heat transfer patterns were correlated with the qualitative details produced from the static pressure distributions and Mach number plots. The highest level of heat transfer occurs at the stagnation point on the leading edge, which ranged around 495 W/m^2K as shown in Figure 6-17. This was indicative and in full agreement with the no velocity condition produced as the flow impinges on the blade. Being that the leading edge area of the SMR-95 profile is circular, the heat transfer coefficients drop drastically as a function of its high angle step change accompanied by the generation of a separation bubble, which was noted by Stieger (1998). This rapid acceleration of flow which is accompanied by thin boundary layer formation accounts for the low levels of heat transfer. The typical values ranged around 110 W/m^2K at 10mm CD on both the pressure and suction surfaces. These results were in conformance with the theory of cylinders exposed to cross-flow.

The separation bubble is then followed by the turbulent re-attachment of the flow on the pressure surface which accounts for the increase in heat transfer to approximately 190 W/m^2K as shown in Figure 6-17. Figure 6-17 then exhibits an increase in heat transfer to approximately 250 W/m^2K at 70mm CD on the pressure surface. This is primarily because of the increased

flow velocity towards the throat section of the profile. The heat transfer coefficients then drop to 190 W/m^2K as the flow makes its way towards the trailing edge of the blade where an expected shock wave would account for this decrease. On the suction surface, the heat transfer coefficients drop at a much slower rate because of the lower acceleration levels which results in thicker boundary layer formations. Therefore, as the turbulent boundary layer grows, the heat transfer coefficients stabilises to about ±100 W/m^2K from 55-140mm CD suction side, as shown in Figure 6-17.

CHAPTER 7

NUMERICAL MODEL VALIDATION AND DEVELOPMENT

7.1 Introduction

The usage of numerical modelling techniques has certainly proven itself to be an invaluable engineering tool in the complex field of jet engine aerothermodynamics. With its vast capabilities of predicting various vital flow characteristics, engineers and researchers alike could perform their required design investigations with minimal costs and time incurred. However, in order to ensure the accuracy of numerical predictions, experimental validations are performed. Once validated, the numerical model could be further developed and optimised with sufficient confidence in the code used. This chapter deals with such a methodology.

The experimental static pressure and heat transfer results generated over the SMR-95 blade profile were used as validation criteria for the numerical model analysed in FLUENT. These two experimental data sets were used in the event that changes in numerical parameters may not necessarily bring about corresponding changes in predictions. The numerical comparisons were done using a 2-D model of the SMR-95 cascade. Its development came about from the initial research investigations conducted by de Villiers (2002). The work done by de Villiers provided a solid platform of which the author built on. The model created by de Villiers was further refined by improving on the mesh quality and the resulting predictions compared against the generated experimental data. Different turbulence models were also investigated and the one displaying the closest correlation to experimental results was used to further the investigation.

The 2-D model was initially used for the comparisons as this requires significantly lower processing power. The validated 2-D model of the cascade was then expanded to 3 dimensions which would not only bring about a better resolution of results but also predict complex 3-D flow phenomena associated with high speed gas turbine flows.

7.2 Model Specification

The first step in setting up a model in FLUENT is creating the geometry of question. The pre-processor used by FUENT to create and mesh the geometry is GAMBIT. Being that the

experimental results were taken over the midspan of the blade profile, a 2-D model of the cascade was therefore seen as sufficient for the numerical validation. The author did however consider modelling a periodic setup of the blade and entire experimental facility i.e. cascade, radiator and plenum. But, the experimental periodicity results were poor and there was no accurate knowledge of the boundary conditions within the plenum.

In all the cases discussed in this chapter, the solver that was used was FLUENT 6.2. This version of FLUENT was designed to solve both structured and unstructured meshes. For all the simulations performed in FLUENT, the coupled solver with implicit formulation was chosen because of the compressible flow conditions. This solver uses 2nd order upwinding for the governing equations and 1st order upwinding for the additional turbulence scalar equations. The discrete equations are solved by Gauss-Siedel point iteration together with the AMG solver. The default Courant number for the coupled implicit solver is 5, but was varied according to the different turbulence models used to achieve and speed up convergence. Table 7-1 below provides the noted courant numbers that brought about convergence for the respective turbulence models used.

Table 7-1: Courant numbers used for specified turbulence models

Turbulence Model	Courant Number
Spalart-Allmaras (SA)	20
Realizable $k-\varepsilon$ (RKE)	9
RNG $k-\varepsilon$,	9
Standard $k-\omega$ model	9
SST $k-\omega$	15

7.2.1 Boundary Conditions

In order to achieve an accurate correlation between experimental and numerical predictions, the most crucial factor is the setting of exact boundary conditions. The three different types of boundary conditions used for the cascade model were walls, pressure inlet and pressure outlet. These boundary conditions were stipulated by the data captured during the experimental runs. The cascade inlet and outlet edges were specified as pressure inlet and pressure outlet boundary

conditions respectively. All the remaining edges were specified as wall boundary conditions. The edges of the test blade were split into its respective pressure and suction sides and were assigned a temperature of 313 K to allow for heat transfer into the surface. The models boundary conditions setup is graphically show in Figure 7-1. The data entered for the pressure inlet ad outlet boundary conditions are presented in Table 7-2 and 7-3 respectively.

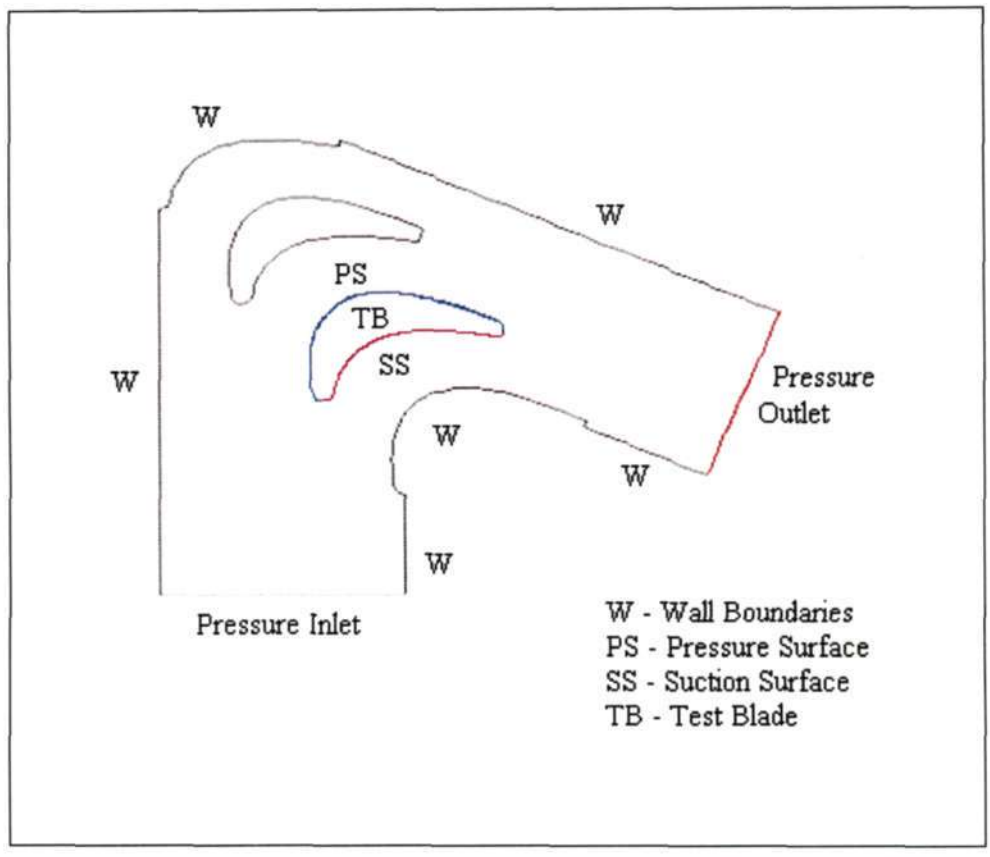

Figure 7-1 GAMBIT and FLUENT geometry with specified boundary conditions

The total gauge pressure was set to 40 kPa. This pressure and all other pressures were set relative to the operating pressure of 0 Pa which is used and explained in section 7.2.3. The "Supersonic/Initial Gauge Pressure" criterion refers to the static pressure at the cascade inlet which was determined from experimental data. The "Total Temperature" refers to the total stagnation temperature at the inlet also determined experimentally using the total temperature Kiel probe. The "Turbulence Specification Method" was set to "Intensity and Hydraulic Diameter" with the intensity level set to 3%. This corresponds to a free inlet which was theoretically and experimentally determined by Snedden (1995, 1998) using a hot wire probe. The numerical predictions of these intensity levels can be found in Appendix 6 of Snedden (1995). The hydraulic diameter was set to the characteristic length of the inlet i.e. the width.

Table 7-2: Pressure inlet boundary condition parameters

Setting	Value/Method
Gauge Total Pressure (Pa)	40 000
Supersonic/Initial Gauge Pressure (Pa)	35 000
Total Temperature (K)	373
Direction Specification Method	Normal to Boundary
Turbulence Specification Method	Intensity and Hydraulic Diameter
Turbulence Intensity (%)	3
Hydraulic Diameter (mm)	118.72

Table 7-3: Pressure outlet boundary condition parameters

Setting	Value/Method
Gauge Total Pressure (Pa)	40 000
Supersonic/Initial Gauge Pressure (Pa)	35 000
Total Temperature (K)	373
Direction Specification Method	Normal to Boundary
Turbulence Specification Method	Intensity and Hydraulic Diameter
Turbulence Intensity (%)	3
Hydraulic Diameter (mm)	467

7.2.2 Material Selection

The setting of the material property when analysing compressible fluid flow is another very important factor. The most important part is setting the density of the operational fluid to an "ideal-gas". If this is not set, the model will not be solved as a compressible flow problem and errors will result. The density is therefore specified ideal-gas properties. Other material properties may be manually set, such as specific heat, thermal conductivity and viscosity. These were however left at the prescribed FLUENT default values. Although various relationships can be selected such as piecewise-linear/polynomial or kinetic, which employ the temperature of the flow to derive these parameters. By prescribing ideal-gas properties to the density, the solver recognises that the flow is compressible and automatically enables the energy equation to allow for heat transfer.

The "ideal-gas" equation modelled in FLUENT is given below in equation 7.2.2.1

$$\rho = \frac{p_{op} + p}{RT} \tag{7.2.2.1}$$

Where p_{op}, is the operating pressure, p the local relative gauge pressure and R is the universal gas constant, which is 287 KJ/kgK.

7.2.3 Operating Pressure

The operating pressure is another important factor to consider when setting up the CFD model because as shown in equation 7.2.2.1, it directly determines the corresponding density. Furthermore, it is also significant in low Mach number flows because of its role in avoiding round-off errors. The recommended settings stipulated by FLUENT for the operating pressure is shown below in Table 7-4.

Table 7-4: Recommended settings in FLUENT for operational pressure

Density Relationship	Mach Number Regime	Operating pressure
Ideal gas law	M>0.1	0
Ideal gas law	M<0.1	Mean flow pressure

Because the plenum operates under a vacuum and the experienced flow velocities are in excess of M > 0.1, the operating pressure was set to "0".

7.2.4 Initialisation and Convergence Criteria

Before iteration of the solution can commence, the domain needs to be initialised. In all simulations, the entire domain was initialised with the velocity, gauge pressure and temperature values prescribed at all zones. The turbulent kinetic energy and turbulence dissipation rate were initialised to the values computed by FLUENT. It was noted that by initialising the velocities from all zones to zero resulted in faster convergence.

The most vital part of any simulation is attaining convergence. This requires that various factors which govern the solution need to be accurately set to suit the type of simulation. Because of the iterative nature in the solution procedure, there is no common rule for judging convergence. Iteration is used to handle the non-linearity of the equations that govern the fluid flow, heat transfer and other related processes. For the conservation equation, an approximate solution is obtained with each iteration that results in a small imbalance in the conservation equation. During the solution algorithm, the imbalance in each cell is a small non-zero value that decreases as the solution progresses. This imbalance is called the residual and is scaled for different variables so that it can be compared. The scaling factors are taken from the bulk flow of the variables through the domain.

The convergence criterions are pre-set conditions on the residuals that indicate a certain level of convergence. The default FLUENT settings requires that all the scaled residuals decrease to 10^{-3}, which indicates that the overall error in the variables is three orders of the magnitude less than the bulk value in the system. For all the simulations conducted in this dissertation, the scaled residuals were set to 10^{-3}, except for the energy and continuity equations for which the criterion was 10^{-5}.

Other convergence criterion used was monitoring the drag coefficient and mass flow balance at the flow boundaries. The solution was considered converged when the drag coefficient remained constant for about 300 iterations and the mass flow rate difference through the pressure inlet and outlet flow boundaries was less than 0.01%.

7.2.5 Grid Independence and Adaptation

The process of ensuring that correct solutions are generated was facilitated by conducting a grid sensitivity study for each model created. The idea is to demonstrate that the solution was insensitive to the size of mesh. The grid insensitivity was determined by computing a solution for a specific model, refining the mesh in critical regions, and then comparing the results until changes could no longer be detected. Once this is achieved, the grid would then be deemed independent and results generated could be compared against experimental predictions. Deviations in results from the corresponding numerical validation could then be owed to the numerical code used or entire CFD model.

The most vital factor in obtaining accuracy of any CFD simulation is achieving a quality mesh. As mentioned earlier, the geometry is meshed in the pre-processor, GAMBIT. The refinement of the mesh however can also be done in FLUENT as it allows for a solution-based grid adaptation. This is done based on specific values or gradients of various flow characteristics such as velocity, temperature, pressure or turbulence. It also allows adaptation based on a wide range of desired wall unit values, or on specific flow boundaries. In all models the grid was adapted according to its y^+ values.

7.3 Numerical Model Validation

The numerical validation was initiated by building on the model previously created by de Villiers (2002). This was done because there were no changes in the experimental model that facilitated the need for geometry modifications in the numerical investigation. The grid however, was firstly refined by improving on the mesh quality. The refinement included upgrading the existing pave meshing scheme by improving on aspects such as EquiAngle skewness, cell size variations and boundary layer meshes. Another strategy implemented was to decompose the entire geometry. This was done by breaking up the cascade model into smaller regions that could allow for the quadrilateral cells to be perfectly mapped, resulting in a highly structured mesh. The meshing strategies of both cases were simulated using different turbulence models and compared against the experimental results of static pressure and heat transfer from which conclusions were drawn. Based on these comparisons, the model was expanded to 3 dimensions, which allowed for secondary complex 3-D flow phenomena to be determined and included in the subsequent comparisons.

7.3.1 Refinement of de Villiers Mesh (Grid 1)

The meshing scheme used by de Villiers (2002) was further refined using the tools of the FLUENT pre-processor, GAMBIT. A boundary layer mesh with 27 rows, a first row size of a=0.001 mm and a growth factor b/a = 1.2, were applied on the middle two blades of the cascade model. A pave meshing scheme with quadrilateral elements having an interval size of 1.5 completed the operation. Examination of the mesh was also done using GAMBIT and revealed minimal cell size variations and a worst cell EquiAngle skewness of 0.52. FLUENT states that cells with EquiAngle skewness of 0.8 and above will not converge. In order to maintain solution stability and accuracy the skewness levels should be below 0.6. With the amount of cells in the model totalling 18468 and all parameters within the accepted limits, the model was exported for analysis. An illustration of the initial grid analysed i.e. Grid 1 is given in Figure 7-2 below.

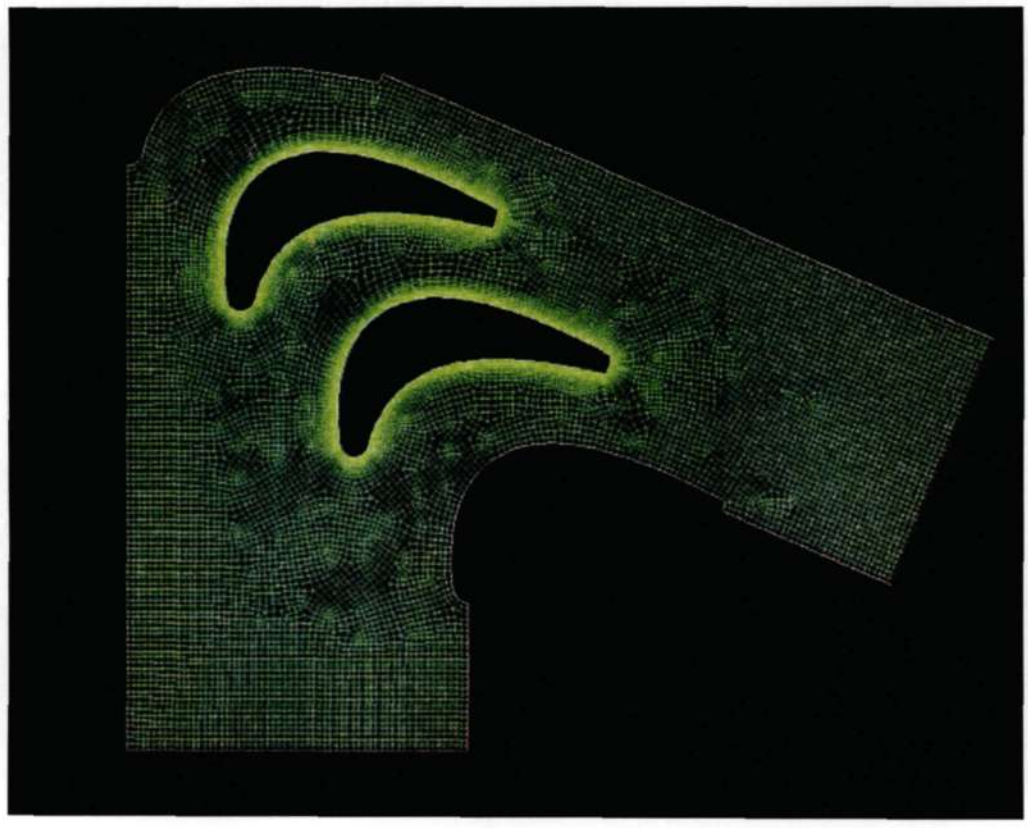

Figure 7-2 Refined version of de Villiers (2002) mesh, Grid 1

Grid 1 was simulated using four different types of turbulence models at the conditions given in Tables 7-2 and 7-3. These models were Spalart-Allmaras (SA), RNG $k-\varepsilon$, Realisable $k-\varepsilon$ (RKE), and SST $k-\omega$. The Standard $k-\omega$ model was also investigated in all the subsequent models. The outcome of this model displayed a solution which was almost identical to the SST

version. This was expected as the only difference is that the SST model is that it incorporates a blending function that allows it to switch from the standard $k-\omega$ model in the near-wall region to a high Reynolds number version of the $k-\varepsilon$ model in the free stream. It was therefore omitted from the comparisons. A more detailed description of the models under investigation is given in chapter 3 of this dissertation.

The experimental static pressure distribution comparisons using grid 1 for different turbulence models is presented in Figure 7-3. The corresponding experimental heat transfer coefficient distribution comparison follows that in Figure 7-4.

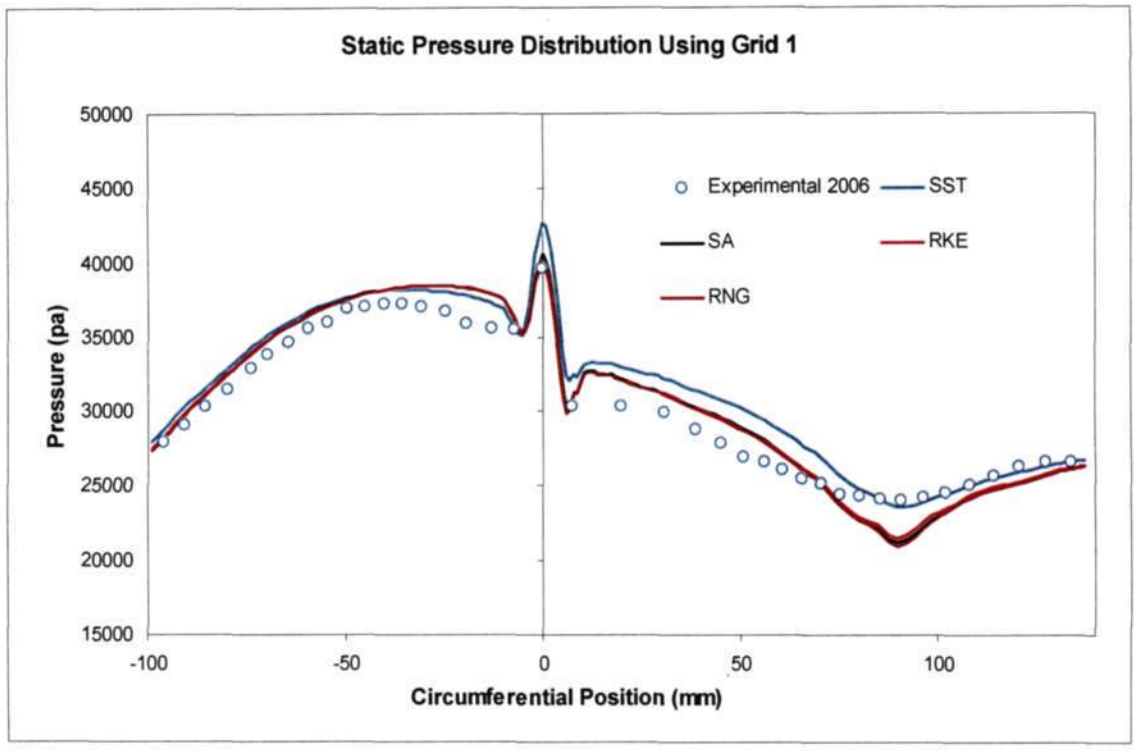

Figure 7-3 Comparison graphs of static pressures using different turbulence models for Grid 1

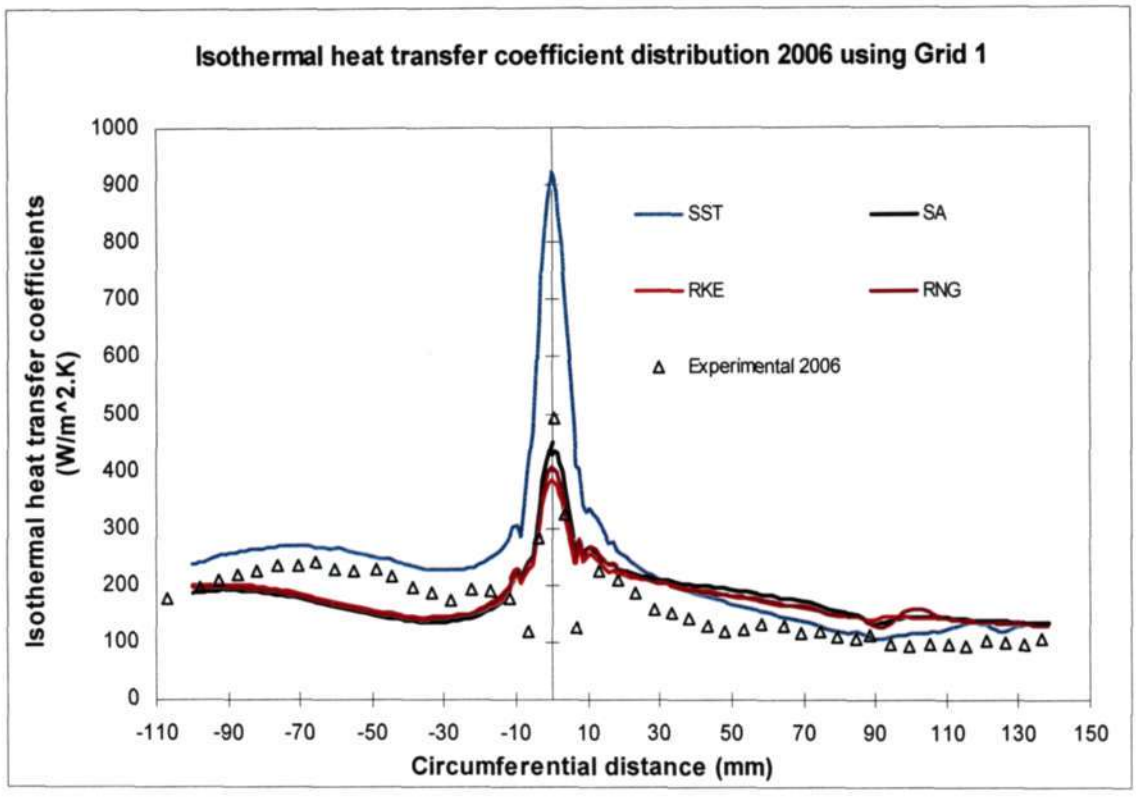

Figure 7-4 Comparison graphs of heat transfer using different turbulence models for Grid 1

Investigations of the static pressure comparisons showed that all the turbulence models correlated extremely well to the experimental results from about 100-35 mm pressure surface. The corresponding experimental heat transfer results however, indicated a pattern that was closely followed by the SST turbulence model.

From 35-10 mm pressure surface, where the flows acceleration levels increases slightly and heat transfer rates decrease, the CFD results of pressure tended to over predict for all the turbulence models. The heat transfer results of the SST model over predicted in this region as well, but the remaining turbulence models under predicted.

At 10 mm pressure surface, where the experimentally noted separation bubble occurs right up till the leading edge, the results from the SST model vastly over predicted. This was clearly evident in both experimental comparisons. The numerical deviation of results in this model further extended its trend up unto 10 mm suction surface. Inspection of the corresponding flow field velocity vector plots also failed to reveal the formation of a separation bubble in this region. The resulting turbulence models however, did produce much more accurate correlations in both pressure and heat transfer comparisons. Velocity vector plots also revealed the

separation bubble formation at about 10 mm pressure surface where the flow reverses. This is shown below in Figure 7-5, which was a velocity vector plot taken from the RNG model.

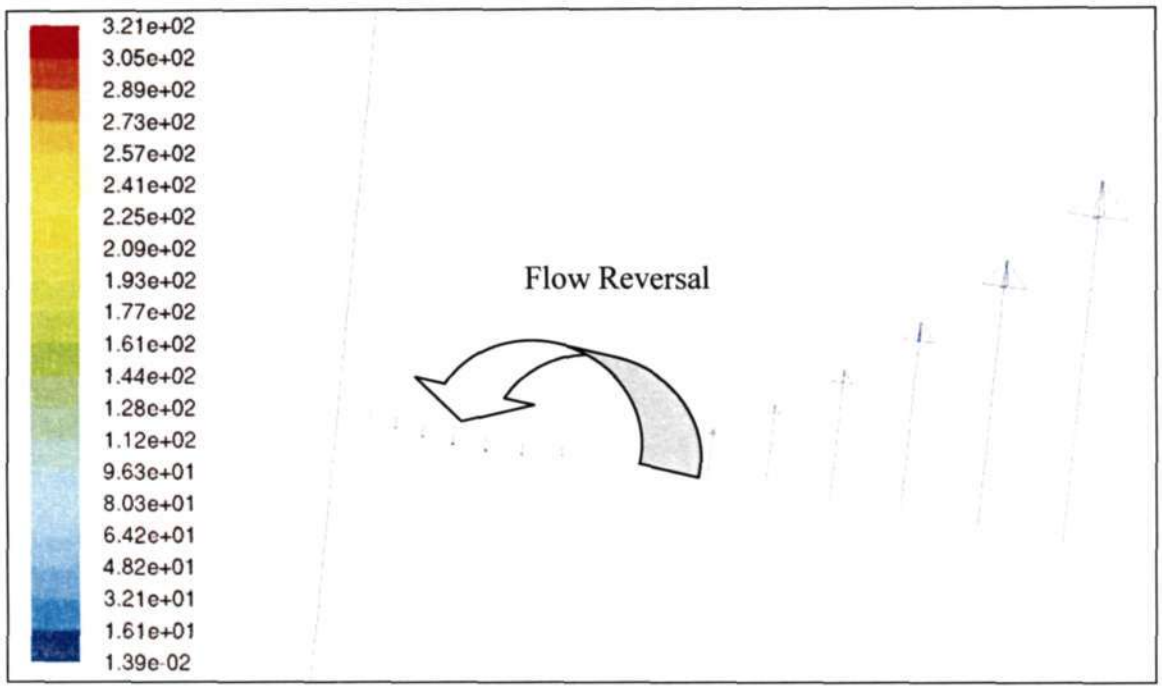

Figure 7-5 Velocity vector plot illustrating flow reversal, taken from the RNG turbulence model at approximately 10 mm pressure surface

As of 10-70 mm suction surface where the flow accelerates to transonic conditions, all the turbulence models over predict in both experimental correlations. With the over predicting trend of decreasing static pressures being higher in the SST model, its corresponding heat transfer coefficients displayed much better recovery rates and closer correlations. When transonic conditions were attained at 90 mm suction surface, the SST model accurately predicted the static pressures and heat transfer coefficients. This trend was further continued until the trailing edge of the blade profile. The remaining turbulence models however depicted much steeper gradients in static pressures and slightly higher heat transfer coefficients. Contours of velocity within the cascade using the SST and SKE models are given below in Figures 7-6 and 7-7 respectively. Based on these figures, it can be clearly seen how diverse the different turbulence models are when predicting the flow field at transonic conditions.

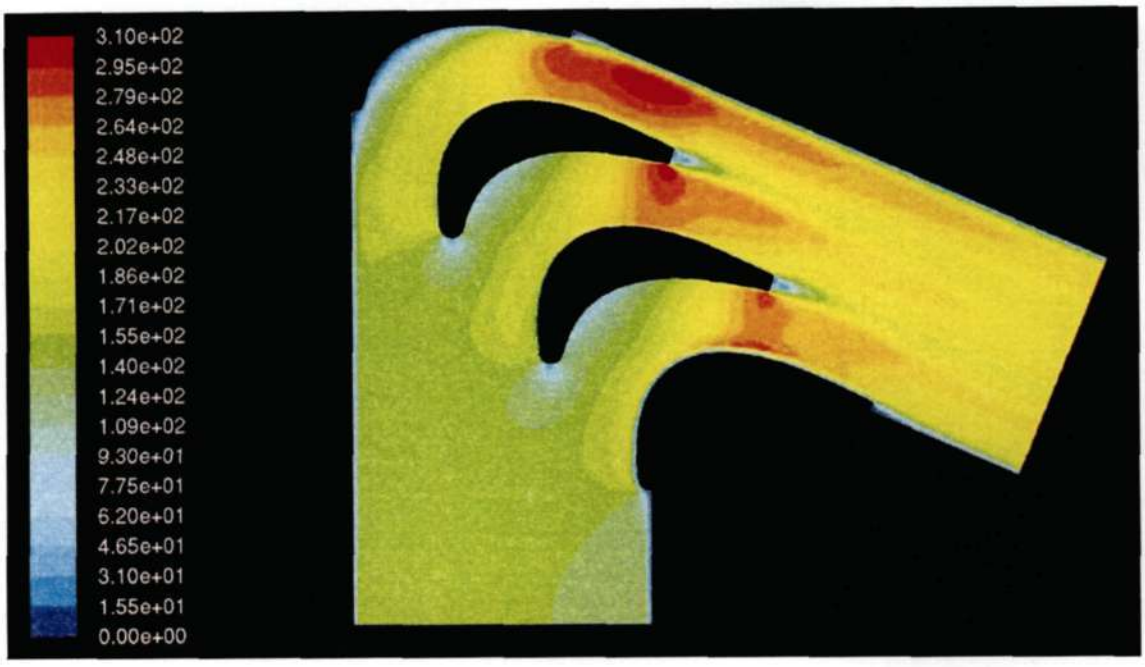

Figure 7-6 Velocity contour distribution using the SST turbulence model

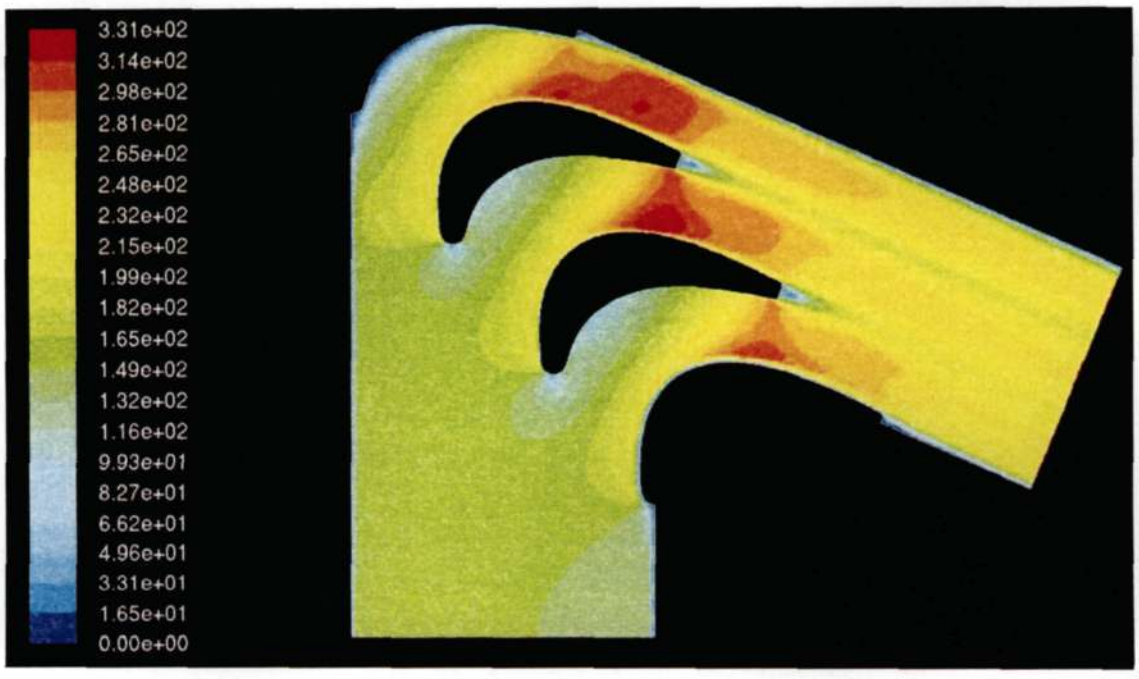

Figure 7-7 Velocity contour distribution using the SKE turbulence model

7.3.2 Decomposed model (Grid 2)

To achieve a highly structured grid using only quadrilateral cells, the entire cascade geometry was pain stakingly sub-divided into smaller 4 sided sections. These sections allowed for the

precise mapping of quad cells. The mapping scheme also provides control of the mesh where the edge nodes are mapped on the opposite side of the region, resulting in almost orthogonal cells. A boundary layer mesh was applied on the test blade with 27 rows, a first row size of a=0.01 and growth factor of b/a=1.2. This mesh was noted to produce y^+ values less than or close to 1 for the majority of the blade surface. The decomposed sections were meshed using the mapping scheme and quad elements with an interval size of 1. The total number of elements was 388880 and an illustration of the decomposed geometry is presented in Figure 7-8.

The decomposed grid was simulated under the exact same conditions as Grid 1 with same turbulence models used. The results from the static pressure and heat transfer comparisons are presented in Figures 7-9 and 7-10 respectively.

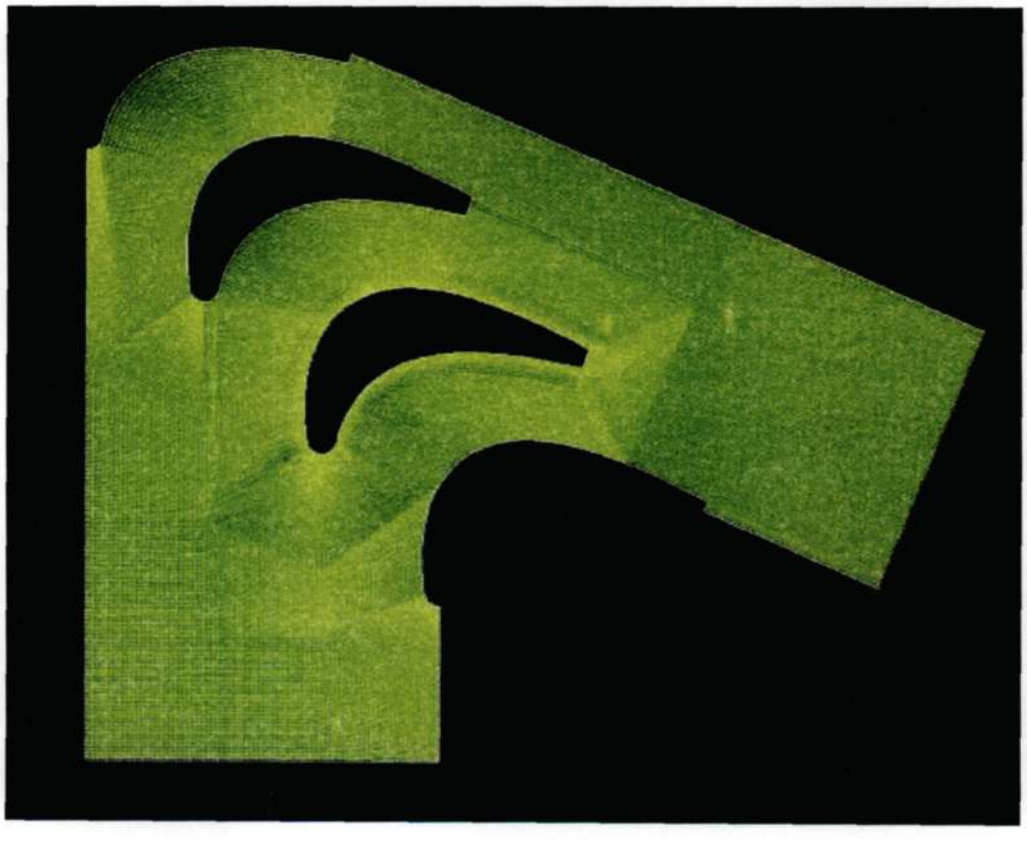

Figure 7-8 Decomposed cascade geometry, Grid 2

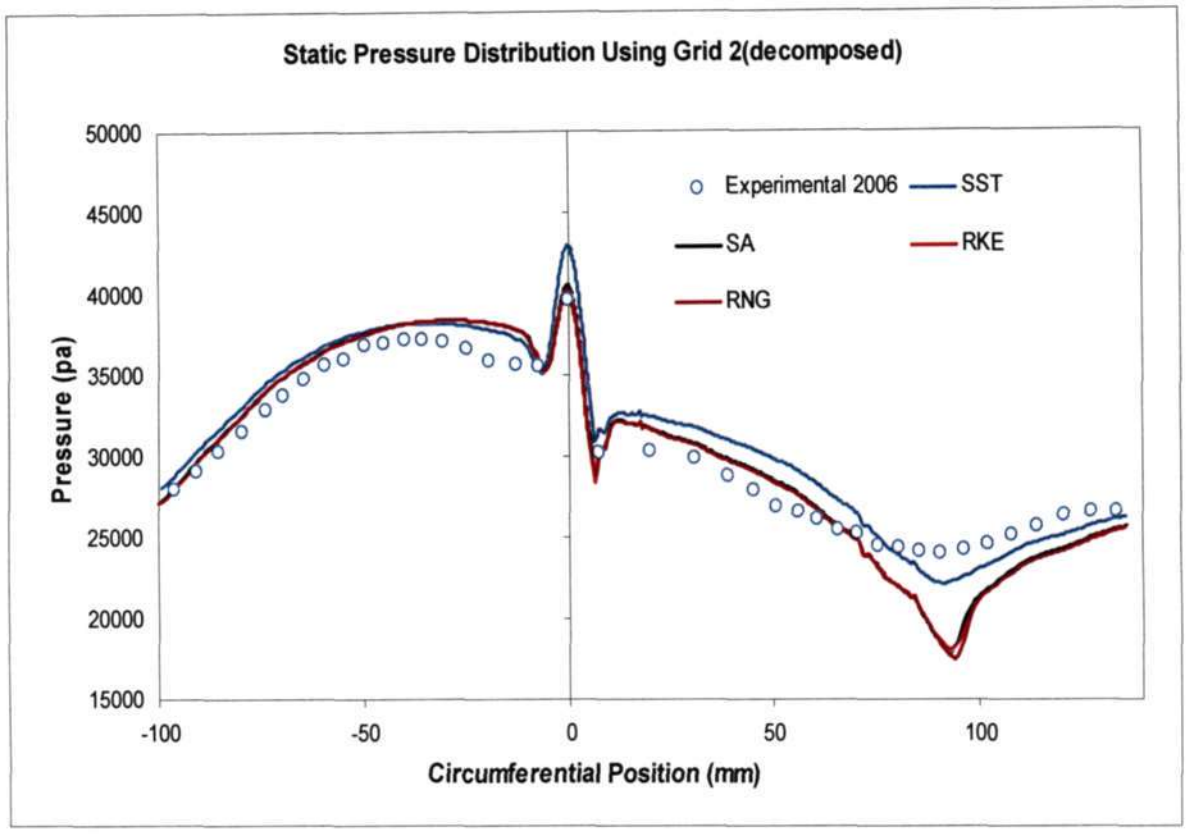

Figure 7-9 Comparison graphs of static pressures using different turbulence models for Grid 2

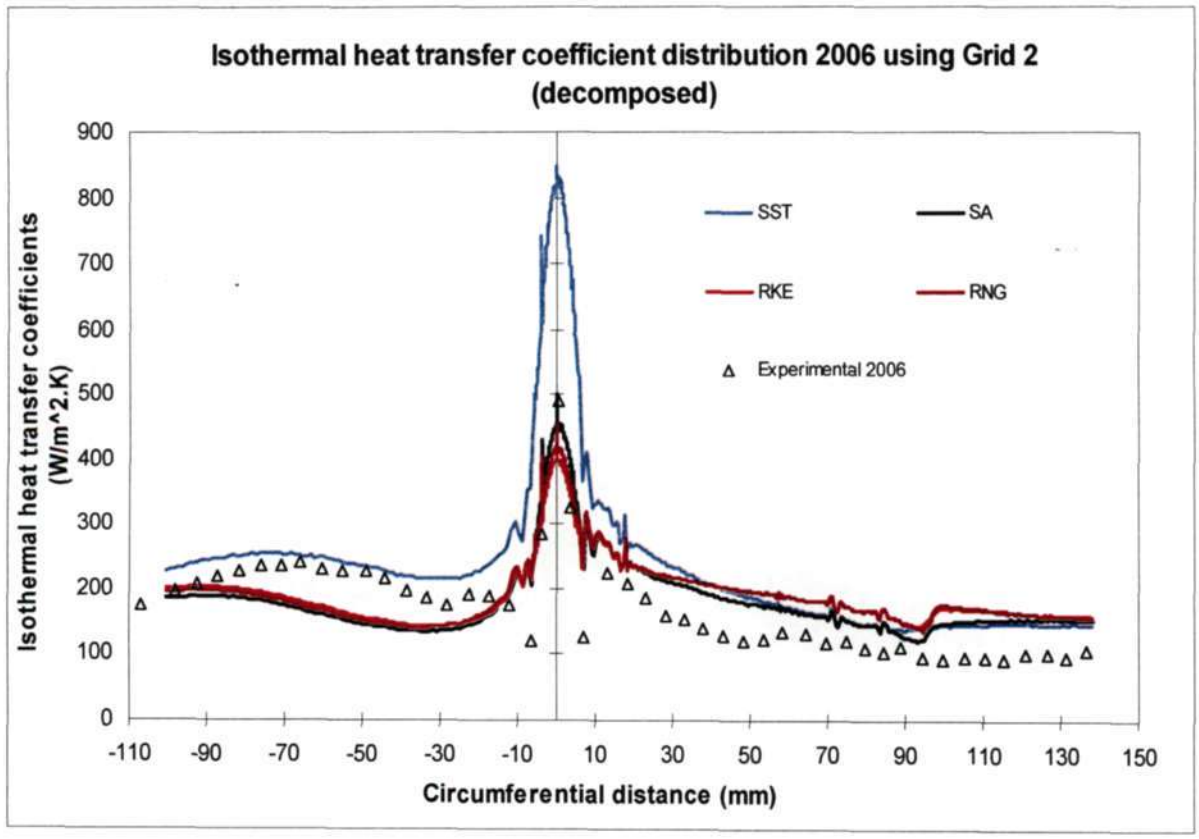

Figure 7-10 Comparison graphs of heat transfer using different turbulence models for Grid 2

With convergence times almost tripling due to the increased amount of cells, the results showed virtually no change. The most notable discrepancy however occurred in the pressure comparison at 90 mm suction surface where the flow enters transonic conditions. This discontinuity which was experienced because of the generated shock wave caused a much steeper gradient in results when compared to grid 1. The reason for the smaller dip in results from the pave meshing scheme is because the discontinuity is smeared out when compared to the decomposed mesh. Another reason is because a refined boundary layer mesh was not implemented on the second blade situated above the test blade. Although one is not interested in this blade, it is important because transonic conditions result as of this blades interaction at the trailing edge. A closer look at the velocity contours used of the SA model presented in Figure 7-11 further illustrates this point.

Although improvements in the decomposed mesh will bring about better accuracy and exhibit the superiority in this form of meshing strategy what was noted to be more important was the choice of turbulence model.

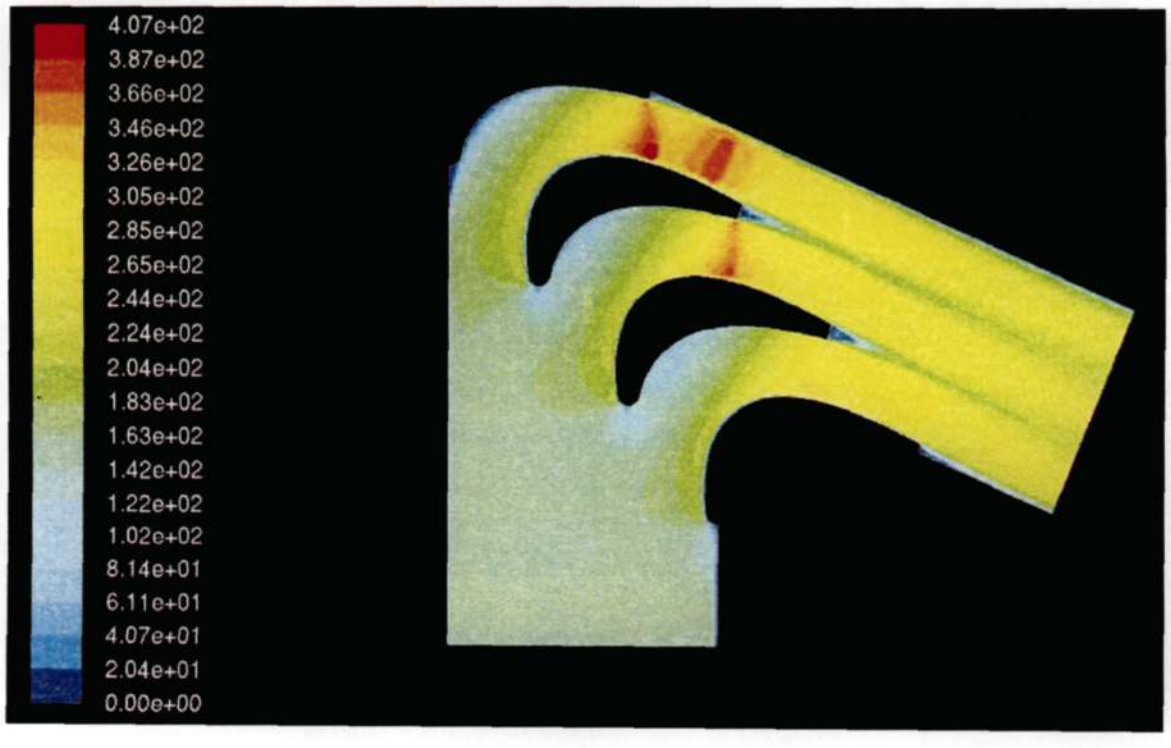

Figure 7-11 Velocity contour plot of the SA turbulence model using Grid 2

7.3.3 3-D Cascade Model (Grid 3)

A 3-D model of the cascade was constructed by projecting its corresponding 2-D version in the co-ordinate axis Z direction. The projection was done to 80 mm blade span with the respective mesh used in Grid 1. This mesh was used because of its significant savings in processing time without compromising on the quality of numerical results. The purpose of constructing a 3-D model was to include secondary flow effects such as horseshoe vortices and note the corresponding change in results. The outcome of the model would also be able to provide pressure and heat transfer distributions in the spanwise direction of the test blade.

The model was simulated under the same conditions used in 2-D versions but with the 3-D solver settings of FLUENT. The boundary conditions were also set in the same fashion as the 2-D model but faces were specified instead of edges. An illustration of the created 3-D model is given in Figure 7-12 and the corresponding mesh in Figure 7-13. The mesh consisted of 295904 cells of which all aspects such as cell skewness and size variations lying within the stipulated ranges of FLUENT.

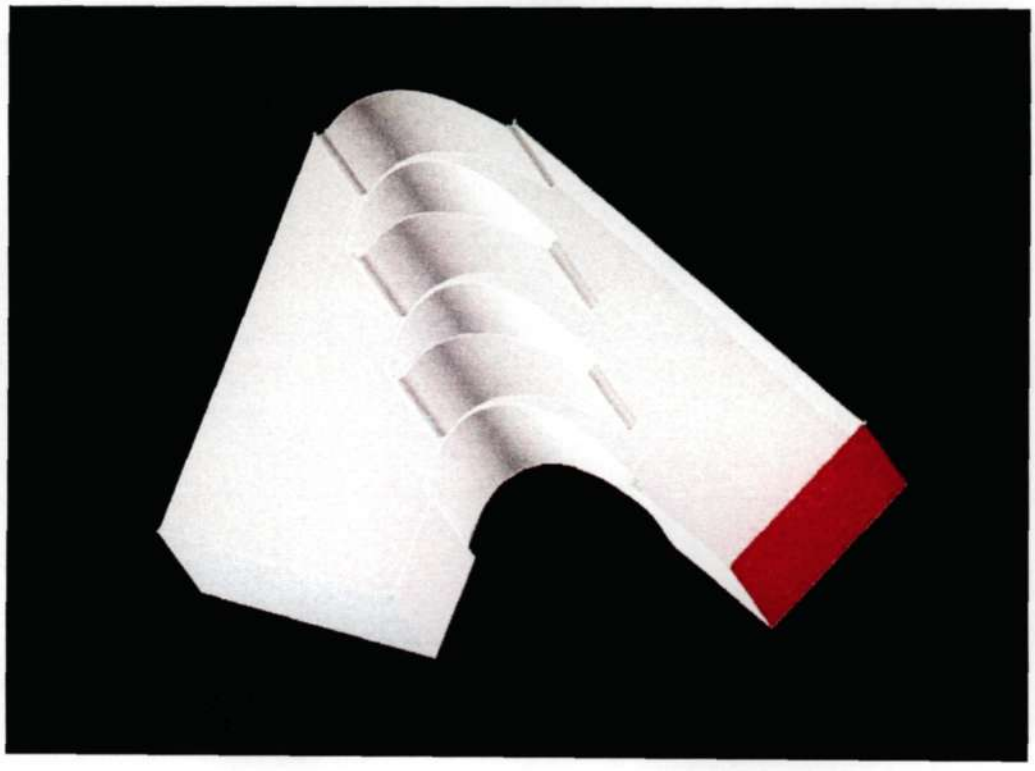

Figure 7-12 3-D model of the cascade

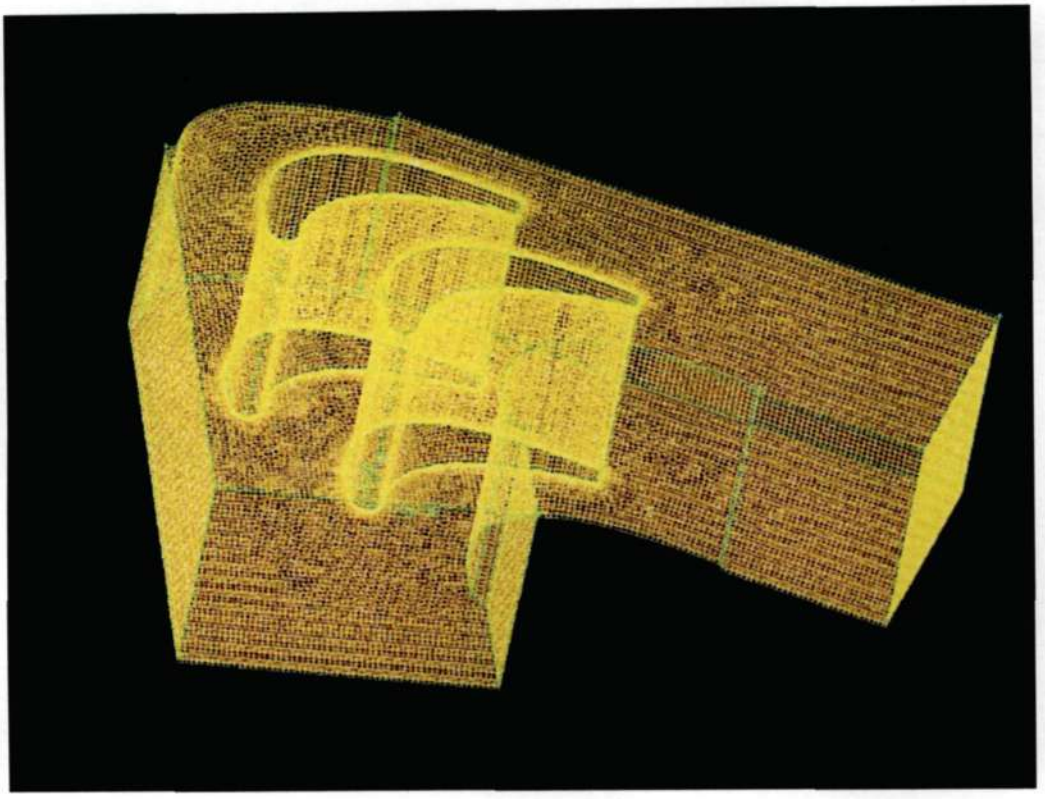

Figure 7-13 Gambit projected mesh of the 3-D cascade model

The 3-D cascade model was simulated using all the turbulence models of 2-D version. The Courant numbers presented in Table 7-1 were used for the respective turbulence models and the discretization was done using the third order muscle function. The results for comparison were taken at 40 mm blade span by creating an iso-surface over the test blade's pressure and suction surfaces respectively. Naturally, the results were compared against the experimental data of static pressures and heat transfer coefficients of which the comparisons are presented in Figures 7-14 and 7-15 respectively.

The outcome of the static pressure investigations on the 3-D model yielded no changes in results for all turbulence models. This concluded that secondary flow effects played no part in changing the static pressure distributions over the midspan of the profile and that a 3-D model would not be necessary to validate its corresponding experimental results.

The isothermal heat transfer distributions displayed no significant changes in predictions on the pressure side of the profile but the results from the suction side did increase by approximately ±25 W/m^2K. This constant increase occurs from 25 mm suction side till the trailing edge.

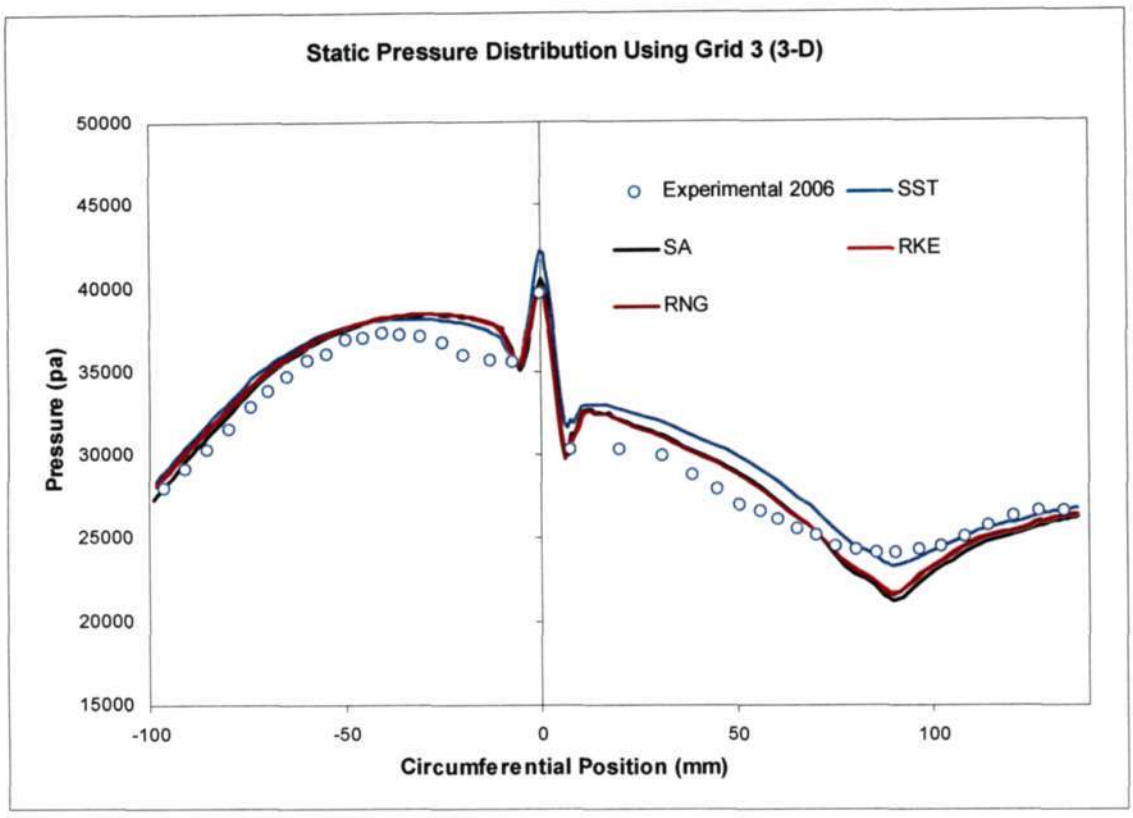

Figure 7-14 Comparison graphs of static pressures using different turbulence models for Grid 3

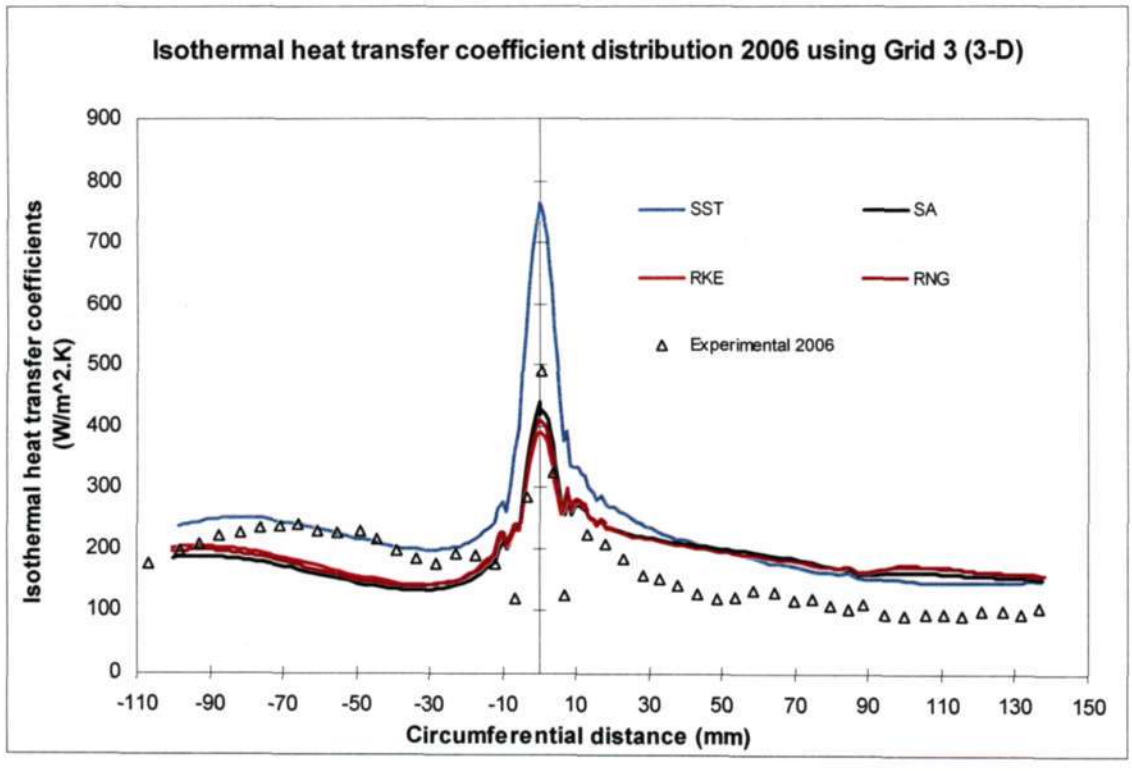

Figure 7-15 Comparison graphs of heat transfer using different turbulence models for Grid 3

Although the comparison results from this model were within acceptable limits, its 3-D nature was used to bring about a better resolution of the flow field within the cascade and around the test blade. A spanwise pressure distribution taken over the pressure and suction surface of the test blade using the SST turbulence model, shown in Figures 7-16, helped explain why no notable differences occurred in the static pressure comparisons. Contours of the corresponding surface heat transfer coefficients taken in the spanwise direction are presented in Figure 7-17.

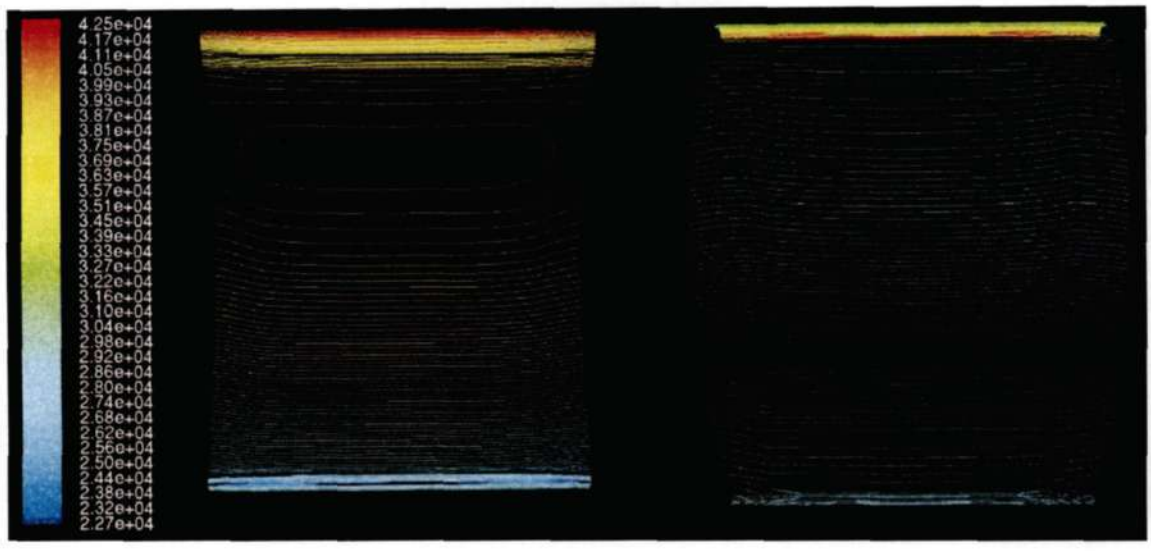

Figure 7-16 Pressure contours taken in the spanwise direction over the concerned test blade, shown as pressure surface (left) and suction surface (right)

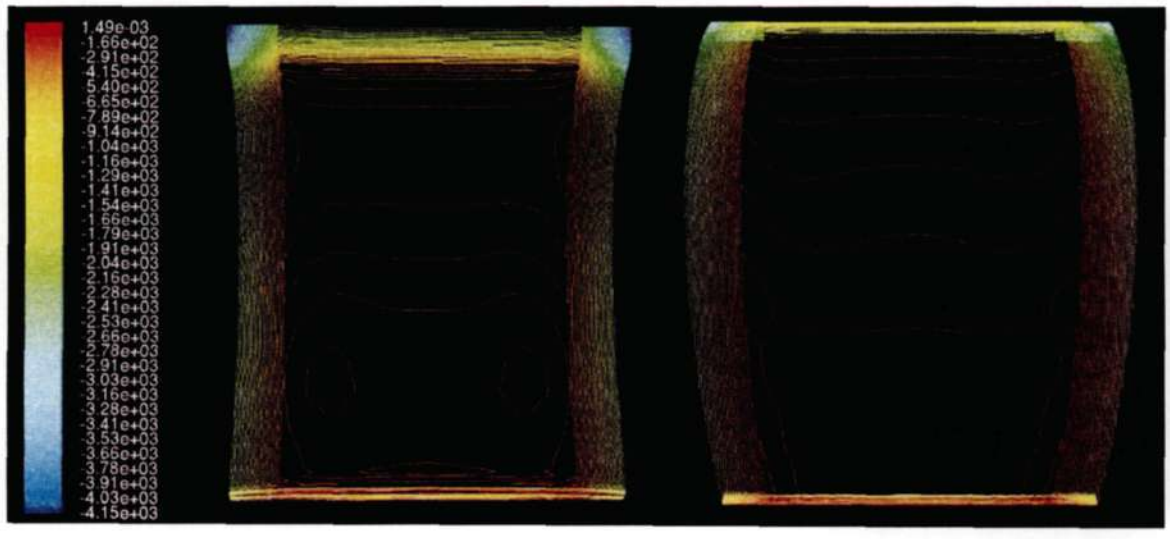

Figure 7-17 Surface heat transfer coefficient contours taken in the spanwise direction over the concerned test blade, shown as pressure surface (left) and suction surface (right)

As shown in Figure 7-16, the distribution of pressures is symmetrical about the blades midspan. It is for this reason that no notable changes were observed between the static pressure comparisons of the 2-D and 3-D model. Analysis of the surface heat transfer coefficient distributions in Figure 7-17 indicated high heat transfer rates near the cascade endwall especially at the leading edge. Note that in this case, the scale is reversed and the blue regions indicate higher rates of heat transfer. The precise reasons for the increased heat transfer rates were unknown at present but studies into the complex field of endwall heat transfer provided the key.

The reason for the high levels of heat transfer is because of the formation of two horseshoe vortices. A review of Goldstein and Spores (1988) illustrated that secondary flows by the endwall region are primarily the result of two main pressure gradients existing in the vane passage. The pressure variation in the passage is caused by the boundary layer velocity distribution and flow stagnation on the blade. These pressure variations cause the flow to be forced toward the endwall and roll up into two legs of the leading edge vortex. The high turning angle of the main flow field between the blade airfoils causes another strong pressure gradient across the passage. This gradient then affects the path of the two horseshoe vortices formed. The formed pressure side leg horseshoe vortex becomes the passage vortex and moves closer to the suction side leg horseshoe vortex. The suction side vortex then instead of adhering to the suction surface, wraps itself around the passage vortex. As the flow progress through the passage the vortices enlarge. The increased heat transfer noted on the suction surface could therefore be as a result of these secondary flows. Goldstein and Spores (1988) indicated that complex heat transfer patterns could result because of these vortices but generally the outcomes are enhanced heat transfer rates.

7.3.4 Numerical Validation Conclusions

The CFD results presented in this chapter has certainly proven itself to provide detailed insight into the flow within the investigated cascade. The 2-D validation and 3-D model development brought about significant increases in data resolution. The investigations of the various turbulence models using different grids had also yielded significant findings.

The results from investigating different turbulence models displayed the SST $k - \omega$ model's superiority in predicting wall bounded flows and transonic conditions. However, this model significantly lacked in areas where large flow separation is encountered typically at the leading edge where the model over predicted in both heat transfer and static pressure. Failure of this

model to predict the leading edge separation bubble further supported its deficiency in this area. The Spalart-Allmaras (SA), RNG $k-\varepsilon$, and Realisable $k-\varepsilon$ (RKE) were all very closely related in terms of numerical predictions. Although these models predicted higher velocities and heat transfer rates at transonic conditions, they correlated very well with experimental results at the leading edge.

The investigated 2-D model was expanded to 3-D in the hope that secondary flow effects would bring about better correlations to experimental results. Although this was not the case, vital information about the 3-D nature of the flow field was gained. The results of static pressure predictions over the profile remained unchanged when compared to the 2-D model and this was deduced by its symmetrical distribution. The heat transfer distribution on the pressure surface also remained unaffected. This was in full agreement with Graziani et al (1980), who states that the blade pressure surface heat transfer is not affected by secondary flows. The reason for its unchanged distribution was owed to the suction surface increasing in heat transfer. This was attributed to the secondary flow formation of two horseshoe vortices at the leading edge of which one reflects from the pressure surface onto the suction surface enhancing heat transfer rates in that region.

In general however, numerical predictions represent the ideal case and do not account for discrepancies in the actual case. Experimental error was therefore seen as a critical factor for the deviation in numerical correlations. Although the general trend of data in the experimental static pressure distribution was within acceptable limits, the heat transfer section would require more investment. In order to reduce the heat transfer variations the entire experimental methodology would have to be redone to bring about decisive results.

CHAPTER 8

CONCLUSIONS AND RECOMMENDATIONS

The project commenced with the objective of achieving experimental static pressures and heat transfer coefficients over a film-cooled turbine test blade. The many issues surrounding its implementation into the supersonic cascade facility were addressed by conducting a feasibility study. In conducting the study an experimental test blade profile was selected on the basis of having well documented results, with and without film-cooling effects. This was the profile used by Consigny and Richards (1982) as well as Camci and Arts (1985a, 1985b, 1990). The concept gas turbine rotor blade was then used as a basis for the design of a new cascade. The cascade was designed by simulating various 2-D blade arrangements using the CFD package, FLUENT. Once the layout of the cascade had been finalised with CFD verification, the test blade profile was expanded to include for film-cooling effects. The locations and arrangement of the discrete film cooling holes were then also investigated using CFD as a guideline. An effective means of cooling was then attained by the simultaneous ejection of coolant from two rows located at the leading edge and a single row of holes on the pressure surface. The conceptual film-cooled test blade was then used to design two experimental test blades, one for obtaining static pressures and the other for isothermal heat transfer coefficients. The experimental test blades were designed around the existing technology used by the SMR-95 profile. This was done to save on aspects like time and money as there was already an existing data acquisition system and transient measurement technique. A proposed 4-blade cascade with two interchangeable film-cooled experimental test blades was then generated. However, in order to make film-cooling a reality, aspects such as coolant supply to the test blades was required from the experimental facility. This brought about a proposed modification to the existing blower supply line which was previously used by the experimental heat transfer investigations to pre-chill the Macor test section upon its transient measurement.

Although a means of implementing film-cooling in the supersonic cascade facility has been generated, its implementation held with it the fundamental requirements that the experimental facility and data acquisition system be operational, of which neither commodity was available at the time. The added limitations of time and money had also caused the foreclosure of the film-cooling project. The objectives were then shifted into repairing and upgrading the experimental facility and data acquisition systems. This was then to be followed by improving on the quality

of experimental data sets over the existing SMR-95 blade profile. The experimental results were then to be used for numerical validation and model development.

The experimental facility was refurbished into a state capable of producing the required operating test conditions. Numerous aspects were addressed into the facilities refurbishment and one of note deals with the carbon seal located on the compressor shaft. The seal had to be removed and relapped to suit the newly ground shaft. The carbon seal which had been eaten away by a corrosive build on the compressor shaft prevented the required vacuum levels of being attained. This problem had resulted on numerous occasions in the past and in order to avoid its reoccurrence, it is recommended that it be replaced by a labyrinth seal. Another recommendation is that the Uchida swash-plate pump which powers up the hydraulic motor be replaced with an electric drive. This pump is highly inefficient and speed control is difficult to maintain. An electric drive would offer the user more flexibility during experimental testing and eliminate the errors experienced when attaining repeatable flow conditions.

Static pressure distributions were then generated using two pressure transducers and the results of which, were then compared to previous researchers for validation purposes. The outcome reveled inconsistencies on the suction side with the results presented by de Villiers (2002). The lower predictions of static pressures on the blade suction side made by de Villiers were justified by his use of only one pressure transducer. The use of one transducer resulted in two experimental data measurements, one on the pressure side and suction side respectively. Analysis of the raw data files revealed an increased compressor rpm on the suction side which would result in lower static pressure predictions.

In order to produce the corresponding heat transfer measurements, a badly damaged heat transfer blade stack with numerous amounts of broken sensors brought about the re-instrumentation of the Macor test section. The Macor substrate was re-instrumented with platinum thin film gauges of increased sensitivity. Calibration of the new gauges revealed marginal increases in sensitivity and modifications to the heat transfer analogue were not necessitated. The heat transfer investigations did produce a consistent distribution with all the heat flux sensors working however there was a large degree of experimental error present. These errors were a result of the electrical noise pick from the rig, general operation of the electrical analogue and difficulties in attaining repeatable flow conditions. A way to overcome these obstacles includes scrapping the integrative nature of the electrical analogue system and replacing it with a numerical algorithm using LABview software. The numerical technique developed by Cook (1970) and Cook and Felderman (1966) would allow the simultaneous measurement of all the sensors however, this procedure is a differential process and would

generate more noise. One would then have to look at reducing the noise pick up from the experimental facility. If this is not possible Snedden (1995) proposed numerous modifications in his dissertation on how to improve on the electrical analogue system. The simultaneous data capturing of all the sensors would then eliminate the need for repeatable flow conditions and reduce experimental error significantly.

The measured experimental data was then compared to the numerical predictions of FLUENT. The use of various grid structures and different turbulence models were investigated to bring about a better understanding of the flow field within the cascade. Initially a 2-D model was used for the comparisons. Two separate meshing strategies i.e. a refined pave mesh and decomposed structured mesh were investigated for different turbulence models. The results revealed that the choice of turbulence model was more important than the grid implemented. Investigations of the different turbulence models displayed the SST $k - \omega$ model's superiority in predicting wall bounded flows and transonic conditions. The model however significantly lacked in areas were large flow separation was encountered. These areas included the blade's leading edge, and the Spalart-Allmaras (SA), RNG $k - \varepsilon$, and Realisable $k - \varepsilon$ (RKE) turbulence models, which were all very similar in numerical predictions, produced much better experimental correlations. The 2-D model was then expanded into a 3-D model to include for secondary flow effects and investigate their effects on heat transfer. The corresponding outcome of the 3-D model revealed no changes in its static pressure distribution. This was justified by its symmetrical distribution of pressures in the blade's spanwise direction. The heat transfer results on the blades pressure surface also remained unaltered but the results on the suction surface did increase. The increased heat transfer rates on the suction surface were owed to the interaction of horseshoe vortices. These vortices which were experimentally noted by Graziani et al (1980), to bring about increased heat transfer rates on the suction surface and leave the pressure surface heat transfer rates unchanged further validated the three dimensional capabilities of FLUENT. The numerical predictions of heat transfer however illustrated the need for the experimental results of heat transfer to be improved. This would be facilitated by redesigning its corresponding data acquisition systems thus reducing on experimental errors and allowing concise conclusions to be drawn from its numerical models.

APPENDIX A

Blade co-ordinates

A 1.1 SMR-95 Blade co-ordinates

Table A1-1: SMR-95 blade profile co-ordinates

Suction Surface		
	X Co-ordinate (mm)	Y Co-ordinate (mm)
1	9.383	2
2	9.262	2.003
3	9.136	2.009
4	9	2.019
5	8.859	2.033
6	8.717	2.051
7	8.583	2.072
8	8.454	2.095
9	8.334	2.12
10	8.216	2.146
11	8.094	2.177
12	7.964	2.213
13	7.827	2.255
14	7.69	2.301
15	7.561	2.348
16	7.44	2.396
17	7.327	2.443
18	7.217	2.492
19	7.102	2.546
20	6.981	2.607
21	6.854	2.675
22	6.724	2.749
23	6.604	2.822
24	6.497	2.89
25	6.397	2.957
26	6.299	3.026
27	6.192	3.105
28	6.085	3.188
29	5.971	3.282
30	5.86	3.378
31	5.756	3.474
32	5.664	3.564
33	5.58	3.649
34	5.499	3.737
35	5.411	3.836
36	5.318	3.947
37	5.228	4.061

Pressure Surface		
	X Co-ordinate (mm)	Y Co-ordinate (mm)
235	97.861	31.162
236	97.77	30.997
237	97.655	30.864
238	97.518	30.764
239	97.361	30.699
240	97.186	30.669
241	96.995	30.675
242	94.849	31.137
243	92.7	31.587
244	90.548	32.026
245	88.395	32.456
246	86.24	32.876
247	84.082	33.278
248	83.6	33.364
249	83.112	33.45
250	82.549	33.547
251	81.918	33.653
252	81.328	33.751
253	80.804	33.836
254	80.263	33.922
255	79.75	34.002
256	79.24	34.08
257	78.711	34.159
258	78.163	34.24
259	77.579	34.324
260	76.998	34.406
261	76.434	34.484
262	75.909	34.555
263	75.403	34.621
264	74.895	34.686
265	74.372	34.751
266	73.782	34.823
267	73.224	34.889
268	72.708	34.949
269	72.18	35.008
270	71.602	35.072
271	71.042	35.132

38	5.142	4.177
39	5.068	4.283
40	4.999	4.388
41	4.937	2.486
42	4.871	4.596
43	4.807	4.709
44	4.745	4.824
45	4.678	4.955
46	4.629	5.057
47	4.558	5.215
48	4.481	5.399
49	4.435	5.523
50	4.403	5.624
51	4.387	5.685
52	4.362	5.792
53	4.34	5.889
54	4.279	6.167
55	4.264	6.237
56	4.25	6.302
57	4.218	6.451
58	4.21	6.488
59	4.16	6.726
60	4.072	7.173
61	4.003	7.583
62	3.958	7.924
63	3.932	8.197
64	3.909	8.517
65	3.891	8.77
66	3.86	9.224
67	3.829	9.677
68	3.761	10.563
69	3.693	11.449
70	3.634	12.238
71	3.596	12.745
72	3.574	13.077
73	3.537	13.8
74	3.501	14.682
75	3.469	15.819
76	3.453	16.607
77	3.445	17.268
78	3.441	18.056
79	3.446	18.896
80	3.457	16.552
81	3.477	20.32
82	3.507	21.099
83	3.553	21.972
84	3.6	22.695
85	3.659	23.442
86	3.732	24.224
87	3.821	25.037
88	3.911	25.764

272	70.605	35.177
273	70.053	35.233
274	69.484	35.289
275	68.857	35.348
276	68.401	35.389
277	67.858	35.435
278	67.266	35.483
279	66.668	35.528
280	66.251	35.557
281	65.761	35.589
282	65.1	35.628
283	64.477	35.661
284	64.143	35.677
285	63.659	35.697
286	63.233	35.713
287	62.283	35.742
288	61.192	35.766
289	60.066	35.775
290	58.941	35.768
291	57.891	35.748
292	56.984	35.722
293	56.566	35.708
294	56.027	35.687
295	55.697	35.672
296	55.2	35.647
297	54.564	35.612
298	54.027	35.58
299	53.505	35.546
300	53.05	35.513
301	52.463	35.467
302	51.918	35.421
303	51.317	35.364
304	50.829	35.314
305	50.3	35.254
306	49.743	35.186
307	49.136	35.106
308	48.59	35.028
309	48.071	34.95
310	47.528	34.862
311	46.967	34.766
312	46.41	34.665
313	45.872	34.562
314	45.334	34.454
315	44.812	34.344
316	44.282	34.227
317	43.755	34.105
318	43.196	33.971
319	42.675	33.841
320	42.19	33.715
321	41.672	33.576
322	41.12	33.424

89	4.011	26.486
90	4.133	27.291
91	4.266	28.081
92	4.392	28.773
93	4.536	29.506
94	4.7	30.285
95	4.883	31.097
96	5.045	31.764
97	5.24	32.518
98	5.447	33.263
99	5.687	34.066
100	5.9	34.731
101	6.143	35.441
102	6.415	36.181
103	6.723	36.965
104	4.012	37.655
105	7.312	38.332
106	7.647	39.045
107	8.005	39.764
108	8.351	40.422
109	8.717	41.082
110	9.11	41.756
111	9.529	42.436
112	9.931	43.056
113	10.362	43.689
114	10.811	44.315
115	11.296	44.957
116	11.767	45.549
117	12.259	46.136
118	12.769	46.713
119	13.307	47.29
120	13.846	47.838
121	14.391	48.365
122	14.962	48.888
123	15.548	49.395
124	16.754	50.368
125	17.37	50.827
126	17.994	51.267
127	18.637	51.697
128	19.291	52.11
129	19.94	52.497
130	20.618	52.88
131	21.333	53.26
132	22.034	53.608
133	22.709	53.923
134	23.388	54.218
135	24.149	54.527
136	24.871	54.798
137	25.599	55.051
138	26.281	55.272
139	27.079	55.511
140	27.827	55.718

323	40.556	33.262
324	40.09	33.124
325	39.553	32.959
326	39.029	32.792
327	38.461	32.604
328	37.998	32.445
329	37.491	32.262
330	36.967	32.066
331	36.401	31.845
332	35.906	31.644
333	35.421	31.439
334	34.911	31.214
335	34.385	30.974
336	33.89	30.74
337	33.406	30.501
338	32.913	30.251
339	32.421	29.991
340	31.947	29.732
341	31.473	29.464
342	30.995	29.185
343	30.517	28.897
344	30.059	28.611
345	29.599	28.315
346	29.139	28.009
347	28.68	27.694
348	28.244	27.385
349	27.803	27.062
350	27.361	26.729
351	26.918	26.383
352	26.5	26.046
353	26.08	25.698
354	25.66	25.338
355	25.24	24.966
356	24.844	24.604
357	24.448	24.23
358	24.054	23.846
359	23.656	23.445
360	23.277	23.05
361	22.904	22.649
362	22.539	22.243
363	22.175	21.823
364	21.82	21.399
365	21.476	20.975
366	21.138	20.543
367	20.807	20.105
368	20.476	19.652
369	20.161	19.204
370	19.853	18.752
371	19.556	18.3
372	19.255	17.825
373	18.966	17.353
374	18.688	16.883

141	28.569	55.908
142	29.254	56.07
143	30.042	56.241
144	30.827	56.396
145	31.56	56.542
146	33.064	56.754
147	33.852	56.85
148	34.583	56.926
149	35.335	56.991
150	36.194	57.05
151	36.982	57.088
152	37.732	57.111
153	38.41	57.12
154	39.254	57.118
155	40.023	57.104
156	40.813	57.08
157	41.485	57.051
158	42.33	57.005
159	43.135	56.951
160	43.872	56.886
161	45.333	56.76
162	46.149	56.671
163	46.871	56.584
164	47.612	56.487
165	48.426	56.371
166	49.203	56.25
167	49.935	56.127
168	50.65	55.999
169	51.521	55.834
170	52.283	55.681
171	53.037	55.522
172	53.665	55.384
173	54.504	55.193
174	55.272	55.011
175	56.026	54.828
176	56.658	54.671
177	57.45	54.469
178	58.253	54.258
179	58.959	54.069
180	59.632	53.885
181	60.359	53.681
182	61.132	53.459
183	61.843	53.249
184	62.587	53.025
185	63.386	52.779
186	64.13	52.544
187	64.837	52.315
188	65.518	52.091
189	66.334	51.817
190	67.065	51.566
191	67.798	51.31
192	68.426	51.088

375	18.424	16.419
376	18.158	15.934
377	17.9	15.447
378	17.652	14.958
379	17.412	14.469
380	17.173	13.962
381	16.944	13.457
382	16.714	12.926
383	16.521	12.462
384	15.754	10.405
385	15.11	8.305
386	14.891	7.231
387	14.741	6.648
388	14.592	6.171
389	14.406	5.626
390	14.238	5.155
391	14.21	5.086
392	14.161	4.98
393	14.092	4.845
394	13.985	4.659
395	13.896	4.512
396	13.845	4.431
397	13.779	4.331
398	13.715	4.238
399	13.64	4.133
400	13.551	4.017
401	13.465	3.909
402	13.379	3.807
403	13.298	3.715
404	13.214	3.625
405	13.129	3.537
406	13.053	3.444
407	12.937	3.353
408	12.833	3.26
409	12.723	3.168
410	12.617	3.084
411	12.517	3.009
412	12.42	2.939
413	12.32	2.871
414	12.207	2.798
415	12.087	2.724
416	11.958	2.65
417	11.827	2.58
418	11.704	2.518
419	11.59	2.464
420	11.481	2.417
421	11.37	2.371
422	11.244	2.322
423	11.108	2.274
424	10.964	2.227
425	10.821	2.185
426	10.687	2.15

193	69.227	50.8
194	69.969	50.53
195	70.693	50.263
196	71.316	50.031
197	72.05	49.755
198	72.813	49.464
199	73.513	49.194
200	74.189	48.931
201	74.876	48.661
202	75.612	48.367
203	76.308	48.087
204	77.045	47.787
205	77.787	47.481
206	78.505	47.182
207	79.176	46.898
208	79.882	46.597
209	80.694	46.247
210	81.408	45.934
211	82.095	45.631
212	82.7	45.361
213	83.512	44.995
214	84.221	44.673
215	84.947	44.341
216	85.5	44.087
217	86.273	43.729
218	87.013	43.385
219	87.693	43.067
220	88.289	42.787
221	88.981	42.461
222	89.745	42.098
223	90.403	41.784
224	91.067	41.466
225	93.834	40.12
226	96.589	38.75
227	99.332	37.358
228	99.483	37.244
229	99.599	37.112
230	99.68	36.964
231	99.724	36.802
232	99.731	36.628
233	99.699	36.444
234	98.78	33.803

427	10.559	2.12
428	10.442	2.096
429	10.323	2.074
430	10.196	2.054
431	10.058	2.036
432	9.913	2.021
433	9.771	2.01
434	9.636	2.003
435	9.506	2

A 1.2 Consigny and Richards (1982), Rotor Blade co-ordinates

Table A1-2: Consigny and Richards (1982) blade profile co-ordinates

X co-ordinate	Y co-ordinate
1.414	2.059
0	8.588
0.353	13.294
1.882	18.588
5.882	25.035
10.588	28.741
17.647	31.824
24.118	33.271
31.176	33.458
38.235	32.647
45.296	31
52.353	28.647
61.176	25.094
71.765	20.024
82.353	14.318
92.941	7.965
96.471	5.647
98.824	4.059
100	2.118
99.765	1.059
97.941	0
94.118	1.518
89.412	3.576
82.353	6.412
75.294	8.918
68.235	11.094
61.176	12.941
54.118	14.447
47.059	15.565
40	16.012
32.941	15.647
25.882	14.129
20.588	12.035
17.647	10.506
15.294	8.976
12.941	6.871
9.412	2.682
5.059	0
1.414	2.059

APPENDIX B

Calibration Procedures and Results

B 1.1 Rosemount Differential Pressure Transducer Calibration Procedure

1. Set the Range of the Rosemount to 0.4 bar

a. Apply zero differential pressure across the Rosemount by leaving both the HP and LP lines of the transducer open to atmosphere.

b. Adjust the zero calibration screw until an output of 1.88V was achieved, this should correspond to the lowest 4mA output of the transducer.

c. Apply a pressure of 0.6 bar to the LP side of the Rosemount, thus providing a differential pressure of 0.4 bar.

d. Adjust the span calibration screw until a maximum of 9.4 V is read by the voltmeter which corresponds to highest 20mA .

e. Repeat the process until the correct voltage range corresponds to the pressure range. (Note. It is vital to repeat the process as adjusting the span screw affects the zero setting)

2. Plot the calibration curves of the Rosemount

a. Leave the HP side of the Rosemount open to atmosphere and attach the LP side to the total inlet pressure.

b. Attach the total pressure to a U-tube manometer.

c. Start the vacuum pump.

d. Once the vacuum pump is started activate a stopwatch noting the height of the mercury every 20 s for 200 s.

e. Simultaneously once the vacuum pump is started, capture the output signal which corresponds to the differential pressure, through channels 0 and 1 on the PC 30 U card with Waveview software. (Note. The software records the change in voltage signal against time)

f. Once the sampling is complete, export the data to a text file and extract the voltage signals corresponding to the 20 s time intervals.

g. Convert the height measurements into pressures using $\Delta P = \rho gh$ where, ρ = density of mercury as 13600 kg/m^3, g = gravity taken as 9.81m/s^2, and h is the difference in height of the mercury in the tubes.

h. Construct a straight line graph of differential pressure vs voltage using the gradient and y intercept as calibration constants to be inputted into the sub VI of the LABview program called "pressure measurement".

Table B-1: Rosemount transducer calibration data template (Atmospheric pressure taken as 101325 Pa)

Time (s)	Manometer Height (m)	Differential Pressure (Pa)	Plenum Pressure (Pa)	RMA (V)
0				
20				
40				
60				
80				
100				
120				
140				
160				
180				
200				

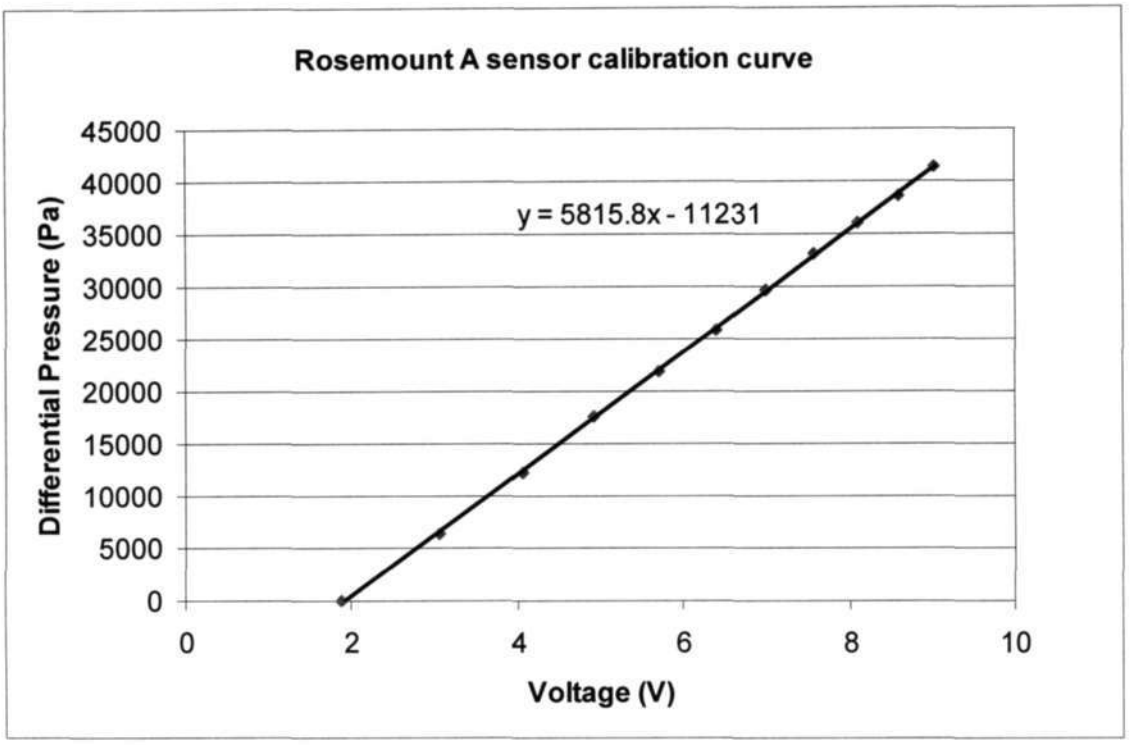

Figure B-1 Rosemount A calibration curve and constants

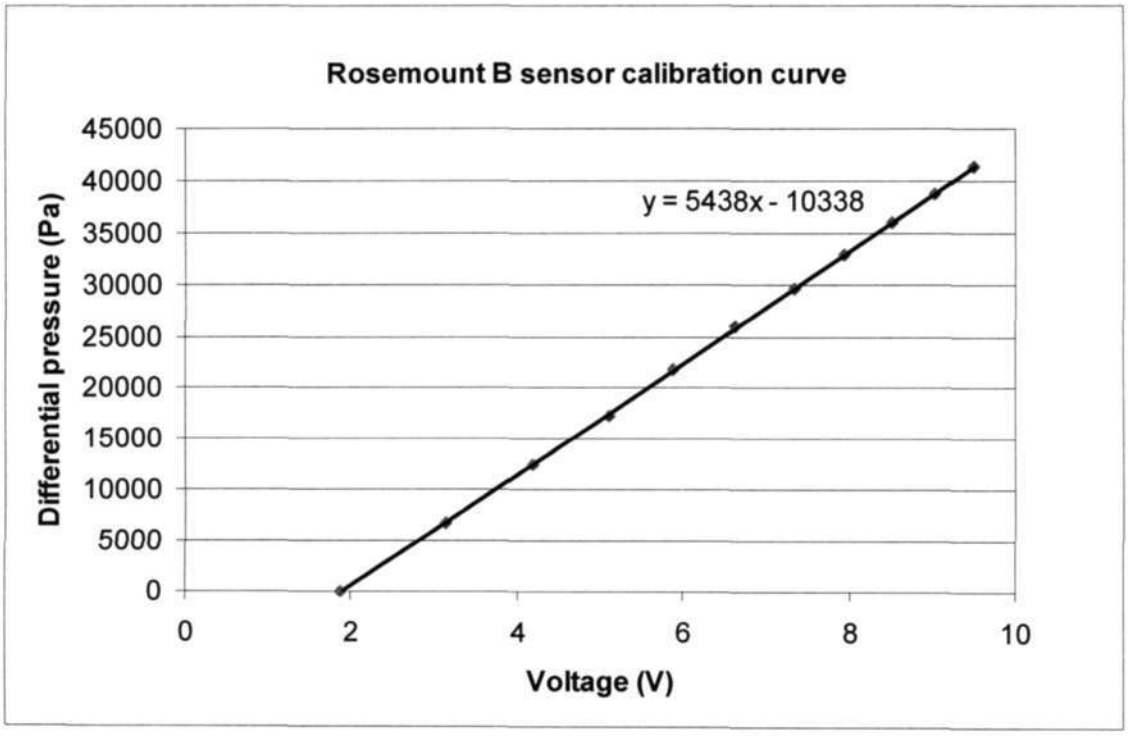

Figure B-2 Rosemount B calibration curve and constants

B 1.2 Kulite Total Pressure Transducer Calibration Procedure

1. Plot the calibration curves of the Kulite Pressure Transducer

a. Attach the total plenum pressure to a U-tube manometer.

b. Start the vacuum pump.

c. Once the vacuum pump is started activate a stopwatch noting the height of the mercury every 10 s for 240 s.

d. Simultaneously once the vacuum pump is started, capture the output signal which corresponds to the total pressure of the Kulite, through channel 3 on the PC 30 U card with Waveview software. (Note. The software records the change in voltage signal against time)

e. Once the sampling is complete, export the data to a text file and extract the voltage signals corresponding to the 20 s time intervals.

f. Convert the height measurements into pressures using $\Delta P = \rho gh$ where, ρ = density of mercury as 13600 kg/m^3, g = gravity taken as 9.81 m/s^2, and h is the difference in height of the mercury in the tubes.

g. Construct a straight line graph of total pressure vs voltage using the gradient and y intercept as calibration constants to be inputted into the sub VI of the LABview program called "pressure measurement".

Table B-2: Kulite transducer calibration data template (Atmospheric pressure taken as 101325 Pa)

Time (s)	Manometer Height (m)	Differential Pressure (Pa)	Plenum Pressure (Pa)	Kulite (V)
0				
10				
20				
30				
40				
50				
60				
70				
80				
90				
100				
110				
120				
130				
140				
150				
160				
180				
200				
220				
240				

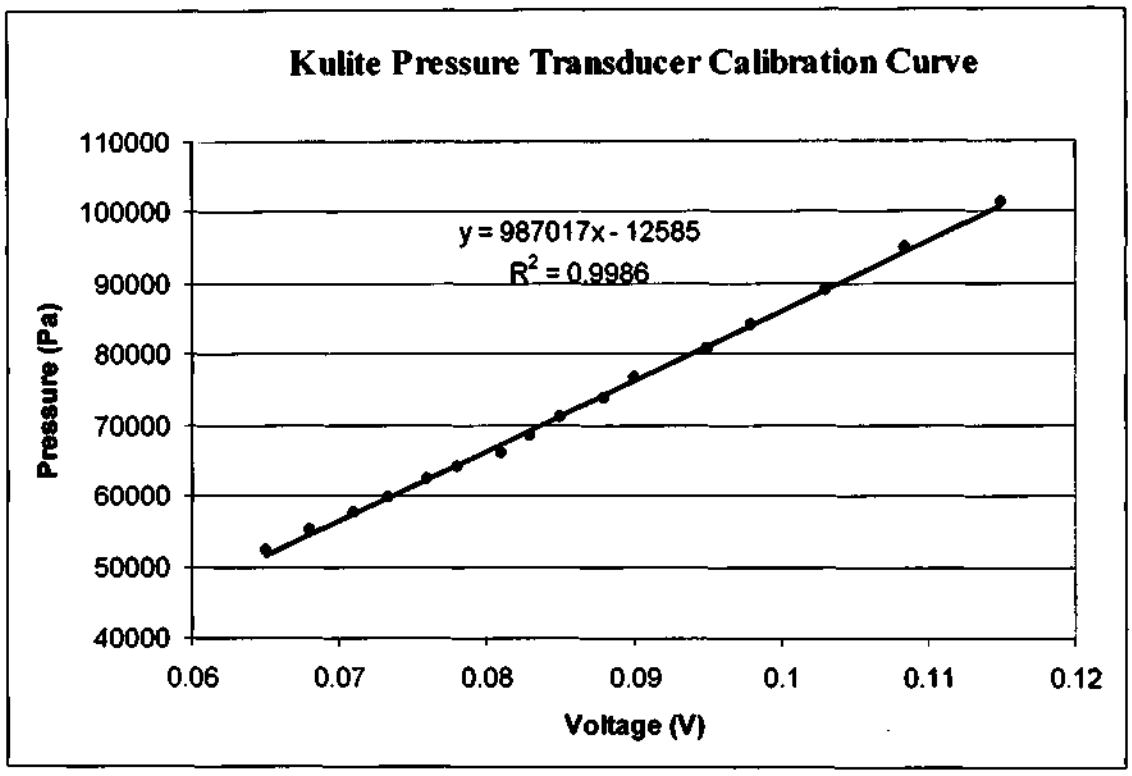

Figure B-3 Kulite calibration curve and constants

B 2.1 Thin Film Gauge Calibration

1. Experimental Setup and Procedure

a. Place the heat transfer blade stack on ceramic blocks within an industrial convection oven.
b. Instrument the blade with thermocouples at the front, top and rear section of the profile.
c. Run the sensor plugs to the heat transfer analogue (Note. The heat transfer analogue remains unplugged for the duration of the calibration)
d. Connect the outputs of the selector box to a multimeter to read out resistance.
e. Run the wiring of the heat transfer blade stack through the linings of the door and switch on the oven.
f. Record the measurements of all the thermocouples as well as the oven display and average for the final temperature.
g. Record the resistances of all the corresponding sensors by changing the plugs and switching the selector box. (Note. This provides for fast and effective calibration of the entire system for all the sensors)

h. Increase the temperature of the oven by approximately 20 ^{0}C and repeat steps f – g up to 100 ^{0}C.

i. Input the data into the Excel spreadsheet "sensorcalibration" to calculate the respective calibration constants i.e. α_R and R_0.

Presented below are the calibration data and plots for the re-instrumented blade stack:

Table B-3: Calibration data for Plug 1

Plug 1		Pins	1&2	3&4	5&6	7&8	9&10	11&12	14&15	16&17
Tave[C]	Kelvin	Sensor No.	1	2	3	4	5	6	7	8
24.175	297.175		141.86	52.38	65.41	62.27	49.51	54.62	52.61	51.29
39.875	312.875		143.89	53.1	66.32	63.21	50.23	55.39	53.41	51.95
59.925	332.925		145.75	53.79	67.19	64.06	51.15	56.07	54.07	52.56
80.125	353.125		149	55	68.69	65.58	51.94	57.38	55.23	53.75
100.15	373.15		151.85	56.06	70.04	66.92	52.92	58.45	56.25	54.78
		Gradient	0.1308	0.0483	0.0606	0.0608	0.0444	0.0503	0.0474	0.0458
		Y-Intercept	138.5100	51.1280	63.8410	60.7070	48.4500	53.3210	51.4300	50.0790
		To (40 degrees C)	40							
		Ro	143.742	53.06	66.265	63.139	50.226	55.333	53.326	51.911
		alphaR	9.100E-04	9.103E-04	9.145E-04	9.630E-04	8.840E-04	9.090E-04	8.889E-04	8.823E-04

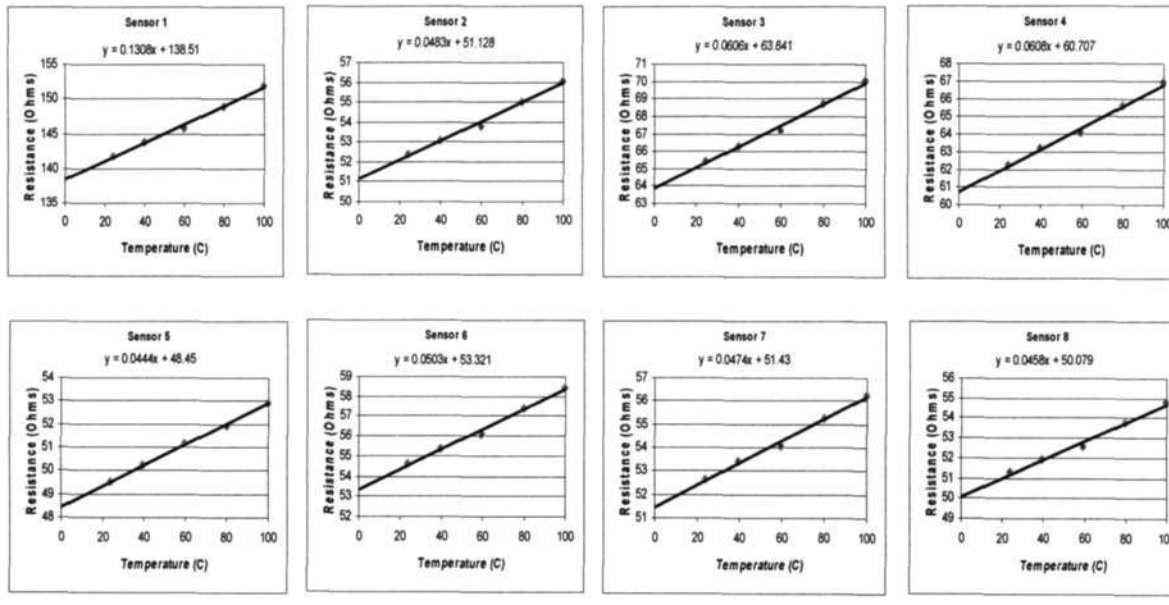

Figure B-4 Calibration plots for Plug 1

Table B-4: Calibration data for Plug 2

Plug 2		Pins	1&2	3&4	5&6	7&8	9&10	11&12	14&15	16&17
Tave[C]	Kelvin	Sensor No.	1	2	3	4	5	6	7	8
24	297		52.19	53.09	54.44	51.23	51.05	52.29	48.2	131.05
39.825	312.825		52.87	53.8	55.15	51.93	51.75	53	49.21	133.06
59.95	332.95		53.5	54.47	55.82	52.59	52.4	53.73	49.6	134.97
80.05	353.05		54.71	55.7	57.01	53.77	53.57	54.94	50.63	138.07
100.025	373.025		55.75	56.78	58.04	54.76	54.6	55.99	51.67	140.79
		Gradient	0.0467	0.0484	0.0472	0.0464	0.0465	0.0487	0.0434	0.1275
		Y-Intercept	50.9650	51.8290	53.2230	50.0380	49.8490	51.0320	47.2240	127.8400
		To (40 degrees C)	40							
		Ro	52.833	53.765	55.111	51.894	51.709	52.98	48.96	132.94
		alphaR	8.839E-04	9.002E-04	8.565E-04	8.941E-04	8.993E-04	9.192E-04	8.864E-04	9.591E-04

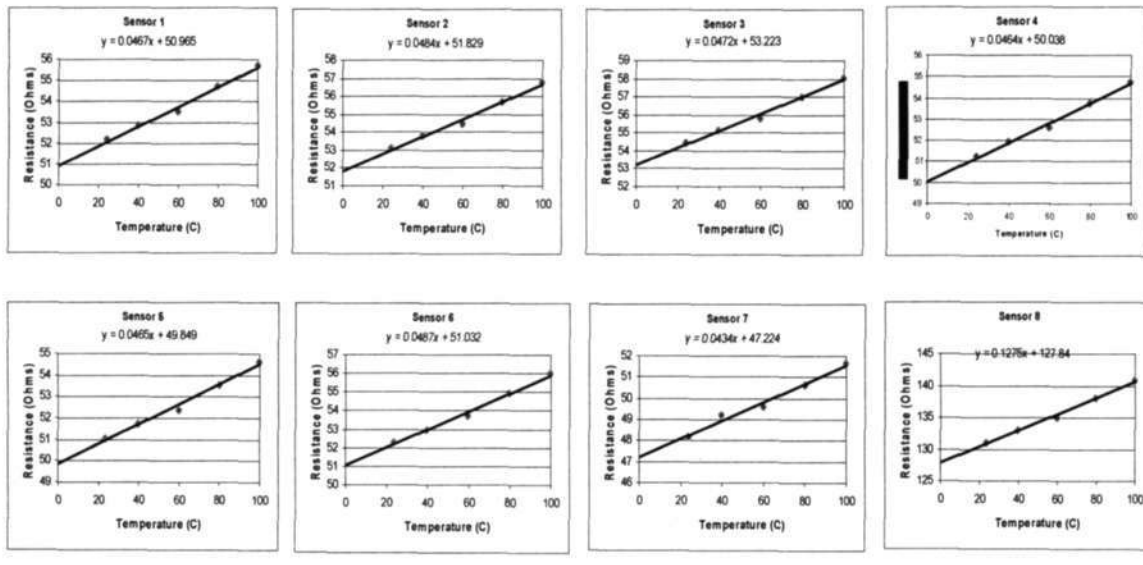

Figure B-5 Calibration plots for Plug 2

Table B-5: Calibration data for Plug 3

Plug 3		Pins	1&2	3&4	5&6	7&8	9&10	11&12	14&15	16&17
Tave[C]	Kelvin	Sensor No.	1	2	3	4	5	6	7	8
23.95	296.95		51.56	51.12	51.44	50.62	50.86	51.37	69.87	121.37
39.95	312.95		52.33	51.84	52.18	51.36	51.55	52.13	71	123.2
59.925	332.925		53.05	52.54	52.9	52.07	52.34	52.87	72.1	125.22
80.025	353.025		54.2	53.72	54.07	53.23	53.45	54.08	73.89	127.76
100.1	373.1		55.21	54.71	55.07	54.21	54.43	55.07	74.96	130.14
		Gradient	0.0477	0.0472	0.0476	0.0471	0.0471	0.0487	0.0680	0.1150
		Y-Intercept	50.3690	49.9180	50.2360	49.4340	49.6650	50.1450	68.2330	118.5500
		To (40 degrees C)	40							
		Ro	52.277	51.806	52.14	51.318	51.549	52.093	70.953	123.15
		alphaR	9.124E-04	9.111E-04	9.129E-04	9.178E-04	9.137E-04	9.349E-04	9.584E-04	9.338E-04

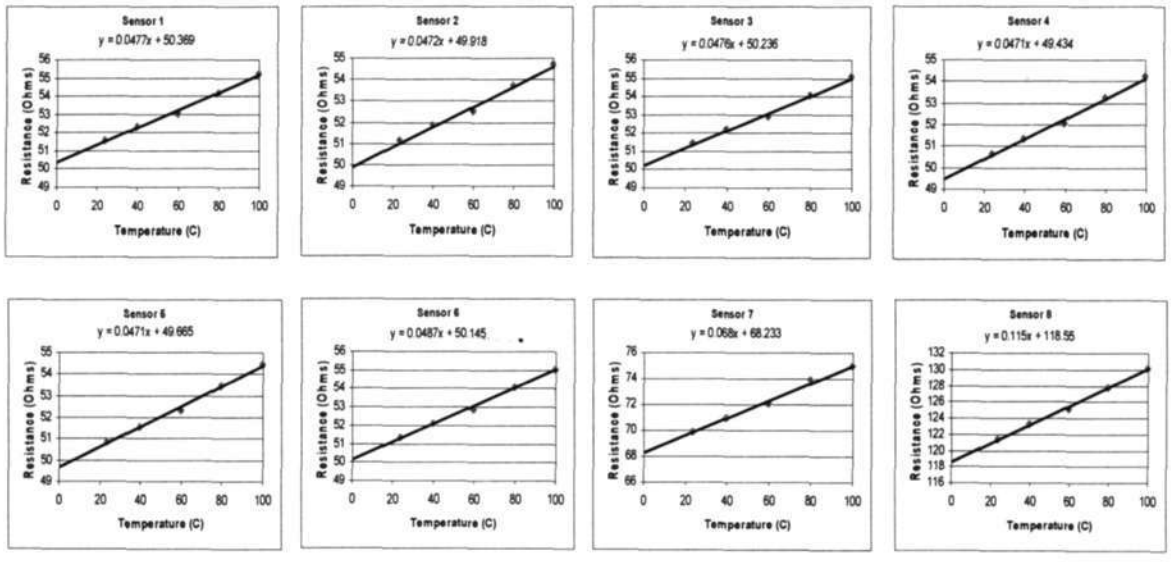

Figure B-6 Calibration plots for Plug 3

Table B-6: Calibration data for Plug 4

Plug 4		Pins	1&2	3&4	5&6	7&8	9&10	11&12	14&15	16&17
Tave[C]	Kelvin	Sensor No.	1	2	3	4	5	6	7	8
24.075	297.075		52.15	52.12	63.97	57.95	52.13	51.42	63.97	60.27
39.825	312.825		52.85	52.82	64.94	58.76	52.91	52.17	64.94	61.16
59.825	332.825		53.69	53.66	66.08	59.74	53.88	53.09	66.08	62.15
79.75	352.75		54.73	54.69	67.4	60.87	54.94	54.16	67.4	63.38
100.025	373.025		55.68	55.65	68.62	61.92	56.02	55.12	68.62	64.52
		Gradient	0.0466	0.0466	0.0613	0.0524	0.0512	0.0490	0.0613	0.0559
		Y-Intercept	50.9880	50.9600	62.4800	56.6660	50.8700	50.2190	62.4800	58.9020
		To (40 degrees C)	40							
		Ro	52.852	52.824	64.932	58.762	52.918	52.179	64.932	61.138
		alphaR	8.817E-04	8.822E-04	9.441E-04	8.917E-04	9.675E-04	9.391E-04	9.441E-04	9.143E-04

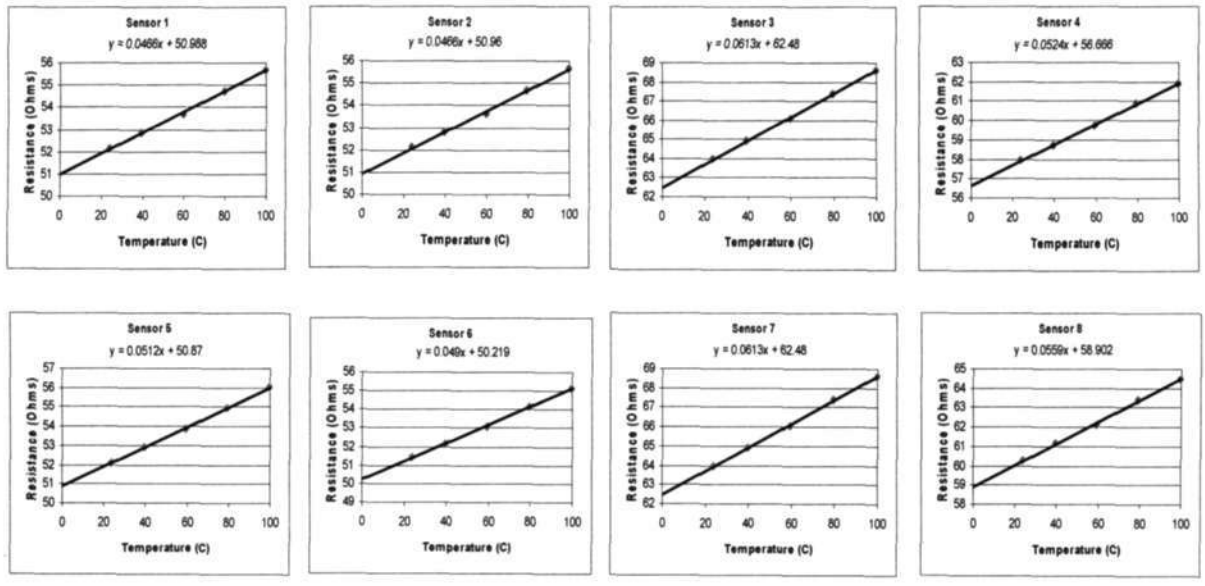

Figure B-7 Calibration plots for Plug 4

Table B-7: Calibration data for Plug 5

Plug 5		Pins	1&2	3&4	5&6	7&8	9&10	11&12	14&15	16&17
Tave[C]	Kelvin	Sensor No.	1	2	3	4	5	6	7	8
23.9	296.9		59.62	54.61	70.02	66.04	52.19	54.03	51.74	52.53
39.925	312.925		60.52	55.43	71.12	67.04	52.7	54.89	52.74	53.33
59.975	332.975		61.55	56.36	72.31	68.15	53.44	55.79	53.43	54.21
79.95	352.95		62.82	57.56	73.86	69.63	54.56	57.01	54.56	55.39
99.85	372.85		64.02	58.66	75.3	71.01	55.59	58.18	55.51	56.42

Gradient	0.0579	0.0534	0.0693	0.0654	0.0453	0.0543	0.0487	0.0513
Y-Intercept	58.1920	53.2840	68.3110	64.4060	50.9460	52.6800	50.6390	51.2600

To (40 degrees C)	40							
Ro	60.508	55.42	71.083	67.022	52.758	54.852	52.587	53.312

alphaR	9.569E-04	9.636E-04	9.749E-04	9.758E-04	8.586E-04	9.899E-04	9.261E-04	9.623E-04

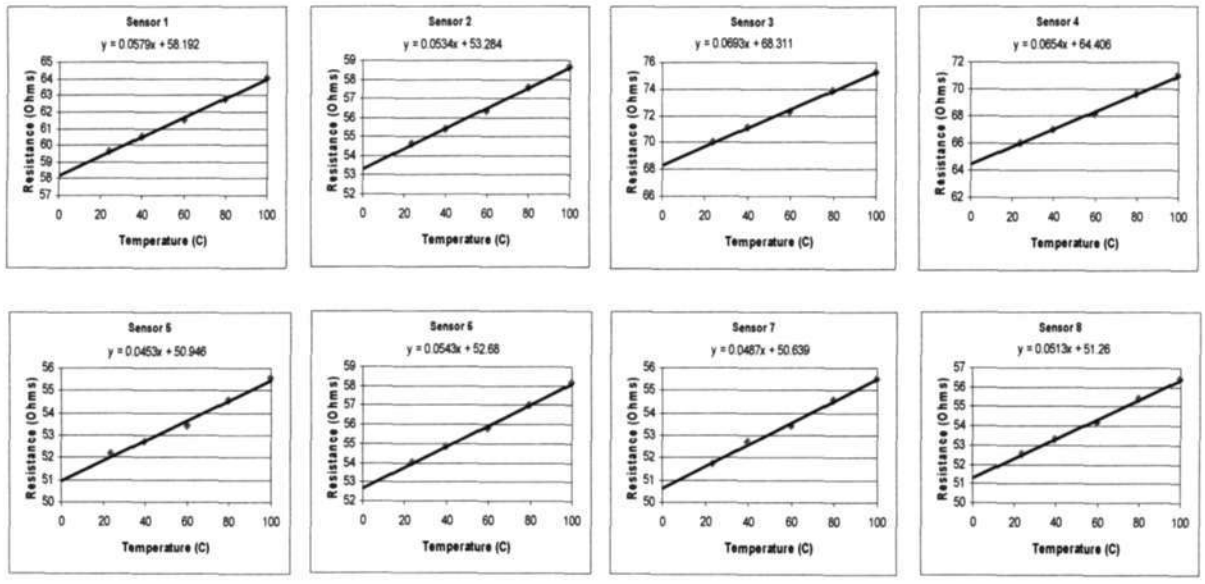

Figure B-8 Calibration plots for Plug 5

Table B-8: Calibration data for Plug 6

		Pins	1&2	3&4	5&6	7&8	9&10	11&12	14&15	16&17
Tave[C]	Kelvin	Sensor No.	1	2	3	4	5	6	7	8
23.75	296.75		51.58	51.03	52.34	63.07	58.34	64.96	51.51	51.98
39.8	312.8		52.41	51.81	53.12	64.05	59.16	66.15	52.72	52.28
59.775	332.775		53.31	52.66	53.98	65.1	60.11	67.57	53.72	53.26
79.925	352.925		54.47	53.74	55.07	66.46	61.35	70.18	55.93	55.33
99.85	372.85		55.59	54.77	56.11	67.66	62.56	73.19	58.21	57.66
		Gradient	0.0525	0.0490	0.0494	0.0603	0.0554	0.1071	0.0867	0.0756
		Y-Intercept	50.2920	49.8340	51.1300	61.6130	56.9490	61.9210	49.1640	49.5180
		To (40 degrees C)	40							
		Ro	52.392	51.794	53.106	64.025	59.165	66.205	52.632	52.542
		alphaR	1.002E-03	9.461E-04	9.302E-04	9.418E-04	9.364E-04	1.618E-03	1.647E-03	1.439E-03

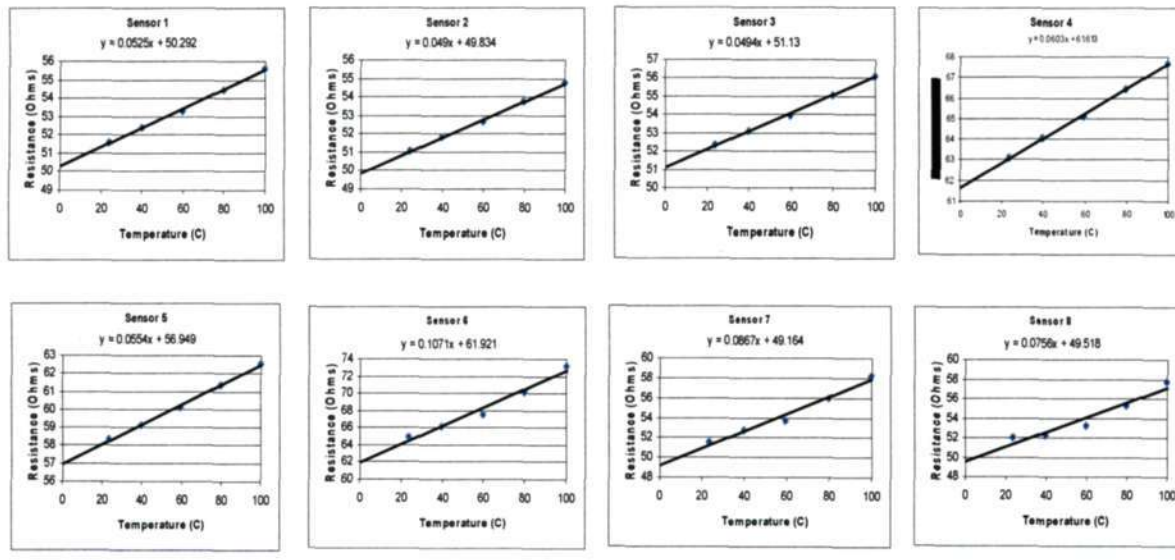

Figure B-9 Calibration plots for Plug 6

B 2.2 Heat Transfer Analogy Calibration

1. Experimental Setup and Procedure

a. Provide a ±15 V supply to the heat transfer analogy and ensure that the blade stack is not connected. (Note. this creates an open circuit to the heat transfer analogy cards)

b. Connect the PC71 interface card to the input of the analogy.

c. Run the calibration program "Cal30". (Note. This program generates a parabolic input to the heat transfer analogy cards and records the output step voltage)

d. Plot the step output voltage in Excel and calculate the step in voltage level.

e. Repeat the calibration process to determine the average circuit calibration constant. (Note. This process is repeated as the signal is very noisy)

f. Turn the switch on the heat transfer analogy housing to the next circuit board to be calibrated and repeat steps a – e.

Table B-9 Circuit calibration results

Circuit	Test 1	Test 2	Average
0	-2.854	-2.893	-2.873
1	-2.784	-2.752	-2.768
2	-2.735	-2.694	-2.714
3	-2.678	-2.673	-2.676
4	-2.628	-2.644	-2.636
5	-2.611	-2.650	-2.631
6	-2.604	-2.628	-2.616
7	-3.102	-3.111	-3.107

APPENDIX C

Experimental Procedures

C 1.1 General Rig Start Up Procedure

1. Turn on the safety control box, display box and pressure control box.
2. Seal the plenum at all locations and start the vacuum pumps excavation.
3. Turn on the main workshop Hydrovane compressor which supplies air to the airpack, used to circulate the gearbox lubrication.
4. Switch on the immersion heater located within the airpack to heat the gear oil to its required operating range of approximately 50-70 °C.
5. Start the air pump. (Note. The oil flow, oil pressure and air pressure interlocks on the safety control box should deactivate and all illuminate green)
6. Check that cooling water is available from the roof mounted reservoir. This is done by turning a stop cock valve on the heat exchanger used to cool the gear oil.
7. At a plenum total pressure of 0.55 bar and gear oil temperature of about 50 °C, the main hydraulic pack may be initiated.
8. Before initiation of the Uchida pump, ensure that the squash plate is in its neutral position, there is an adequate amount of hydraulic motor oil and the hydraulic pump control circuitry is switched to "sonic".
9. Once a fault free system has been displayed on the main power box, the prime pump may be started followed by the Uchida pump.
10. Shut down is initiated in the reverse order.

C 1.2 Experimental Setup and Procedure for Pressure results

1. Setup of the cascade and plenum for pressure measurements.
   a. Insert the pressure measurement test blade within the cascade and bolt it to a plate on the underside, which prevents it from falling through.
   b. Bolt the cascade to the diffuser.
   c. Attach the pressure measurement cover plates to the plenum and connect the silicon tubes to the test blade or exit static pressure tappings in the case of a periodicity study.

d. Connect the silicon tubes at the other end of the cover plates to the respective scanivalve wafers.
e. Connect the Kiel pressure probe which measures the total inlet pressure of the cascade via silicon tubes to the total cascade inlet copper tube.
f. Attach the static inlet and outlet tubes to the corresponding copper tubes.
g. Seal the dished end.

2. Setup of instrumentation for pressure results.
   a. Attach a 24 V power supply to the scanivalve.
   b. Connect both the Rosemount and Kulite pressure transducers to the scanivalve thus ensuring power supplied.
   c. Tubes must also be connected from the common ports on the wafers to the low pressure side of the Rosemount differential pressure transducer.
   d. From the Kulite pressure transducer which measures the total inlet pressure, tubes are connected to the high pressure side of the Rosemount and the balance pressure port of the scanivalve, which is needed to act as a rotor thrust bearing.
   e. The total plenum pressure is also monitored by a U-tube manometer.
   f. The inlet and outlet static pressures are measured using the scanivalve by connecting the pressure tubing to the wafer used on the pressure side of the blade.

3. Setup of the data acquisition system.
   a. Connect the PC 30U card to the PC 30 PGL card located within the computer casing via a D-Type ribbon cable.
   b. Connect gnd and channels Ch0 – 3 of the PC 30U card to the scanivalve.
   c. On the ports of the PC 30U card, connect gnd, A0 – 4 and B0 representing the binary equivalent of the position of the scanivalve and the output voltage used to step the scanivalve.
   d. Start the computer and run the program "Pressure", then select "Winfin" from the VI list.

4. Experimental Rig Operating Procedure for Results
   a. Follow the general start up procedure outlined in Appendix C 1.1 above.
   b. Increase the speed of the pump to 2500 rpm as fast as possible to raise the air temperature of the plenum.
   c. At an air temperature of 90 – 100 °C vary the flow rate of cooling water to the internal radiator to maintain this temperature.

d. When the desired operating conditions are attained, capture the data using the LABview software command "Perform measurement".

C 1.3 Experimental Procedure for Heat Transfer Results

1. Cascade Setup and Instrumentation
   a. Fasten the heat transfer blade stack to the sliding plate on the slider mechanism
   b. Using extreme caution not to scratch any sensors, insert the blade stack through the cascade endwall and fasten the sliding mechanism to the underside of the cascade.
   c. Attach the cooling box and perforated copper plate to the top of the cascade.
   d. Fill the cooling box with insulating foam.
   e. Connect the pneumatic ram through the top of the cooling box lid and screw into the top of the blade.
   f. Fasten the pneumatic ram to the cascade.
   g. Bolt the assembled cascade to the diffuser.
   h. Connect the cooling pipes from the blower to the inlets of the cooling box.
   i. Connect the corresponding compressed air line pipes to the pneumatic cylinder.
   j. Run the heat flux sensor flying leads through one of the specially made cover ports and seal with silicon.
   k. Connect the total inlet, static inlet and static outlet pressure tappings o the respective ports.
   l. Static inlet and outlet pressure tappings are connected in the same manner as the pressure measurement experiments with the output voltages captured using a digital multimeter.
   m. Connect the total inlet temperature thermocouple to the temperature display box.
   n. Connect the internal heat transfer thermocouples to 4 Fluke K/J digital thermometer readouts.

2. Experimental Rig Operating Procedure for Heat Transfer Results
   a. Follow the general start up procedure outlined in appendix C1.1.
   b. Reduce the speed of the compressor to 1000 RPM and open both the radiator water taps for the blade and plenum cooling fully. This results in a drop of the air temperature of the plenum air to assist the instrumented test blade with cooling.

c. Switch off the power supply to the heat transfer analogy and monitor the resistances of the sensors on D-type connectors using the selector box until the value drops to the resistance corresponding to a surface temperature of 40°C , which is required for plunging. This takes ± 30 minutes.
d. Shut off the radiator water supply and increase the compressor speed to 2900 rpm (Max=3000 RPM).
e. When cascade inlet temperature reaches ± 90 °C take speed down to operating conditions i.e. 2500 RPM while trying to maintain 100 °C.
f. Record voltages from the Rosemount pressure transducer for the static inlet and outlet pressures using a multimeter. Record and monitor the total inlet pressure on the display box ensuring a total pressure of 40 Kpa.
g. Record internal blade temperatures.
h. Record initial resistances of all sensors.
i. Turn on the power supply to the heat transfer analogy and record the initial voltages across the inputs of the PC71 interface card.
j. Record down compressor speed and cascade inlet temperature.
k. Start sampling data on Waveview and plunge blade stack.
l. Retract blade stack and return to part b.

Note. 3 experimental templates were used to acquire the relevant data for the generation of isothermal heat transfer coefficients. They are presented in Table C-1, C-2 and C-3, in the following pages.

Table C-1: Experimental template used during heat transfer experimentation

Amb temp before plunge 313 (K) / 40 C							
Plug	Sensor	Circum Pos	Res for 40C	alphaR	Initial Volt	Ini Res	RPM/Inlet temp
P1	1	0.3	143.742	0.000909964			Average Internal Temp =
	2	3.5	53.060	0.00091029			RPM =
	3	6.9	66.265	0.00091451			IN Tot Temp =
	4	13	63.139	0.000962955			IN Stat (V) =
	5	18.1	50.226	0.000884004			OUT Stat (V) =
	6	23.1	55.333	0.000909042			Total Pressure =
	7	28.3	53.326	0.000888872			Notes:
	8	33	51.911	0.000882279			
P2	1	37.8	52.833	0.000883917			Average Internal Temp =
	2	43.1	53.765	0.000900214			RPM =
	3	48.3	55.111	0.000856453			IN Tot Temp =
	4	53.3	51.894	0.00089413			IN Stat (V) =
	5	58.4	51.709	0.000899263			OUT Stat (V) =
	6	64.3	52.980	0.000919215			Total Pressure =
	7	69.4	48.960	0.000886438			Notes:
	8	74.6	132.940	0.000959079			
P3	1	79.5	52.277	0.000912447			Average Internal Temp =
	2	84.5	51.806	0.000911091			RPM =
	3	88.7	52.140	0.000912927			IN Tot Temp =
	4	94.4	51.318	0.000917807			IN Stat (V) =
	5	99.7	51.549	0.000913694			OUT Stat (V) =
	6	105.4	52.093	0.000934866			Total Pressure =
	7	110.5	70.953	0.000958381			Notes:
	8	115.4	123.150	0.000933821			
P4	1	121	52.852	0.000881707			Average Internal Temp =
	2	126.6	52.824	0.000882175			RPM =
	3	131.5	64.932	0.000944065			IN Tot Temp =
	4	136.5	58.762	0.000891733			IN Stat (V) =
	5	107	52.918	0.000967535			OUT Stat (V) =
	6	98.2	52.179	0.000939075			Total Pressure =
	7	92.8	64.932	0.000944065			Notes:
	8	87.6	61.138	0.000914325			
P5	1	81.9	60.508	0.000956898			Average Internal Temp =
	2	76.2	55.420	0.000963551			RPM =
	3	70.8	71.083	0.000974917			IN Tot Temp =
	4	66	67.022	0.000975799			IN Stat (V) =
	5	60.4	52.758	0.000858638			OUT Stat (V) =
	6	55	54.852	0.000989937			Total Pressure =
	7	49	52.587	0.000926084			Notes:
	8	44.5	53.312	0.00096226			
P6	1	38.9	52.392	0.001002061			Average Internal Temp =
	2	33.5	51.794	0.000946056			RPM =
	3	28.2	53.106	0.000930215			IN Tot Temp =
	4	22.7	64.025	0.00094182			IN Stat (V) =
	5	17.3	59.165	0.000936364			OUT Stat (V) =
	6	12	66.205	0.001617703			Total Pressure =
	7	6.7	52.632	0.001647287			Notes:
	8	3.7	52.542	0.001438849			

Table C-2: Experimental template used to calculate blade surface temperature

		Sensor	Initial Resistance	Gradient	Y-intercept	Temperature (C)	Surf Temp[K]	Resistance at 40C
P1	1	LE 1		0.130	138.510	-1058.94	-785.79	143.74
	2	2		0.048	51.128	-1058.55	-785.40	53.06
	3	3		0.060	63.841	-1053.48	-780.33	66.27
	4	4		0.060	60.707	-998.47	-725.32	63.14
	5	5		0.044	48.450	-1091.22	-818.07	50.23
	6	6		0.050	53.321	-1060.06	-786.91	55.33
	7	7		0.047	51.430	-1085.02	-811.87	53.33
	8	8		0.045	50.079	-1093.43	-820.28	51.91
P2	1	9		0.046	50.965	-1091.33	-818.18	52.83
	2	10		0.048	51.829	-1070.85	-797.70	53.77
	3	11		0.047	53.223	-1127.61	-854.46	55.11
	4	12		0.046	50.038	-1078.41	-805.26	51.89
	5	13		0.046	49.849	-1072.02	-798.87	51.71
	6	14		0.048	51.032	-1047.89	-774.74	52.98
	7	15		0.043	47.224	-1088.11	-814.96	48.96
	8	16		0.127	127.840	-1002.67	-729.52	132.94
P3	1	17		0.047	50.369	-1055.95	-782.80	52.28
	2	18		0.047	49.918	-1057.58	-784.43	51.81
	3	19		0.047	50.236	-1055.38	-782.23	52.14
	4	20		0.047	49.434	-1049.55	-776.40	51.32
	5	21		0.047	49.665	-1054.46	-781.31	51.55
	6	22		0.048	50.145	-1029.67	-756.52	52.09
	7	23		0.068	68.233	-1003.43	-730.28	70.95
	8	24		0.115	118.550	-1030.87	-757.72	123.15
P4	1	25		0.046	50.988	-1094.16	-821.01	52.85
	2	26		0.046	50.960	-1093.56	-820.41	52.82
	3	27		0.061	62.480	-1019.25	-746.10	64.93
	4	28		0.052	56.666	-1081.41	-808.26	58.76
	5	TE 29		0.051	50.870	-993.55	-720.40	52.92
	6	30		0.049	50.219	-1024.88	-751.73	52.18
	7	31		0.061	62.480	-1019.25	-746.10	64.93
	8	32		0.055	58.902	-1053.70	-780.55	61.14
P5	1	33		0.057	58.192	-1005.04	-731.89	60.51
	2	34		0.053	53.284	-997.83	-724.68	55.42
	3	35		0.069	68.311	-985.73	-712.58	71.08
	4	36		0.065	64.406	-984.80	-711.65	67.02
	5	37		0.043	50.946	-1124.64	-851.49	52.76
	6	38		0.054	52.680	-970.17	-697.02	54.85
	7	39		0.048	50.639	-1039.82	-766.67	52.59
	8	40		0.051	51.260	-999.22	-726.07	53.31
P6	1	41		0.052	50.292	-957.94	-684.79	52.39
	2	42		0.049	49.834	-1017.02	-743.87	51.79
	3	43		0.049	51.130	-1035.02	-761.87	53.11
	4	44		0.060	61.613	-1021.77	-748.62	64.03
	5	45		0.055	56.949	-1027.96	-754.81	59.17
	6	46		0.107	61.921	-578.16	-305.01	66.21
	7	47		0.086	49.164	-698.15	273.15	52.63
	8	48		0.075	49.518	-655.00	-381.85	52.54
Avg Temp			-1025.42	-730.91				

Table C-3: Experimental template used for LABview

		Fill in Labview			From other Excel docs			Last Win	
Plug	Sensor	Filter	Front-End stop	Freq	Surf Temp	Initial Volt	alphaR x E-04	Start-Stop	h
P1	1						9.100		
	2						9.103		
	3						9.145		
	4						9.630		
	5						8.840		
	6						9.090		
	7						8.889		
	8						8.823		
P2	1						8.839		
	2						9.002		
	3						8.565		
	4						8.941		
	5						8.993		
	6						9.192		
	7						8.864		
	8						9.591		
P3	1						9.124		
	2						9.111		
	3						9.129		
	4						9.178		
	5						9.137		
	6						9.349		
	7						9.584		
	8						9.338		
P4	1						8.817		
	2						8.822		
	3						9.441		
	4						8.917		
	5						9.675		
	6						9.391		
	7						9.441		
	8						9.143		
P5	1						9.569		
	2						9.636		
	3						9.749		
	4						9.758		
	5						8.586		
	6						9.899		
	7						9.261		
	8						9.623		
P6	1						10.02		
	2						9.461		
	3						9.302		
	4						9.418		
	5						9.364		
	6						16.18		
	7						16.47		
	8						14.39		

REFERENCES

Ameri, A.A., P.M. Sockol and R.S.R. Gorla. 1992. "Navier-Stokes analysis of turbomachinery blade external heat transfer," *Journal of Propulsion and Power*, 8, 374-381.

Bellows, W.J. and R.E. Mayle. 1986. "Heat transfer downstream of a leading edge bubble," *ASME Journal*, 86-GT-59.

Birch, N.T. 1987. "Navier-Stokes predictions of transition, loss and heat transfer in a turbine cascade," *ASME Gas Turbine Conference and Exhibition*, 87-GT-22.

Blair, J.P., and Launder, , R.D., 1975. "New Techniques for Measuring Film Cooling Effectiveness." ASME *Journal of Heat Transfer*, Vol. 97, pp. 539-543

Buttsworth D.R., 1997. "A finite difference routine for the solution of transient one dimensional heat conduction problems with curvature and thermal-dependent thermal properties." , University of Oxford, OUEL Report number 2130/97.

Camci, C., and Arts, T., 1985. "Experimental Heat Transfer Investigation Around the Film-Cooled Leading Edge of a High-Pressure Gas Turbine Rotor Blade," ASME *Journal of Engineering for Gas Turbines and Power*, Vol. 107, No. 4, pp. 1016-1021.

Camci, C., and Arts, T., 1985. "Short Duration Measurements and Numerical Simulation of Heat Transfer Along the Suction Side of a Film Cooled Turbine Blade," ASME *Journal of Engineering for Gas Turbines and Power*, Vol. 107, No. 4, pp. 991-997.

Camci, C., and Arts, T., 1990. "An Experimental Convective Heat Transfer Investigation around a Film-Cooled Gas Turbine Blade," ASME *Journal of Turbomachinery*, Vol. 112(3) pp 497-503.

Changmin, S., Gillespie, D., Ireland, P., and Dailey G.M., 2000. "Heat Transfer and Flow Characteristics of an Engine Representative Impingement Cooling System." ASME Paper 2000-GT-219

Cho, H.H., and Goldstein, R.J., 1995. "Heat (Mass) Transfer and Film Cooling Effectiveness with Injection Through Discrete Holes. Part 1: Within Holes and on the Back Surface." ASME *Journal of Turbomachinery*, Vol. 117, pp. 451-460

Consigny, H., and Richards, B.E., 1982. "Short Duration Measurements of Heat Transfer Rate to a Gas Turbine Blade," ASME *Journal of Engineering for Power*, Vol. 104, No. 3, pp. 542-551.

Cook, W.J. and Felderman, E.J., 1966. "Reduction of Data From Thin-Film Heat-Transfer Gauges: A Concise Numerical Technique", AIAA Journal Vol. 4, No. 3, pp 561-562.

Cook, W.J., 1970. "Determination of Heat-Transfer Rates From Transient Surface Temperature Measurements", AIAA Journal, Vol. 8, No. 7, pp 1366-1368.

Denos R., 1996. "Aerothermal investigation of the unsteady flow in the rotor of a transonic turbine stage', Ph.D. thesis, University of Poitiers

Didier F., Denos R., Arts T., 2002. "Unsteady rotor heat transfer in a transonic Turbine Stage.", ASME 2002, Amsterdam, GT-2002-30195, *Journal of Turbomachinery*, vol. 124(4), pp614-622

Diller T.E., 1993. "Advances in heat flux measurements", Academic Press, Inc, ISBN 0-12-020023-6, Advances in heat transfer, vol. 23, pp 279-368

Doorly, D.J., and Oldfield, M.L.G., 1985. "Simulation of the effects of Shock Waves Passing on a Turbine Rotor Blade." ASME *Journal of Engineering for Gas Turbines and Power*, Vol. 107, pp. 998-1006

Doorly J.E., Oldfield M.L.G., 1986. "New heat transfer gages for use on multilayered Substrates" *Journal of Turbomachinery*, vol. 108, pp 153-160

Doorly J.E., Oldfield M.L.G., 1987,."The Theory of Advanced Multi-Layer Thin Film Heat Transfer Gauges." *Journal of Heat Mass Transfer*, vol. 30 (6), pp 1159-1168

Doorly J.E., 1988. "Procedures for determining surface heat flux using thin film gages on a coated metal model in a transient test facility." *Journal of Turbomachinery*, vol. 110, pp 242-250

Dunn, M.G., Rae, W.J., and Holt, J.L., 1984. "Measurement and Analyses of Heat Flux Data in a Turbine Stage, Part 1: Description of Experimental Equipment. Part 2: Discussion of Results and Comparison with Predictions." ASME *Journal of Engineering for Gas Turbines and Power*, Vol. 106, pp. 229-240.

Dunn, M.G., 1984. "Turbine Heat Flux Measurements: Influence of Slot Injection on Vane Trailing Edge Heat Transfer and Influence of Rotor on Vane Heat Transfer." ASME Paper 84-GT-175.

Dunn, M.G., Martin, H.L., and Stanek, M.J., 1986. "heat Flux and Pressure Measurements and Comparison with Prediction for a Low Aspect Ratio Turbine Stage." ASME *Journal of Turbomachinery*, Vol. 108, pp. 108-115.

Dunn, M.G. 2001. "Convective heat transfer and aerodynamics in axial flow turbines," *ASME TURBO EXPO*, 2001-GT-0506.

Eagle Technology. 1990. "User manual for PC30 PGL and PC30 PGH", 2nd Edition, Cape Town, South Africa.

Eagle Technology website. "http://www.eagle.co.za," *Internet*.

Epstein, A.H., Kerrebrock, J.L., Koo, J.J., and Preiser, U.Z., 1985. "Rotating Effects on Impingement Cooling." GTL Report No. 184, MIT.

"Fluent Inc. Product Documentation,"
root:\Fluent.inc\documentaion\Fluent.inc\manuals\index.html.

Fransson, T.H., Rubensdorffer, F., 2004. "A New Test Facility for Evaluation of Parameters Defining Nozzle Guide Vane Endwall Heat Transfer." The 17th Symposium on Measuring Techniques in Transonic and Supersonic Cascades and Turbomachines, SE-100 44 Stockholm, Sweden

Frati, G. and R. Dénos. 2002. "One-dimensional unsteady modeling of the flow-field in a short duration facility," *ASME/IGTI*, GT-2002-30456.

GALCIT website. "http://www.galcit.caltech.edu/T5," *Internet*.

Glezer, B., Moon, H.K., Kerrebrock, J., and Guenette, G., 1998. "Heat Transfer in a Rotating Radial Channel with Swirling Internal Flow." ASME Paper 98-GT-214

Goldstein, R.J. and T. Yoshida. 1982. "The influence of a laminar boundary layer and laminar injection on film cooling performance," *Journal of Heat Transfer*, 104, 355-362.

Goldstein, R.J. and Taylor, J.R., 1982. "Mass Transfer in the Neighborhood of Jets Entering a Crossflow." ASME *Journal of Heat Transfer*, Vol. 104, pp 715-721

Goldstein, R.J., and Spores, R.A., 1988. "Turbulent Transport on the Endwall in the Region Between Adjacent Turbine Blades." ASME *Journal of Heat Transfer*, Vol. 110, pp 862-869

Goldstein, R.J. and H.H. Cho. 1995. "A review of mass transfer measurements using naphthalene sublimation," *Experimental Thermal and Fluid Science*, 10 (4), 416-434.

Graziani, R.A., M.F. Blair, J.R. Taylor and R.E. Mayle. 1980. "An experimental study of endwall and airfoil surface heat transfer in a large scale turbine blade cascade," *Journal of Engineering and Power*, 102, 257-167.

Gritsch, M., Schultz, A., and Wittig, S., 1998. "Adiabatic Wall Effectiveness Measurements of Film Cooling Holes with Expanded Exits." ASME *Journal of Turbomachinery*, Vol. 120, pp. 549-556.

Guenette, G.R., Epstein, A.H., Giles, M.B., Hanes, R., and Norton, R.J.G., 1989. "Fully Scaled Transonic Turbine Rotor Heat Transfer Measurements." ASME *Journal of Turbomachinery*, Vol. 111, pp.1-7.

Han, J.C., 1988. "Heat Transfer and Friction Characteristics in Rectangular Channels with Rib Turbulators." ASME *Journal of Heat Transfer*, Vol. 110, pp. 321-328.

Harasgama, S.P. and E.T. Wedlake. 1990. "Heat transfer and aerodynamics of a high rim speed turbine nozzle guide vane tested in the RAE isentropic light piston cascade (ILPC)," *ASME Gas Turbine and Aeroengine Congress and Exposition*, 90-GT-41.

Haring, M., Bolcs, A., Harasgama, S.P., and Richter, J., 1995. "Heat Transfer Measurements on Turbine Airfoils Using Naphthalene Sublimation Technique." ASME *Journal of Turbomachinery*, Vol. 117, pp.423-437

Hornung, H.G. 1992. "Performance data of the new free-piston shock tunnel at GALCIT," *AIAA*, 92, 3943

Incropera, F.P. and D.P. DeWitt. 1996. "Fundementals of heat and mass transfer," John Wiley and Sons Inc, 4th Edition.

Kader, B. 1993. "Temperature and Concentration Profiles in Fully Turbulent Boundary Layers," *Int. J. Heat Mass Transfer*, 24(9), 1541-1544.

Kennon, S.R. and G.S. Dulikravich. 1985. "The inverse design of internally cooled turbine blades," *ASME Journal of Eng. for Gas Turbines and Power*, 107, 123-126.

Kost, F. and M. Nicklas. 2001. "Film-cooled turbine endwall in a transonic flow field: Part I – Aerodynamic Measurements," *ASME TURBO EXPO*, 2001-GT-0145.

Kohli, A., and Bogard, D.G., 1998. "Fluctuating Thermal Field in the Near Hole Region for Film Cooling Flows." ASME *Journal of Turbomachinery*, Vol. 120, pp. 86-91.

Launder, B.E. and D.B. Spalding. 1974. "The numerical computation of turbulent flows," *Computer Methods in Applied Mechanics and Engineering*, 3, 269-289.

Ligrani, P.M., C. Camci and M.S. Grady. 1982. "Thin film heat transfer gage construction and measurement details," *Technical Memorandum 33*, von Karman Institute for Flud Dynamics

McDonald G. 1994. "Measurement of tip clearance pressure distributions and heat transfer on a turbine blade at realistic blade velocities", *Masters thesis*, School of Mechanical Engineering, University of Natal, Durban, South Africa

Mehendale, A.B., and Han, J.C., 1992. "Influence of High Mainstream Turbulence on Leading Edge Film Cooling Heat Transfer." ASME *Journal of Turbomachinery*, Vol. 114, pp. 707-715.

Mick, W.J., and Mayle, R.E., 1988. "Stagnation Film Cooling and Heat Transfer, Including its Effect Within the Hole Pattern." ASME *Journal of Turbomachinery*, Vol. 110, pp.66-72.

Noel, B.W., Borella, H.M., Lewis, W., Turley, W.D., Beshears, D.L., Capps, G.J., Cates, M.R., Muhs, J.D., and Tobin, K.W., 1990. "Evaluating Thermographic Phosphors in an Operating Turbine Engine." ASME Paper 90-GT-266

Oldfield, M.L.G., D.L. Schultz and T.V. Jones. 1978. "On-line computer for transient turbine cascade instrumentation," *IEEE Tranactions on Aerospace and Electronic Systems*, AES-14 (5), 738-749.

Oldfield M.L.G., H.J. Burd and N.G. Doe. 1982. "Design of wide-bandwidth analogue circuits for heat transfer instrumentation in transient tunnels," Department of Engineering Science, University of Oxford.

Ou, S., Han, J.C., Mehendale, A.B., and Lee, C.P., 1994. "Unsteady Wake over a Linear Turbine Blade Cascade with Air and CO_2 Film Ejection. Part 1: Effect on Heat Transfer Coefficients." Vol. 116, pp. 721-729.

Pietrzyk, J.R., Bogard, D.G., and Crawford, M.E., 1990. "Effects of Density Ratio on the Hydrodynamics of Film Cooling."ASME Journal *of Turbomachinery*, Vol. 112, pp. 437-443.

Pope A., Goin K.L., 1965, "High-speed wind tunnel testing," John Wiley & Sons, Inc., Library of Congress Catalog Card Number: 65-21435, United States of America

Rodi, W. and G. Scheuerer. 1985. "Calculation of heat transfer to convection-cooled gas turbine blades," *ASME Journal of Eng. for Gas Turbines and Power*, 107, 620-627.

Rolls-Royce, 1986. "The jet engine, "The technical publications department of Rolls-Royce pcl, ISBN 0902121235, Derby, England.

Schultz, D.L. and T.V. Jones. 1973. "Heat transfer measurements in short duration hypersonic facilities," *AGARD*, AG-165

Schultz, D.L., Jones, T.V., Oldfield, M.L.G., and Daniels, L.C. 1977. "A New Transient Facility for the Measurement of Heat Transfer Rates," *AGARD*, CP 229, Paper 31.

Snedden, G.C. 1995. "Transient measurement of heat transfer in steady state turbine cascades", *Masters thesis*, School of Mechanical Engineering, University of Natal, Durban, South Africa

Snedden G.C. 1998. "SMR-95 Cascade Aerodynamic Characterisation and Heat Transfer Measurement," *IZMAR 6*, CSIR, AEROTEK, Pretoria, South Africa.

Son, S., Kihm, K.D., Han, J.C., and Shon, D.K., 1999. "Flow Field Measurements in a Two-Pass Channel using Particle Image Velocimetry." ASME Journal of Heat Transfer, Vol. 121, No. 3, p. 509 (picture gallery)

Stieger, R. 1998. "Experimental evaluation of heat transfer distribution on a turbine blade", *Masters thesis*, School of Mechanical Engineering, University of Natal, Durban, South Africa.

Thole, K., Gritsch, M., Schulz, A., and Wittig, S., 1998. "Flow Field Measurements for Film Cooling Holes with Expanded Exits." *Journal of Turbomachinery*, Vol. 120, pp. 327-336.

Van der Steege, A.W. 1990. "Experimental investigations of special turbine blade cooling configurations", *Masters Thesis*, School of Mechanical Engineering, University of Natal, Durban, South Africa

de Villiers, J.E. 2002. "Experimental and numerical validation of the flow and heat transfer on a transonic turbine blade", *Masters Thesis*, School of Mechanical Engineering, University of Natal, Durban, South Africa

VKI website. "http://www.vki.ac.be

Wang, J.H., H.F. Jen and E.O. Hartel. 1985. "Airfoil heat transfer calculation using a low reynolds number version of a two-equation turbulence model," *ASME Journal of Eng. for Gas Turbines and Power*, 107, 60-67.

Wolfstein, M. 1969. "The velocity and temperature distribution of one-dimensional flow with turbulence augmentation and pressure gradient," *Int. J.. Heat Mass Transfer*, 12, 301-318.